ELECTROSTATIC EFFECTS IN III-V SEMICONDUCTOR BASED METAL-OPTICAL NANOSTRUCTURES

Karol Grzegorz Gryczynski, B.A., B.S., M.S.

Dissertation Prepared for the Degree of

DOCTOR OF PHILOSOPHY

UNIVERSITY OF NORTH TEXAS

May 2012

APPROVED:

Arup Neogi, Major Professor
Arkadii Krokhin, Committee Member
Usha Phillipose, Committee Member
Duncan Weathers, Committee Member
David Schultz, Chair of the Department of Physics
James D. Meernik, Acting Dean of the Toulouse Graduate School

Gryczynski, Karol Grzegorz, Electrostatic effects in III-V semiconductor based metal-optical nanostructures. Doctor of Philosophy (Physics), May 2012, 122 pp., 95 figures, references, 104 titles.

The modification of the band edge or emission energy of semiconductor quantum well light emitters due to image charge induced phenomenon is an emerging field of study. This effect observed in quantum well light emitters is critical for all metal-optics based light emitters including plasmonics, or nanometallic electrode based light emitters.

This dissertation presents, for the first time, a systematic study of the image charge effect on semiconductor–metal systems. The necessity of introducing the image charge interactions is demonstrated by experiments and mathematical methods for semiconductor-metal image charge interactions are introduced and developed.

ACKNOWLEDGEMENTS

I would like to acknowledge the hard work of my advisor Dr. Arup Neogi and my committee members Dr. Arkady Krokhin, Dr. Usha Phillipose, Dr. Duncan Weathers.

I am very grateful to my group members Akhilesh Singh for his mentoring in experimental techniques and Tony Llopis for helpful discussion.

I would also like to thank my cat for his undiminishing interest in this work.

TABLE OF CONTENTS

Page

LIST OF TABLES

Page

LIST OF ILLUSTRATIONS

Page

LIST OF ACRONYMS

I think dealing with acronym soup is one of the most prohibitive barriers for entering the field, but it shouldn't be.

The author of this dissertation first introduced "ICF." For all others, only acronyms published in peer reviewed journals are listed here.

2DEG	Two dimensional electron gas
2DG	Two dimensional gas
2DHG	Two dimensional hole gas
AFM	Atomic force microscopy
Ag	Silver
Al_2O_3	Sapphire
AlAs	Aluminum arsenide
AlGaAs	Aluminum gallium arsenide
AlGaN	Aluminum gallium nitride
Au	Gold
CL	Cathode luminescence
CW	Continuous wave
eV	Electron volt ($1.602176565*10^{-19}$ J)
FLIM	Fluorescence lifetime imaging microscopy
FWHM	Full width at half maximum
Ga	Gallium
GaAs	Gallium arsenide
GaN	Gallium nitride
HeCd	Helium cadmium
HeNe	Helium neon
HRTEM	High resolution transmission electron microscopy
ICF	Image charge field (F_{ICF})
InGaN	Indium gallium nitride
InN	Indium nitride
IQE	Internal quantum efficiency
IRF	Instrument response function

LA	Longitudinal acoustic
LO	Longitudinal optical
MBE	Molecular beam epitaxy
MOCVD	Metal-organic chemical vapor deposition
MOVPE	Metal-organic vapor phase epitaxy
MQW	Multiple quantum wells
Nm	Nanometer (10^{-9} m)
PEF	Piezoelectric field (F_{PEF})
PL	Photoluminescence
QCSE	Quantum confined Stark effect
QD	Quantum dot
QW	Quantum well
RT	Room temperature
SEM	Scanning electron microscopy
SERS	Surface enhanced Raman spectroscopy
SP	Surface plasmon
SPP	Surface plasmon polariton
SPR	Surface plasmon resonance
SQW	Single quantum well
TA	Transverse acoustic
TEM	Transmission electron microscopy
Ti:sapph	Titanium sapphire
TO	Transverse optical
TRPL	Time resolved photoluminescence

CHAPTER 1

INTRODUCTION

In this work experimental data showing the effects of image charges in semiconductor light emitting devices is presented and analyzed. A theory on the effects of image charges on semiconductor emitters is applied to explain the experimental data and numerical results are given for analyzed systems. Trends are simulated for systems not analyzed in the lab; however the theoretical systems are kept realistic to the largest extent possible.

This introduction is meant as a brief review of the most important introductory physics extensively used in this work. It is assumed that the reader has a basic understanding of graduate level physics, especially quantum mechanics and electrostatics and electrodynamics. The quantum confined Stark effect merits its own section as much of the mathematics of image charge electric fields is modeled similarly to the Stark effect.

This work is focused on experimental tests of the theory of image charges on semiconductor systems; experimental data from multiple semiconductor systems are presented and explained.

1.1 Quantum Confinement

Optical emission from semiconductors occurs when a bound electron and hole pair, called an exciton, recombines and the electron passes through the forbidden energy bandgap. The exciton has a characteristic separation distance between the electron and hole, called the exciton bohr radius, or simply the exciton radius. In a bulk structure the exciton may have this separation in any orientation; however when the dimensions of the semiconductor are smaller

than the exciton radius, the exciton is confined. Furthermore the semiconductor may have one to three dimensions smaller than the exciton. In a material which has no dimensions smaller than the exciton radius quantum confinement cannot occur. The allowed emission energies in confined structures must be discrete to satisfy the steady state Schrödinger equation of quantum mechanics ($H|\psi\rangle = E|\psi\rangle$) [1-4]. Thus the density of states in unconfined (bulk) systems is non-discrete, or quantized. The density of states in a bulk structure and quantum confined structures are depicted in figure 1.1.1.

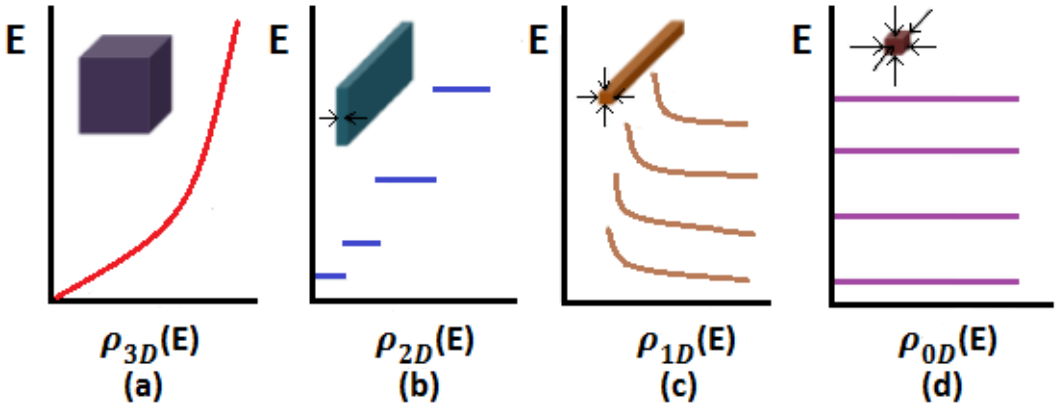

Figure 1.1.1 Illustrations of densities of states for a) bulk, b) confined in one dimension, c) confined in two dimensions, and d) confined in 3 dimensions semiconductor systems. Modified from Garner, Brett PhD Dissertation, UNT 2008 [7].

Fig. 1.1.1a shows a bulk structure with no quantum confinement and a continuous density of states. The density of states, ρ, is given by

$$\rho_{3D}(E) = \frac{1}{2\pi^2}\left(\frac{2\mu}{\hbar^2}\right)^{3/2}\left(E - E_g\right)^{1/2} \qquad 1.1.1$$

where ρ_{id} is the density of states in i dimensions, $\hbar$ is Plank's constant divided by two pi, μ is the reduced mass, E_g is the bandgap energy, and E is the energy. The bulk structure is said to be 3 dimensional (3D) since the exciton is free to move in any direction and is not shortened in any direction.

In Fig. 1.1.1b only one dimension is smaller than the exciton radius; such a quantum confined structure is a quantum well (QW). This structure is 2D since the excitons are free to move in the plane of the well, while the third dimension is too small for the exciton to move in or orient itself normal to the confined surface. As seen in figure 1.1.1b the allowed energies for a carrier in a QW are discrete, corresponding to allowed boundary condition between the well and its barriers. The density of states for a 2D structure is.

$$\rho_{2D}(E) = \frac{\mu}{\pi\hbar}\sum_{n}\theta\left(E - E_n - E_g\right) \qquad 1.1.2$$

where E_n is the energy of the n^{th} quantized energy state.

A semiconductor structure where two dimensions are confined is referred to as a quantum wire and is pictured in figure 1.1.1c. Sadly, the words 'well' and 'wire' both start with 'W' and there is no one universally agreed upon abbreviation for quantum wire. The carriers are free to move only in the direction parallel to the length of the wire. The density of states is given by,

$$\rho_{1D}(E) = \frac{(2\mu)^{1/2}}{\pi\hbar}\sum_{n}\frac{1}{\left(E - E_m - E_n - E_g\right)^{1/2}} \qquad 1.1.3$$

and finally a semiconductor structure may be made smaller than the exciton radius in all dimensions. In such a structure the carriers have no free motion; this is shown in Fig. 1.1.1d. A 0D structure is commonly referred to as a quantum dot (QD). The density of states for structures confined in three dimensions is

$$\rho_{0D}(E) = 2\sum_{n,m,l}\delta\left(E - E_l - E_m - E_n - E_g\right) \qquad 1.1.4$$

It is helpful to note that a n dimensional structure is confined in 3-n dimensions, i.e., a three dimensional bulk structure is confined in 3 – 3 = 0 dimensions and a 2D quantum well is confined in 3 – 2 = 1 dimensions and so on.

The quantum well is the most common quantum confined structure and the most important for this work. Figure 1.1.2 top shows an arbitrary QW potential. In such a well a carrier is assumed to travel in only the z direction since there is radial symmetry in the other two 'bulk' dimensions. In the simplest case, only a single quantum well (SQW) is considered. In this structure there are 3 different regions: the well region surrounded by the barriers. The well region in figure 1.1.2 is Region 2. The potential, V, in the QW system is given as

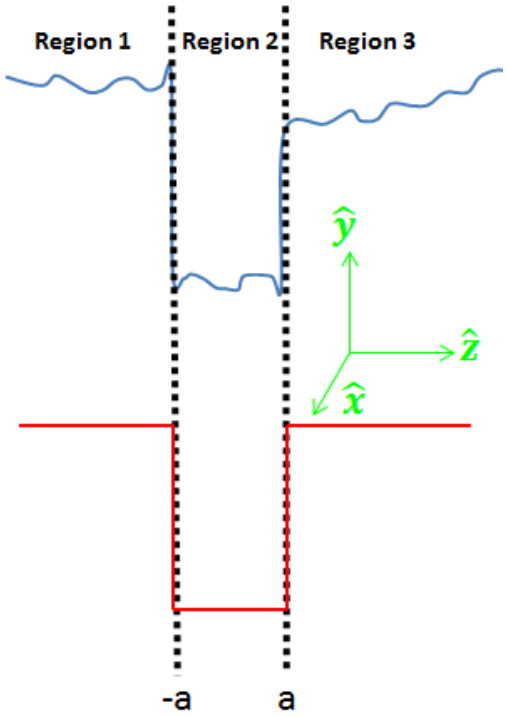

Figure 1.1.2 arbitrary well potential (top) and square well potential (bottom)

$$V = \begin{cases} g(z) & z < -a \\ f(z) & -a \leq z \leq a \\ h(z) & z > a \end{cases} \qquad 1.1.5$$

where g(z), f(z), and h(z) are arbitrary functions of z and the well is centered at 0 with width 2a. For the systems in Fig. 1.1.2 to have pure confined states the conditions $f(z) + E_0 < g(z)$ and $f(z) + E_0 < h(z)$ must hold for all z. E_0 is the lowest possible energy which the confined carrier may be in the well; as shown in Fig. 1.1.1b, E_0 is not zero. As a rule each consecutive energy state (n) must have a higher energy (E_n) than the previous energy state. Thus a QW only allows a state iff $f(z) + E_n < g(z)$ and $f(z) + E_n < h(z)$. If the particle has an energy which will not satisfy the

previous condition it is not confined. That however does not mean that it will not interact with the well, the wave function is affected by all boundary conditions. If a QW is assumed to be of infinite depth ie g(z) = h(z) = ∞ it will allow for an infinite number of confined states. Although this approximation is tolerable for some QW systems, it is not applicable to this work and merits no further discussion.

Note that V, or any of its component functions must not be continuous, nor a function in the strict mathematical sense (the delta function is an acceptable potential). If f(z) > g(z) or f(z) > h(z) the carrier in the well may tunnel out of the well even if barriers are present and greater then E_n. However if the probability of the tunneling is small, leading to the expected tunneling time to be much longer then the recombination time one may still solve for bound energy states in this well. Such states are called quasi-bound since theoretically the carriers may decay outside of the well, but in practice this is rare.

Figure 1.1.2 bottom (red) depicts a very common text book quantum well potential which gives appreciable insight. The potential for this well is given by

$$V = \begin{cases} b & z < -a \\ 0 & -a \leq z \leq a \\ b & z > a \end{cases} \quad ; \quad b > 0, b \in \boldsymbol{R}. \tag{1.1.6}$$

Thus f(z) = 0 and h(z) = g(z) = b. All the potentials are horizontal lines and the height of the barrier is b, a positive real number. The Hamiltonian for this system is,

$$H\psi = \left(\frac{-\hbar^2}{2m}\frac{d^2}{dz^2} + V(z)\right)\psi = E\psi \tag{1.1.7}$$

Solving for the wave function, ψ, we get

$$\psi = \begin{cases} b_0\, exp\left[-\dfrac{\sqrt{2m(b-E)}}{\hbar}\right] & z < -a \\ a_0\, sin\left[\dfrac{\sqrt{2n(E)}}{\hbar}\right] + a_1\, sin\left[\dfrac{\sqrt{2n(E)}}{\hbar}\right] & -a \le z \le a \\ c_0\, exp\left[\dfrac{\sqrt{2m(b-E)}}{\hbar}\right] & z > a \end{cases} \quad 1.1.8$$

Or

$$\psi = \begin{cases} \psi_1 & z < -a \\ \psi_2 & -a \le z \le a \\ \psi_3 & z > a \end{cases} \quad 1.1.9$$

where b_0, a_0, a_1, and c_0 are constants to be matched to boundary conditions; the energy, E, is also unknown. Notice that equation 1.1.8 is a solution wave function to eq. 1.1.7 and is not general. V = b for a < z < -a, the potential is a constant in the barriers. There are five unknowns and five equations; thus, solving for the energy and constants is possible. Four boundary conditions are known: $\psi_1(-a) = \psi_2(-a)$, $\psi_2(a) = \psi_3(a)$, $\psi_1'(-a) = \psi_2'(-a)$, and $\psi_2'(a) = \psi_3'(a)$, where the first two equations are the continuity condition and the second two insure that the rate of change across the boundary is equal at each side of the barrier. The fifth equation is the normalization condition: $\langle\psi|\psi\rangle = 1$.

A solution wave function may be a linear combination of solution wave functions for any number of allowed states. Thus if the set of states ψ_i is possible for a QW, another possible solution to the Schrödinger Equation is the wave function $\Psi = \sum_i A_i\psi_i$, where A_i are coefficients satisfying the normalization condition. However it is very uncommon to observe more than one state in a semiconductor SQW.

Although the above method is 'brute force' mathematics it is well suited for a computer. Chapter 2 presents iterations of about one hundred calculated energies. Appendix A provides

an overview of implementing the above mentioned calculation method using Mathematica (Wolfram Research, Champaign, Illinois). The graphical method of solving a finite square well presented in most undergraduate quantum mechanics texts is more elegant, but does not generalize to most other potentials and their corresponding wave functions.

In solving the quantum well, the fact that the three Cartesian coordinates are linearly separable was used. This is why the energy was solved only on one axis, the confinement axis. Thus it is possible to consider a "two dimensional" quantum well. The intuitive method which works is to separate the potential into two dimensions, say along z and y. Then the same procedure may be used to find allowed states in two dimensions n_z and n_y, and their corresponding energies, E_z and E_y. This is an approximation to a quantum wire which has a rectangular cross section with edges shorter than the exciton radius (Fig. 1.1.1c). In practice such a potential is not a good approximation for most quantum wires since the cross sectional shape of quantum wires often depends on the crystal lattice type of the semiconductor they are made of.

Taking the above procedure to the next level; a three dimensional quantum well may be modeled. All three dimensions in Cartesian coordinates are taken to be less than the exciton radius, thus three quantum states exist and the total confinement of energy $E = E_x + E_y + E_z$. This is a box with lengths L_x, L_y, and L_z, which must not necessarily be equal, but may also form a cube. This is of course a quantum dot and such a system is depicted in figure 1.1.1d. A more realistic model for a quantum dot is a spherical confinement potential. This problem is naturally best solved in spherical coordinates.

1.2 Image Charge Interactions

It is well known that for any neutrally charged metal there is no electric field in its interior, electric field lines emanating or ending at on its surface are normal to the surface, no field lines may cross the surface, and the charge carriers (free electrons) are located on the surface of the metal. When a charged object, point charge or macroscopic object, is brought close to a metal its electric field interacts with the free moving charges on the metal. In order to maintain the before mentioned conditions the free carrier in the neutral metal must rearrange themselves as a result of the presence of the electric field from the charged object. In order to maintain the condition that there is to be no electric field within the metal the electrons on the metal surface rearrange in such a way that charges of opposite sign to that of the foreign charged object replace other charges on the surface of the metal closest to the foreign charge. The non-uniform charge distribution on the metal thus results in the metal creating an electric field outside the metal. This external field is necessary to maintain the electric field in the metal at zero; it also exerts a force on the charged object in the vicinity of the metal [5].

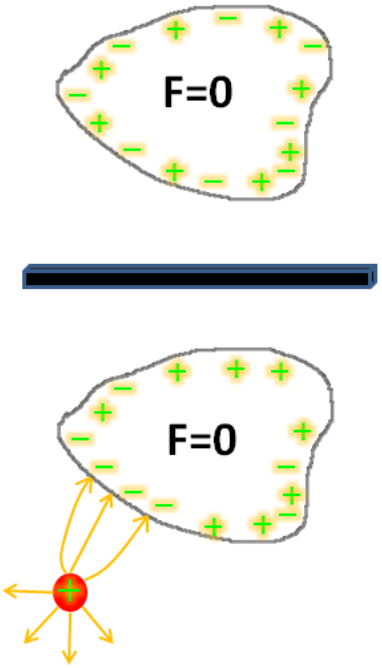

Figure 1.2.1 A neutral metal (top) and a neutral metal in the presence of a charges object (bottom).

To calculate the force on a point charge frm the neutral metal one has to know the surface charge distribution, σ, on the metal surface. However, for geometries with certain symmetries such vigorous treatment of the problem is not necessary when only solving for the

field outside the metal. In these cases the method of images may be employed to find the electrostatic force on the charged object due to the neutral metal. In these cases the method of images may be employed to find the electrostatic force on the charged object due to the neutral metal. In this technique the metal is removed from the mathematical calculations and replaced with a single charge inside the metal with charge opposite to that of the point charge. By placing the single charge in the correct position, knowing the charge distribution on the metal is not necessary. This is possible because of the uniqueness theorem which states that any arrangement of charges which satisfies all boundary values in the physical system is acceptable to use in regions where the imaginary charge distribution is not present.

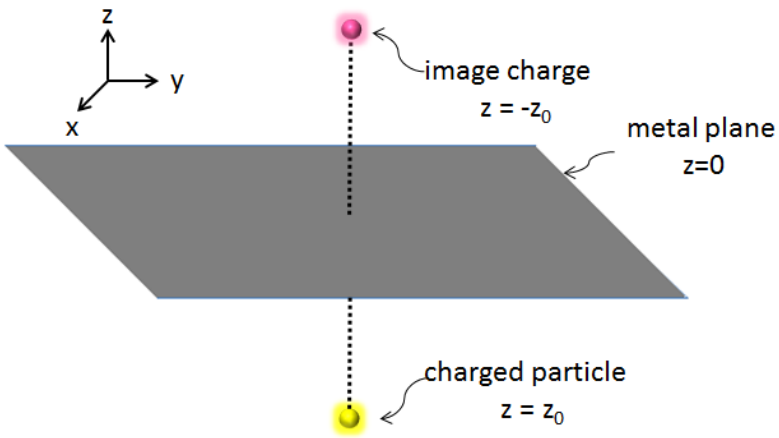

Figure 1.2.2 Image charge effect for a plane and point charge

A common and useful case is to approximate the force on a point charge from a neutral plane metal surface. This is more realistic if one considers the surface areas of a charge carrier (electron/hole) and a flat (2d) metal surface. In the mathematical approach the metal plane is completely removed and replaced with a virtual image charge of the real point charge. The position of the virtual charge would be as if the real charge was in front a flat mirror, thus the image charge effect. The real charge (yellow) and image charge (pink) must be equidistant from

the charge plane (grey) and the absolute values of their charge must be the same – equal and opposite charge. Notice that for the uniqueness theorem to be applicable the boundary conditions on the plane must be satisfied – i.e. the electric field lines must be normal to the plane. This will only be the case if the real charge and image charge are equal distances away on the plane and on a line normal to the plane. Because of the condition that the two charges be on a line normal to the plane this problem is equivalent to a two dimensional problem of two charges equidistant from a line, the image and real charge being on opposite sides of the line.

Another common image charge configuration is that for a sphere, or circle in two dimensions. Again the same logic is applied as in the case of the plane, only now there is a curved surface.

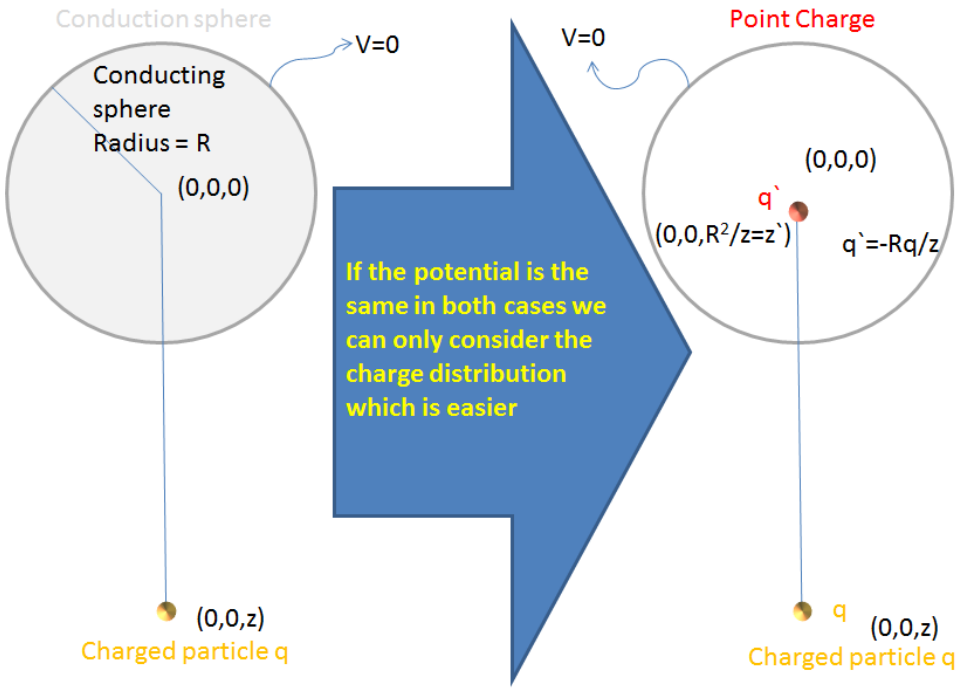

Figure 1.2.3 Image charge effect for a charged sphere

Figure 1.2.3 presents such a system where the sphere is centered at the origin and a point charge is located at a distance z from the center of the sphere. The sphere exerts a force on the point charge as discussed earlier. To model this system the boundary condition that the field lines on the spherical surface must be normal to the surface is necessary to insure the valid application of the uniqueness theorem. The left side of Fig. 1.2.3 shows the sphere and real charge, and the right side shows the real charge, image charge, and the sphere's surface. The potential and field outside the spherical surface is the same, however the field inside the spherical surface on the right does not correspond to anything physical. To insure that the field lines are correct on the spherical surface the image charge must have the opposite charge to the real charge, however its size is scaled by R/z where R is the radius of the sphere. The image charge must be closer to the image point charge then the surface of the sphere then the center, the position of the image charge is R^2/z.

The image charge field is distinct from a normal electric field in that it is attractive to both and electron and a hole (both signs of charges). Normally an electric field is attractive to one charge and repulsive to the other. Figure 1.2.4 depicts a positive and negative charge. They experience forces from the external field which are equal in magnitude and opposite in direction (red vectors), and the image

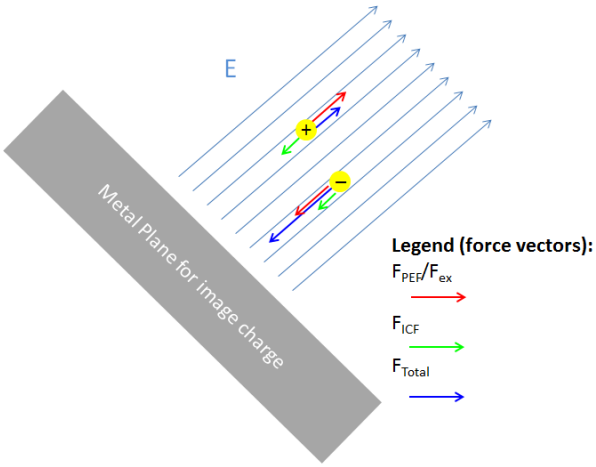

Figure 1.2.4 A positive and negative point charge in an electric field and by a metal plane inducing image charge effect. The forces on the particle are shown as vectors. Red from electric field, green from image charge, and blue the net force on each carrier.

charge forces (green vectors) which are equal in intensity and direction. Thus the net force (blue vectors) on the particles can differ in both in magnitude and direction.

Another important application of the method of images is ability to be applied to metals which carry a net charge. These systems are more complex and often require more than one image charge. However such systems are not necessary for this work.

1.3 Quantum Stark Effect

The Stark effect is the shift or splitting of spectral lines due to the presence of a static electric field. It is an electric analogue to the Zeeman Effect.

The quantum Stark effect is the Stark effect applied to semiconductor hetero junctions or quantum wells. The effect is used to study static electric fields uniformly applied to quantum wells. Since the confined particles in the semiconductor QWs are charged they feel a potential from the externally applied static electric field. This electrostatic potential is additive to the quantum confinement potential. Thus the potential of confinement V becomes V + eFz. Where e, F, and z are the carrier charge, electric field and the normal distance in the quantum confined structure. Notice that the charge of the electron and hole are opposite leading to a different additive potential for the electron and hole.

A common semiconductor quantum well is made from the heterojunctions of gallium arsenide (GaAs) and aluminum gallium arsenide (AlGaAs or GaAlAs). In these QWs, GaAs serves as the barrier and AlGaAs as the well. Such quantum wells naturally have square well potential for their carriers. The alteration to the potential due to the external electric field is linear, since e and F are constant and z is the distance in the well. This effectively changes the potential

from rectangular to triangular. Optically this leads to a red shift in the confined emission. Figure 1.3.1 shows data on the Stark effect from Bastard et al. [13]. The top plot shows extracted data of the Stark energy shift versus applied electric field. The bottom graph of Fig. 1.3.1 shows the rate of change in the emission energy shift as a function of the applied electric field. Note that for higher electric fields the rate of change is greater, i.e. the emission energy decreases faster. Thus as the well becomes more triangular the emission energy decreases more rapidly.

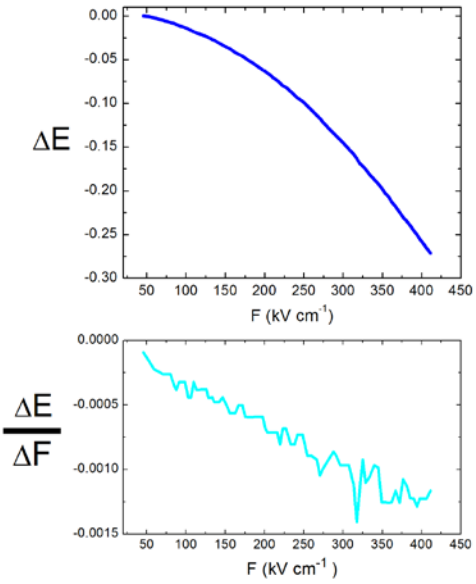

Figure 1.3.1 Energy shift from the Stark Effect in an AlGaAs QW (top) and rate of change of the energy shift (bottom)

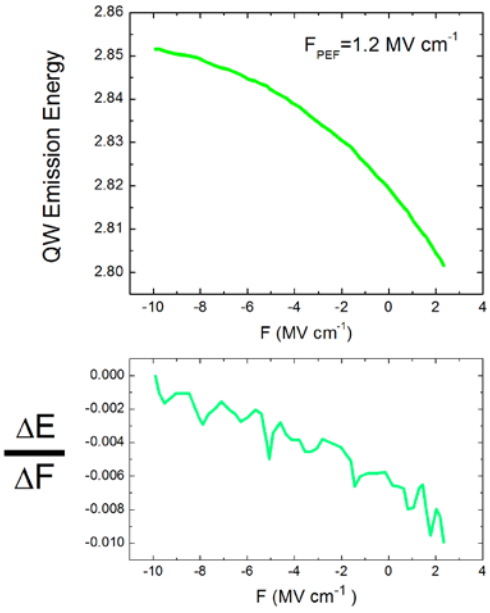

Figure 1.3.2 Stark effect energies for a InGaN QW with internal electric field of 1.2 MV cm^{-1} (top) and the rate of change in emission energy v. applied field (bottom)

Another common semiconductor quantum well is made from heterojunctions of gallium nitrite (GaN) and Indium gallium nitrate (InGaN). InGaN forms the well and GaN the barrier of the well. These wells have naturally occurring internal electrical, or piezo electric fields (PEF) which arise from natural lattice mismatches in the junction between InGaN and GaN. These wells naturally have a triangular potential like AlGaAs wells have in the presence of an external electric field. Figures 1.3.2 and 1.3.3 show the effects of the Stark effect on InGaN QWs with different

intensity internal electric fields, from Kaneko et. al [15]. The rate of shift v. the applied electric field is plotted on the bottom of the two plots. It is important to note that the externally applied electric fields in these plots is opposing the PEF. Thus as the intensity of the applied electric field (F_{ex}) is increased the total electric filed (F) decreases. $|F| = F_{PEF} - F_{ex}$. Thus as the total internal field decreases the emission energy increases.

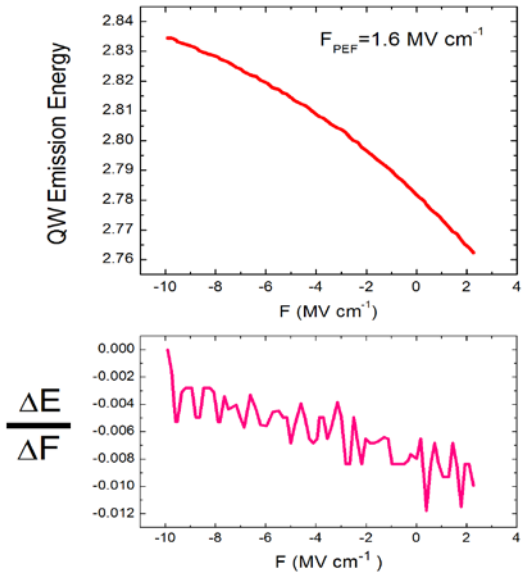

Figure 1.3.3 Stark effect energies for a InGaN QW with internal electric field of 1.6 MV cm-1 (top) and the rate of change in emission energy v. applied field (bottom)

Figure 1.3.4 shows the data from Jho et. al [16]. Which show that a varying electrostatic field may cause a blue shift or a red shift depending on the intensity of the applied external field. When the external electric field is positive there is a red shift, if there is a negative field applied there is a blue shift until $F_{ex} = -F_{PEF}$ and then there is red shift from the maximum emission energy. Also the rate of change in the emission energy is minimal where the emission energy is maximal. The dotted line in Fig. 1.3.4 bottom is the line where the rate of change is zero. Notice that as the rate of change in emission energy v. applied electric field is increasing until it becomes zero (maximum emission energy) and then decreases. Thus when $F_{ex} = -F_{PEF}$ the well is most likely a square potential.

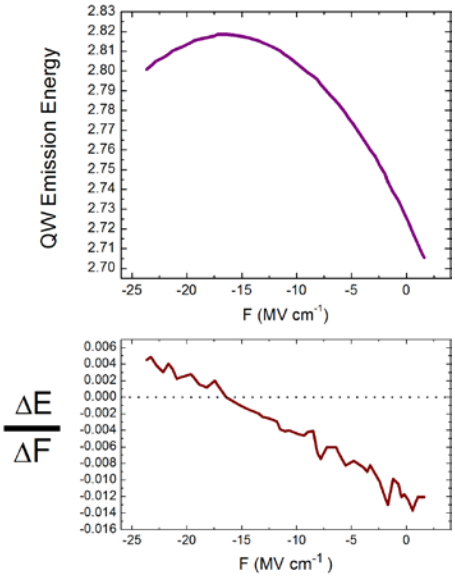

Figure 1.3.4 Stark effect energies for an InGaN well (top) and the rate of change in energy shift v. electric field

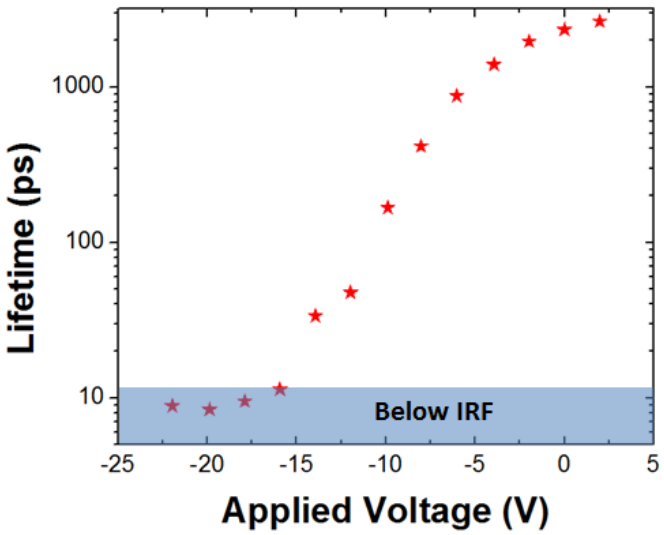

Figure 1.3.5 Lifetime per applied electric field for system in figure 1.3.4

As the confined electron/hole wave functions are spread further apart the recombination lifetime of the system is increased. The wave function separation increases with the net electric field. Figure 1.3.5 shows the change in lifetime v. external electric field for the system of figure 1.3.4. It should be noted that at the point where the lifetime is minimal (Fig. 1.3.5), the emission energy maximal (Fig. 1.3.4 top), and the rate of change in energy shift is zero (Fig. 1.3.4. bottom) the externally applied electric field cancels the internal PEF. In this case the potential energy in the QW is square like.

For both QW systems (square (AlGaAs) and triangular (InGaN)) the shift in energy becomes more intense as the well potential become more triangular, or F_{total} increases. This is illustrated for various wells in the rate of change in energy shift per applied electric field (Figs. 1.3.1 – 1.3.4). A negative value on these plots represents that the energy is decreasing and a positive number when the energy is increasing (PEF is countered by applied field). The larger the absolute value of the rate of change represents the intensity of the shift. The larger the net electric field, the more triangular the well becomes.

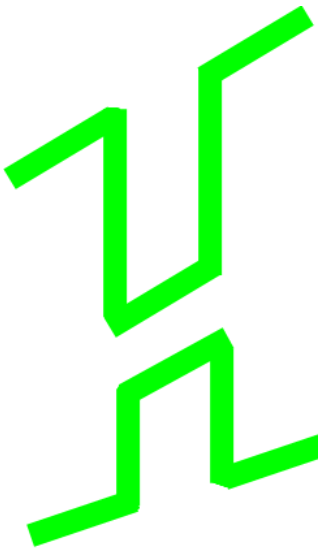

Figure 1.3.6 Triangular quantum well potential schematic

In general the potentials for QWs in an external electric field are triangular (Gig.1.3.6) wells with the Hamiltonian given below:

$$H_{well} = \frac{-\hbar^2}{2m^*}\frac{d^2}{dx^2} + (V_0 + e(F)x). \tag{1.3.1}$$

The solution wave functions to the above Hamiltonian are:

$$\Psi = \begin{cases} a_1\left(\boldsymbol{i}\,\mathrm{Ai}\left(-\left(\frac{2m^*}{(\hbar eF)^2}\right)^{1/3}(E - V_0 - eFx)\right) + \mathrm{Bi}\left(-\left(\frac{2m^*}{(\hbar eF)^2}\right)^{1/3}(E - V_0 - eFx)\right)\right) & z < -\frac{L}{2} \\ a_0\,\mathrm{Ai}\left(-\left(\frac{2m^*}{(\hbar eF)^2}\right)^{1/3}(E - eFx)\right) + b_0\mathrm{Bi}\left(-\left(\frac{2m^*}{(\hbar eF)^2}\right)^{1/3}(E - eFx)\right) & -\frac{L}{2} \le z \le \frac{L}{2} \\ a_1\ \mathrm{Ai}\left(-\left(\frac{2m^*}{(\hbar eF)^2}\right)^{1/3}(E - V_0 - eFx)\right) & z > \frac{L}{2} \end{cases} \tag{1.3.2}$$

Eigenvalues of energy for the above equations correspond to the QW energy emissions. To find a shift in energy due to the Stark effect the difference between two energy eigenvalues solved with different values of F must be found. It should be noted that there exist special cases when the potentials for real quantum wells are best approximated as square wells. This happens for AlGaAs in the case of no external electric field and for InGaN when $F_{ex} = F_{PEF}$. Thus for both cases when the net electric field across the well is zero the potential is best approximated as a finite square well.

1.4 Plasmonics

The image charge effect is not necessarily related to plasmonics. Plasmonic phenomena are discussed as another means of carrier recombination engineering which can coexist with image charge engineering. It is important to be able to compare and contrast the image charge effect and plasmonic effects in chapter 3, thus a brief review is presented for the interested reader.

A plasmon is a quantum of oscillation of an electromagnetic wave originating from the oscillation of electrons. The free electrons in a metal may be seen as a dilute ionized gas, or plasma. Plasmonics generally refers to ensembles of electromagnetic wave oscillations. Surface plasmons are electron oscillations which are localized to the interface of a dielectric material with a positive dielectric constant and that of a metal with a complex (negative real) dielectric constant. Of course these electromagnetic fields obey Maxwell's equations and may be solved as boundary condition problems.

$$E_{2x} = \frac{ic}{\omega\varepsilon_x}\kappa_2 A e^{ikx-\kappa_2(z-d)} \tag{1.4.1}$$

$$\vec{\nabla}\times\vec{E} = -\frac{1}{c}\frac{\partial\vec{H}}{\partial t} = \frac{i\omega}{c}\vec{H} \tag{1.4.2}$$

Taking the fields in the dielectric to have subscript 1 and in the metal subscript 2, the fields become:

$$H_1 = Be^{ikx+\kappa_1 z} + Ce^{ikx-\kappa_1 z} \tag{1.4.3}$$

$$E_{1x} = -\frac{ic}{\omega\varepsilon_m}\kappa_1[Be^{ikx+\kappa_1 z} - Ce^{ikx-\kappa_1 z}] \tag{1.4.4}$$

$$\kappa_1{}^2(\omega) = k^2 - \frac{\omega^2}{c^2}\varepsilon_m(\omega) \tag{1.4.5}$$

$$H_2 = Ae^{ikx-\kappa_2(z-d)} \tag{1.4.6}$$

$$E_{2x} = \frac{ic}{\omega\varepsilon_x}\kappa_2 A e^{ikx-\kappa_2(z-d)} \tag{1.4.7}$$

$$\kappa_2{}^2(\omega) = \varepsilon_x\left(\frac{k^2}{\varepsilon_z} - \frac{\omega^2}{c^2}\right) \tag{1.4.8}$$

Solving for κ_2/κ_1 the dispersion relation - which must have lower frequency than ck (light cone line), may be obtained.

$$\frac{\kappa_2}{\kappa_1} = -\left(\frac{\varepsilon_x}{\varepsilon_m}\right)\coth\left(\frac{\kappa_1 d}{2}\right) = -\left(\frac{\varepsilon_x}{\varepsilon_m}\right)\tanh\left(\frac{\kappa_1 d}{2}\right) \tag{1.4.9}$$

The energy of these plasmons is altered by the dielectric contrast of the materials at the interface and by the geometry of the surface they are on. For example the bulk plasmon energy of gold is in the ultra violet; however when gold micro spheres are imbedded in a dielectric the surface plasmon energy is decreased to the visible region. In the case of the Lycurgus Cup, the plasma energy, $\hbar\omega = hc/\lambda$, corresponds to the red part of the visible spectrum. These plasmons give the cup a red color when illuminated from the inside since the plasmons in the gold microspheres scatters blue and green light back into the cup, and thus gold makes it red.

Figure 1.4.1 Lycurgus Cup – a cup with gold nanoparticles which absorb and scatter light of certain frequencies, thus light passing through the cup and reflecting from the cup have different colors. This is a famous example of plasmonics. When a white light is placed inside the cup (right red), the light is absorbed and scattered more at plasma frequencies giving rise to enhanced reflection and reduced transmission, the cup transmits; only the longer wavelengths and absorbs the shorter ones. When illuminated from the outside the cup appears green (left green).

Figure 1.4.2 shows a schematic of a surface plasmon. The fields are consistent with equations 1.4.1 to 1.4.9. The field exists in both the metal and the dielectric and it decays exponentially in both materials since it has an imaginary wave vector. The penetration depth of the field in the dielectric is often given by the relation

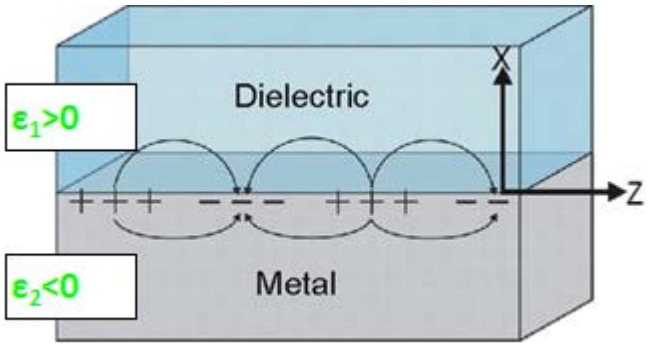

Figure 1.4.2 schematic of plasmons at a metal / dielectric interface

$$X = \frac{\lambda}{2\pi}\sqrt{\frac{\left(\varepsilon'_{die} - \varepsilon'_{metal}\right)^2}{\left(\varepsilon'_{die}\right)^2}} \tag{1.4.10}$$

where X is the penetration depth, λ the wavelength, and ε the dielectric constant. The distance X is defined as the distance at which the field strength drops to 1/e of its initial intensity. Thus there is a distance dependence of how far a plasmonic interaction may be felt in the dielectric. The plasmon field strength decays exponentially in the dielectric and metal.

The frequency of a plasmon is determined by the properties of the metal it exists on and the dielectrics the metal is joined to. Table 1.4.1 lists the bulk plasma frequency of various metals.

Table 1.4.1 Bulk plasmon energies, from reference Somorjai and Lin [6]

Martial	Bulk plasmon energy (eV = hc/λ)
Aluminum	14.75
Gold	9.02
Copper	7.38
Lead	7.36
Tungsten	6.40
Vanadium	5.15
Nickel	4.88
Iron	4.09
Cobalt	3.96
Titanium	2.51

Thus when selecting a metal for plasmonics, both the distance from the optically active layer and bulk plasmon energy must be considered.

In an optically active system, such as the quantum wells discussed in this work, there is a thin metal film sandwiched between two dielectrics, the semiconductor the air/vacuum on the other side of the metal film. Economou [21] modeled such a system and an example dispersion curve shown in Fig. 1.4.3. The analytical expressions for the two curves are:

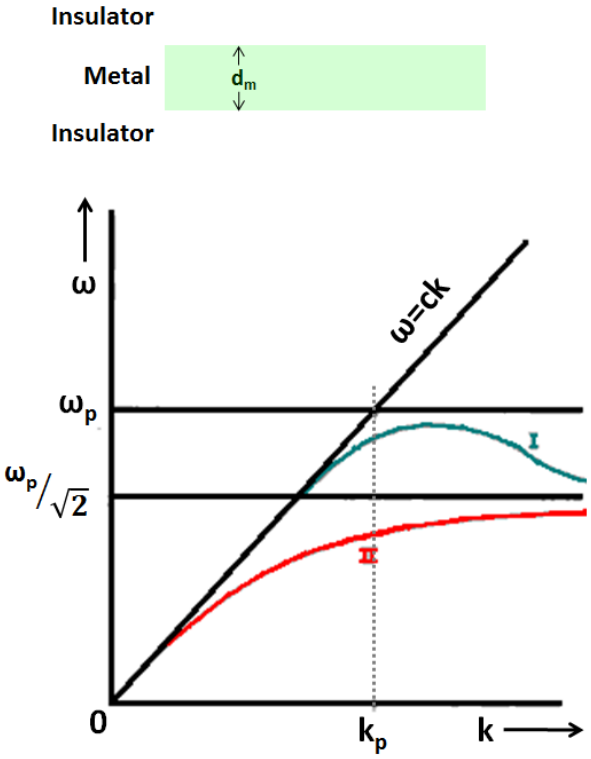

Figure 1.4.3 Geometry and the dispersion relations for SP of a metal film between to semi-infinite dielectric. Expression for k<<kp [21].

$$\omega = \left(\frac{\omega_p}{\sqrt{2}}\right)\sqrt{1 \pm e^{-kd_i}} \tag{1.4.11}$$

for curve II in figure 1.4.3 and

$$k \cong \frac{\omega^2}{c^2} + \frac{\omega^4}{c^2\omega_p^2}\tanh^2\left({}^1\!/_2\, k_p d_m\right) \tag{1.4.12}$$

For curve I of figure 1.4.3. Of course eqs. 1.4.11 and 1.4.12 are only valid for the ideal metal dielectric interface [20]. For the metal,

$$\varepsilon_m(\omega) = 1 - \frac{\omega_p^2}{\omega^2} \tag{1.4.13}$$

and it is assumed that the dielectric constant is not highly absorptive at frequencies over ω_p. Thus eqs. 1.4.11 and 1.4.12 are only valid when ω_p is less than the absorption edge.

A more complete treatment of surface plasmon dispersion is given by Gonjoti et. al [22]. The dispersion relation for a metal film between two dielectrics with dielectric constants ε_1 and ε_3, with the metal having a dielectric constant ε_2 (figure 1.4.4) is:

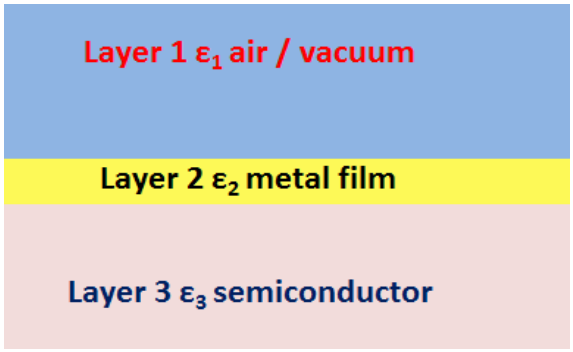

Figure 1.4.4 schematic of metal sandwiched between two different dielectrics

$$0=(\varepsilon_1\gamma_2+\varepsilon_2\gamma_1)(\varepsilon_2\gamma_3+\varepsilon_3\gamma_2)-(\varepsilon_3\gamma_2-\varepsilon_2\gamma_3)(\varepsilon_1\gamma_2-\varepsilon_2\gamma_1)e^{-2\gamma_2 t} \quad (1.4.14)$$

where

$$\gamma_i^2=k^2-\varepsilon_i\omega^2/c^2 \quad (1.4.15)$$

and k is the wavenumber, ω is the oscillation frequency, ε_i is the dielectric function of the material, and c is the speed of light in vacuum. The rate at which quantum well spontaneous emission recombines with the plasmon continuum is given by

$$\Gamma_p(\omega)=\frac{2\pi}{\hbar}\langle \boldsymbol{d}\cdot\boldsymbol{E}(a)\rangle^2\rho(\hbar\omega) \quad (1.4.16)$$

This leads to a decrease in lifetime, increase in the density of states, and an increase in luminescence intensity. Excitons and surface plasmons couple when the exciton recombination energy and surface plasmon energy are very close together. Surface plasmons of course can couple to excitons in quantum wells.

1.5 Chapter References

1. John Townsend, A Modern Approach to Quantum Mechanics, University Science Books (2000)
2. David J. Griffiths, Introduction to Quantum Mechanics, Pearson Education (1993)

3. R. Shankar, Principles of Quantum Mechanics, Springer Science (1994)

4. L. D. and L. M. Lifshitz, Quantum Mechanics Non-Relativistic Theory, Third Edition: Volume 3, Butterworth-Heinemann (1977)

5. F.T. Vasko, A.V . Kuznestow. Electronic States and Optical Transitions in Semiconductor Heterostructures, Springer-Verlag New York Inc. (1999)

6. Gabor A. Somorjai, Yimin Li, Introduction to Surface Chemistry and Catalysis, John Wiley & Sons, Inc. (2010)

7. Brett William Garner, Multifunctional Organic-Inorganic Hybrid Nanophotonic Devices, University of North Texas (2008)

8. David J. Griffiths, Introduction to Electrodynamics (3rd Edition), Prentice-Hall (1999)

9. John David Jackson, Classical Electrodynamics Third Edition, Hamilton Printing Company (1999)

10. D. Halliday, R. Resnick, and K. S. Krane, Physics, Volume 2, 3th Edition, Wiley (1996)

11. E. M. Purcell, Electricity and Magnetism, 2nd Edition, McGraw Hill (1997)

12. Mark A. Heald and Jerry B. Marion, Classical Electromagnetic Radiation Third Edition, Saunders College Publishing (1995)

13. G. Bastard, E. E. Mendez, L. L. Chang, and L. Esaki, Phys. Rev. B 28, 6 (1983)

14. D. A. B. Miller, D. S. Chemla, and T. C. Damen ,A. C. Gossard and W. Wiegmann, T. H. Wood and C. A. Burrus, Phys. Rev Lett., 53, 22, (1984)

15. T. Takeuchi, C. Wetzel, S. Yamaguchi, H. Sakai, H. Amano, I. Akasaki, Y. Kaneko, S. Nakagawa, Y.Yamaoka, and N. Yamada, Appl. Phys. Lett 73, 1691 (1998)

16. Y. D. Jho, J. S. Yahng, E. Oh, and D. S. Kim, Appl. Phys. Lett 79, 8, (2001)

17. P. C. Wu, T.-H. Kim, A. S. Brown, M. Losurdo, G. Bruno, and H. O. Everitt, Appl. Phys. Lett. 90, 103119 (2007)

18. D. Ahn and S.L. Chuang, Phys. Rev. B, 34, 12 (1986)

19. S.F. Chichibu, A.C. Abare, M.P. Mack, M.S. Minsky, T. Deguchi, D. Cohen, P. Kozodoy, S.B. Fleischer, S. Keller, J.S. Speck, J.E. Bowers, E. Hu, U.K. Mishra, L.A. Coldren, S.P. DenBaars, K. Wada, T. Sota, and S. Nakamura, Mat. Sci. and Eng., B59 298 (1999)

20. Nagaraj and A. A. Krokhin, Phys. Rev. B, 81, 8, 085426 (2010)

21. E. N. Economou, Phys. Rev., 182, 2, (1969)

22. I. Gontijo, M. Boroditsky, E. Yablonovitch, S. Keller, U. K. Mishra and S. P. DenBaars, Phys. Rev. B, 60, 16 (1999)

CHAPTER 2

ON THE IMAGE CHARGE EFFECT IN SEMICONDUCTOR QUANTUM WELLS

This chapter makes the connection from the introduction to quantum wells to describing real semiconductor systems. The finite square well systems works well for aluminum gallium arsenide wells, but is very poor for indium gallium nitride wells which have an internal electric field. This chapter solves and explains the potential of QWs with internal electric fields, originating from inherit internal properties, externally applied fields, and image charge fields.

A semiconductor QW is made of at least two hetero-junctions, or joinings of different semiconductors. In these hetero-junctions of thin films there is only one film with one confinement direction. This dimension is smaller than the Bohr exciton radius and is typically on the order of a few nanometers; the other dimensions are much larger. Figure 2.1 presents a schematic. Each color is a different semiconductor, and the thin red slab is the quantum well with a confinement potential in the vertical direction.

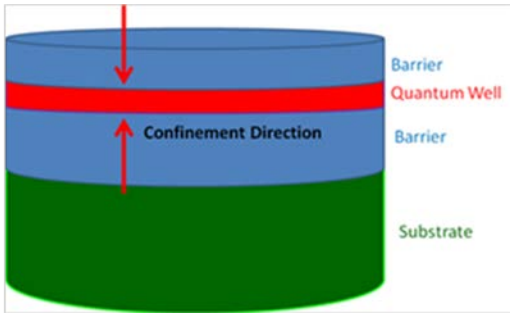

Figure 2.1 Schematic of a semiconductor quantum well

A photograph of an AlGaAs QW sample is shown in figure 2.2. The left side is coated with a dried silver colloid solution.

Figure 2.2 Photograph of AlGaAs SQW wafer

Another important aspect of quantum wells discussed in this chapter is the motion of carriers in the plane direction of the well. This leads to effects such as temperature dependent shifts and determines when carriers experience different potentials.

2.1 Alteration to Confinement Potentials

In semiconductor systems there are two confinement potentials: one for the electrons and one for the holes. The emission energy from a semiconductor quantum well is the sum of the bulk exciton energy in the well plus the confinement potentials of the electron and hole. The two potentials of the wells are often represented with the electron potential on top and an upside down well for the hole below it. In common schematics the electron and hole wells may be thought of as mirror images, if the two potentials are the same. The total depth of both wells is the difference in exciton emission energies between the barrier material and the well material. The potentials of the electron and hole wells are rarely the same; most often the electron well is deeper. This is why semiconductor quantum wells are often described as X%/(100-X)% wells. The first number is the percent of the total depth which is the electron well depth followed by a slash ("/") and then the percentage of the total potential difference which is used for the hole depth. Obviously the two percentages sum to 100%. Common semiconductor well potentials are 70/30 and 60/40.

The quantum confinement potential of an aluminum gallium arsenide ($Al_{0.33}Ga_{0.66}As$) well is an introductory style finite square well potential. This happens because the system has no internal electric fields and $Al_{0.33}Ga_{0.66}As$ and GaAs are lattice matched leading to no strain. Furthermore AlGaAs wells are easily reproducible on different instruments and have very well-known potentials. An example AlGaAs potential is depicted in figure 2.2.1 left.

The image charge potential introduces a potential in the quantum well. The image charge interaction may arise between a carrier in the well and a metal in close proximity to that carrier. Thus the AlGaAs well under the influence of the image charge effect is the sum of the

confinement potential and the image charge potential. The image charge potential is attractive to both the electron and the hole, thus both of their potentials are affected identically. Such a potential is depicted in the right side of Fig. 2.2.1. It should be noted that since both the potentials are affected in the same way, the deeper corners of the potential are on the same side, and apart from the different barrier heights the two potentials are mirror images of each other. This is in contrast to the quantum Stark Effect where one carrier is attracted and the other repelled leading to the deep corners of the potential to be on opposite sides of the wells. The well depth is not altered, but the electric potential is felt along with the confinement potential. The potential changes from $V_0 \rightarrow V_0 + eFz$ for both the electron and hole potentials. This means that the solution wave functions changes from the trigonometric functions into Airy functions.

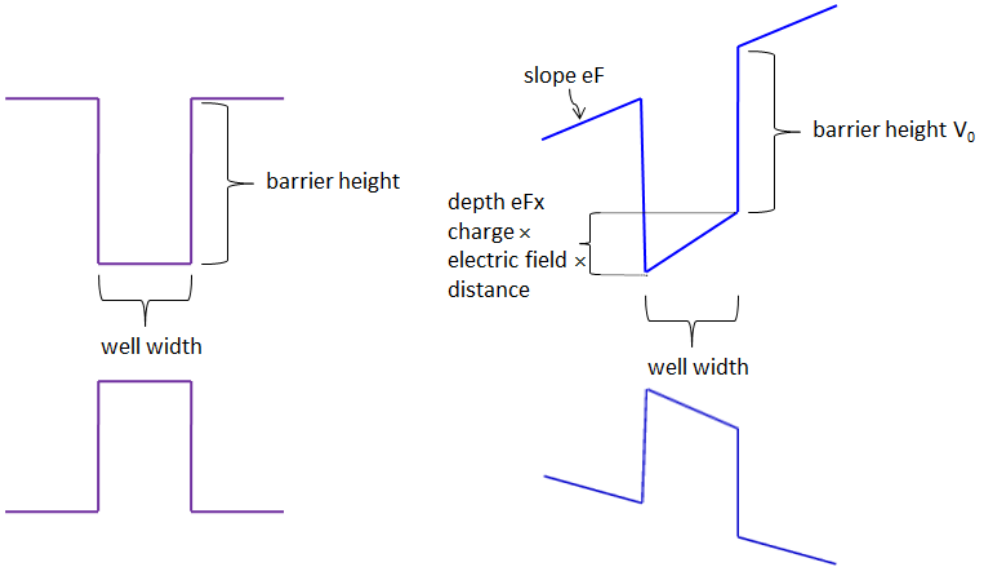

Figure 2.2.1 Potential of AlGaAs quantum well with no external influence (left) and an AlGaAs quantum well in the presence of an image charge field (right).

Indium gallium nitride (InGaN) is more difficult to model then AlGaAs. This is mostly due to the bandgap of InGaN not being reliably reproducible. The well depth differs for InGaN made

under the same conditions in different instruments. Furthermore for InGaN grown in the same instrument only varying temperature the well emission may differ by as much as 200 nm. InGaN also has a naturally occurring internal electric field. This field originates from internal mechanical strain and is often referred to as the piezoelectric field (PEF). The field from this force is abbreviated as F_{PEF}. This internal field is estimated to range from less than 1 MeV cm^{-1} to over 2MeV cm^{-1}. Again there is no reliable method to grow InGaN predictably with a pre-determined PEF unless the same exact instrument is used. However the PEF results in a quantum well potential results in the same type of potential as the Stark Effect. The field is constant across the InGaN well. Figure 2.2.2 depicts a typical schematic for an InGaN quantum well.

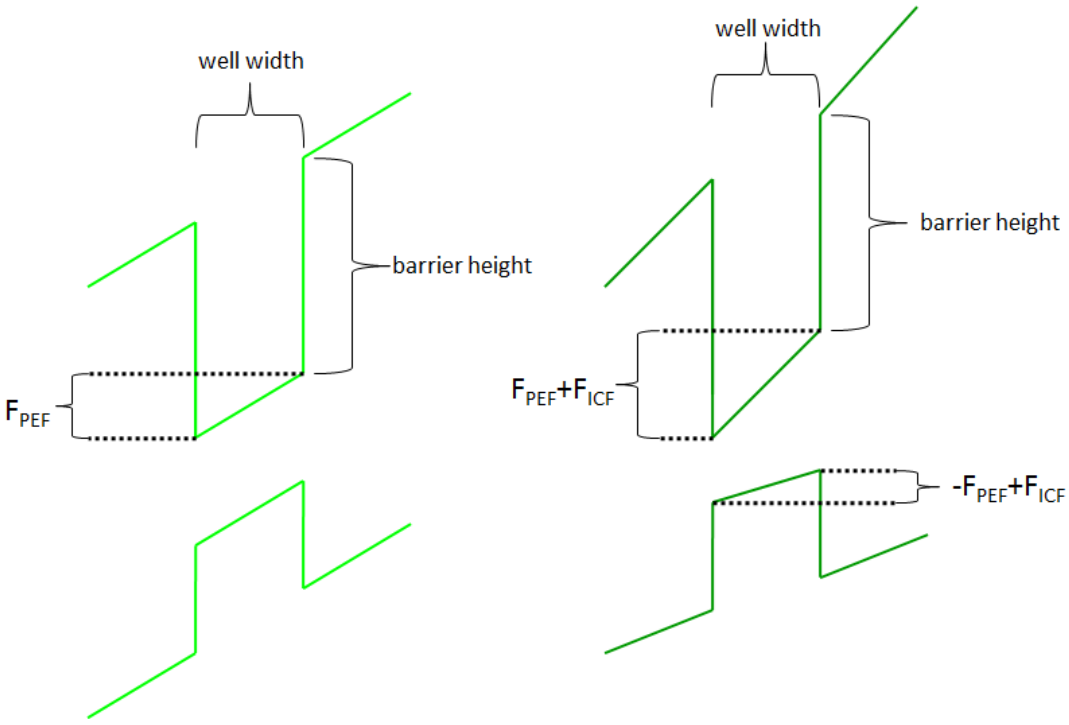

Figure 2.2.2 Potential of InGaN potential left as grown, and right with image charge field.

The image charge effect has the same effect on both types of quantum wells. The attractive electromagnetic potential of the image charge effect is summed with the potentials

of the as grown well. Thus the potential changes as $V_0 + eF_{PEF}z \rightarrow V_0 + e(F_{PEF} \pm F_{ICF})z$ for electrons (top) and holes (bottom). F_{PEF} and F_{ICF} are the electrostatic fields from the internal piezoelectric and image charge fields respectively; V_0 is the well barrier height. It should be noted a positive electric field is attractive to electrons and repulsive to holes. This causes one net electric field ($F_{PEF} \pm F_{ICF}$) to increase for electrons and decrease for holes. To the best of my knowledge this is the only case where the absolute intensity of the electric fields is different for two carriers in the same system. This causes a larger wave function separation then in the Stark effect thus a longer lifetime is expected.

The emission energy and the impact of the ICF depend on three factors: PEF, ICF, and potential barrier height. Tables of the effects of varying each of these parameters is presented while keeping the other two factors constant. Some values of the varying parameters are at the extremes of literature and beyond. This is done as a theoretical calculation to emphasize the trends of varying these parameters. On the other hand, the ranges of the varied parameter differ somewhat; this is done to keep all the situations physical. Thus only semi bound states as described in the introduction of this chapter are shown. The varied parameter are always the left most columns and highlighted, the other two columns are simulation results. For more information on the simulation see Appendix A.

Although the tables are theoretical calculations a few important conclusions may be drawn from them. When the PEF is low compared to the ICF a blue shift results. At higher relative PEF values a red shift occurs. Also a higher barrier is preferable for the blue shift to occur. It is important to note that it is possible to induce an ICF into the system of table 2.2.1 such that there will be no emission energy shift. The potential is of course altered, however the

increase of emission energy of one carrier is matched in the decrease in emission energy of the other. Deeper wells result in a blue shift, and for deeper wells a blue shift is observed.

Table 2.1.1 Potential of 1.2 eV in 60/40 well and a ICF of 2.8 10^{-3} MV cm^{-1}

Piezoelectric electric field MV cm^{-1}	Well Emission Energy (eV)	Shift from ICF (eV)
0.08	3.16406	0.00316
0.09	3.15242	0.00087
0.1	3.14064	-0.001
0.11	3.12877	-0.0025
0.12	3.11686	-0.0038
0.13	3.10491	0.00477
0.14	3.09296	-0.0056
0.15	3.08099	-0.0063
0.16	3.06902	-0.0069
0.17	3.05704	-0.0074
0.18	3.04506	-0.0079
0.19	3.03305	-0.0083
0.2	3.02104	-0.0087
0.21	3.009	-0.009
0.22	2.99694	-0.0093
0.23	2.98485	-0.0096

Table 2.1.2 Potential of 0.9 eV in 60/40 well and a ICF of 2.8 10-3 MV cm^{-1}

Piezoelectric electric field MV cm^{-1}	Well Emission Energy (eV)	Shift from ICF (eV)
0.8	3.06121	-0.0005
0.9	3.05026	-0.0006
1	3.03946	-0.00072
1.1	3.02877	-0.0008
1.2	3.01818	-0.00086
1.3	3.00767	-0.00092
1.4	2.9972	-0.00096
1.5	2.98677	-0.00101
1.6	2.97636	-0.00104
1.7	2.96595	-0.00108
1.8	2.95554	-0.00111
1.9	2.94511	-0.00114
2	2.93465	-0.00116
2.1	2.92416	-0.00118
2.2	2.91363	-0.56664
2.3	2.90306	-0.00122

Table 2.1.3 Potential of 0.7 eV in 60/40 well and a ICF of 2.8 10^{-3} MV cm^{-1}

Piezoelectric electric field MV cm^{-1}	Well Emission Energy (eV)	Shift from ICF (eV)
0.8	2.98832	-0.0009
0.9	2.97915	-0.001
1	2.97016	-0.0011
1.1	2.96129	-0.00112
1.2	2.95251	-0.00116
1.3	2.94377	-0.0012
1.4	2.93505	-0.00123
1.5	2.92633	-0.00126
1.6	2.91758	-0.00129
1.7	2.90881	-0.00131

Table 2.1.4 Potential of 1 eV in 60/40 well and a PEF of 2 MV cm^{-1}

Image charge field 10^{-3} MV cm^{-1}	Well Emission Energy (eV)	Shift from ICF (eV)
1.8	2.98832	-0.0063
1.81	2.98832	-0.00634
1.82	2.98832	-0.00637
1.83	2.98832	-0.00641
1.84	2.98832	-0.00644
1.85	2.98832	-0.00648
1.86	2.98832	-0.00652
1.87	2.98832	-0.00655
1.88	2.98832	-0.00659
1.89	2.98832	-0.00663
1.9	2.98832	-0.00666
1.91	2.98832	-0.0067
1.92	2.98832	-0.00674
1.93	2.98832	-0.00677
1.94	2.98832	-0.00681
1.95	2.98832	-0.00685

Table 2.1.5 Potential of 0.7 eV in 60/40 well and a PEF of 2 MV cm^{-1}

Image charge field MV cm^{-1}	Well Emission Energy (eV)	Shift from ICF (eV)
0.05	3.42625	-1.0069
0.06	3.42625	-1.17544
0.07	3.42625	-1.56026
0.08	3.42625	-1.72902
0.09	3.42625	-1.89076
0.1	3.42625	-2.5601

Table 2.1.6 Potential of 2 eV in 60/40 well and a PEF of 2 MV cm^{-1}

Image charge field MV cm^{-1}	Well Emission Energy (eV)	Shift from ICF (eV)
0.01	3.24767	-0.00049
0.02	3.24767	-0.00076
0.03	3.24767	-0.00077
0.04	3.24767	-0.00051
0.05	3.24767	5.48E-05
0.06	3.24767	0.000939
0.07	3.24767	0.002165
0.08	3.24767	0.003747
0.09	3.24767	0.005692
0.1	3.24767	0.008002
0.11	3.24767	0.010669
0.12	3.24767	0.013686
0.13	3.24767	0.017042
0.14	3.24767	0.020728

Table 2.1.7 PEF 0.9 MV cm^{-1} and an ICF of 2.8 10^{-3} MV cm^{-1}

Barrier height (eV)	Well Emission Energy (eV)	Shift from ICF (eV)
0.5	2.91002	-0.0014
0.6	2.94397	-0.0012
0.7	2.97915	-0.00101
0.8	3.01476	-0.00082
0.9	3.05026	-0.00063
1	3.08524	-0.00043
1.1	3.11938	-0.00022
1.2	3.15242	-1.4E-05
1.3	3.18419	0.000184
1.4	3.21457	0.000361
1.5	3.24351	0.000505

Table 2.1.8 PEF 1.5 MV cm^{-1} and an ICF of 2.8 10-3 MV cm^{-1}

Barrier height (eV)	Well Emission Energy (eV)	Shift from ICF (eV)
0.6	2.89831	-0.0014
0.7	2.92633	-0.00126
0.8	2.95603	-0.00113
0.9	2.98677	-0.00101
1	3.01807	-0.00089
1.1	3.04958	-0.00077
1.2	3.08099	-0.00065
1.3	3.11209	-0.00052
1.4	3.14267	-0.0004
1.5	3.17257	-0.00028

Table 2.1.9 PEF 2 MV cm^{-1} and an ICF of 2.8 10^{-3} MV cm^{-1}

Barrier height (eV)	Well Emission Energy (eV)	Shift from ICF (eV)
0.9	2.93465	-0.0012
1	2.96282	-0.00106
1.1	2.99172	-0.00097
1.2	3.02104	-0.00088
1.3	3.05052	-0.00079
1.4	3.07997	-0.0007
1.5	3.10922	-0.00061
1.6	3.1381	-0.00052
1.7	3.16649	-0.00042
1.8	3.19428	-0.00033
1.9	3.22136	-0.00025
2	3.24767	-0.00016

Table 2.1.10 PEF 1.8 MV cm^{-1} , ICF of 2 10^{-3} MV cm^{-1} , Barrier height 1 eV

Well Width (nm)	Well Emission Energy (eV)	Shift from ICF (eV)
4.05	2.55606	0.002297
4.1	2.54484	0.002312
4.15	2.53376	0.002327
4.2	2.52281	0.002341
4.25	2.51199	0.002354
4.3	2.50129	0.002367
4.35	2.4907	0.00238
4.4	2.48021	0.002392
4.45	2.46982	0.002404
4.5	2.45953	0.002415
4.55	2.44933	0.002425

Table 2.1.11 PEF of 1.5 MV cm^{-1} , ICF of 2 10^{-3} MV cm^{-1} , Barrier height 1 eV

Well Width (nm)	Well Emission Energy (eV)	Shift from ICF (eV)
4.05	2.5657	-0.00085
4.1	2.55535	-0.00086
4.15	2.54515	-0.00087
4.2	2.5351	0.002432
4.25	2.52518	0.002447
4.3	2.5154	0.002462
4.35	2.50574	0.002477
4.4	2.4962	0.002491
4.45	2.48678	0.002505
4.5	2.47746	0.002519
4.55	2.46825	0.002532

Table 2.1.12 PEF of 0.5 cm^{-1}, ICF 2 of 0.1 MV cm-1 , Barrier height 0.5 eV

Well Width (nm)	Well Emission Energy (eV)	Shift from ICF (eV)
4.05	2.20633	0.075109
4.1	2.20389	0.074209
4.15	2.20149	0.073323
4.2	2.19911	0.072451
4.25	2.19676	0.071592
4.3	2.19443	0.070746
4.35	2.19213	0.069913
4.4	2.18986	0.069093
4.45	2.18761	0.068285
4.5	2.18538	0.06749
4.55	2.18318	0.066707

2.2 Estimating Image Charge Intensity in Semiconductor Systems

The method of images is a mathematical trick which allows for finding analytical solutions for electrostatic fields and potentials, between a charge and a metal, which are not readily solvable. The greatest advantage of the image charge is that it is unnecessary to know the charge distribution, ρ, on a metal. Thus the method of image can only be applied to a few classes of systems with high symmetry of infinity approximations.

The geometry used for solving image charge problems in this work is the point charge and an infinite plane. Using the infinity approximation is usually justified when the lengths/areas used in the real sample differ in size by at least one order of magnitude. Using the infinity approximation in systems which do not meet this condition may be done mathematically, but it is senseless mathematically. In the current work there are two geometries used for the image charge effect: the thin film over the entire sample and semi-spherical droplets randomly assembled over the entire sample surface.

The estimated upper radius of an electron is 10^{-22} m according to the Penning Trap experiment. The thin metal film on the sample has dimensions of about centi-meters or 10^{-2} meters. Thus the metal film is about 20 orders of magnitudes larger than the electron. The surface area of contact between a metal droplet and the sample surface in this work is about 100 nm or 10^{-7} m, a difference of fifteen orders of magnitudes with the droplet being larger than the electron. Thus the infinity approximation is justified, especially if we consider that the fact that the area interface between the metal and sample and the electrons are two dimensional, thus the infinity approximation is even more justified. The other problem in the droplet samples is that there exist areas of the sample with no metal above it. The metal particle is always attractive to the charge carriers, even if the carrier is not directly underneath it. Thus there is an attractive in plane of the quantum well component to the image charge force. This attraction is more difficult to model since there is no symmetry and will be discussed later. It suffices to say that the height of these particles is much less than half the separation between the droplets (ratio less than unity) and that the ratio of the height of the particle to the distance of the carriers to the metal is about two.

Optical emission comes from the recombination of excitons or electron hole pairs. Thus to study the image charge it is necessary to consider the electron and hole simultaneously. This imposes the condition that the exciton radius may not be small compared to the distance between the exciton and the metal surface. If this condition is not met, the exciton may be approximated as a dipole which would nullify the image charge since the image charge field of a dipole is zero, or no attraction. For the plane case the location of the exciton is irrelevant. For the droplet case it is necessary to assume that the exciton is under the droplets. This is shown in figure 2.2.1 with exaggerated horizontal width larger then realistic for it be visible. It assumed that the image charge is calculated as the interaction of an electron hole pair under an infinite plane.

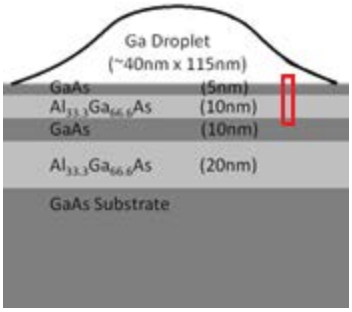

Figure 2.2.1 schematic of AlGaAs-GaAs SQW with area used to estimate image charge attraction labeled in red

Figure 2.2.2 shows the geometry of the image charge calculation for an exciton and a metal plane. The metal plane is grey and holds the 'images' of the electron and hole. The quantum well is red and shows the 'real' electron and hole.

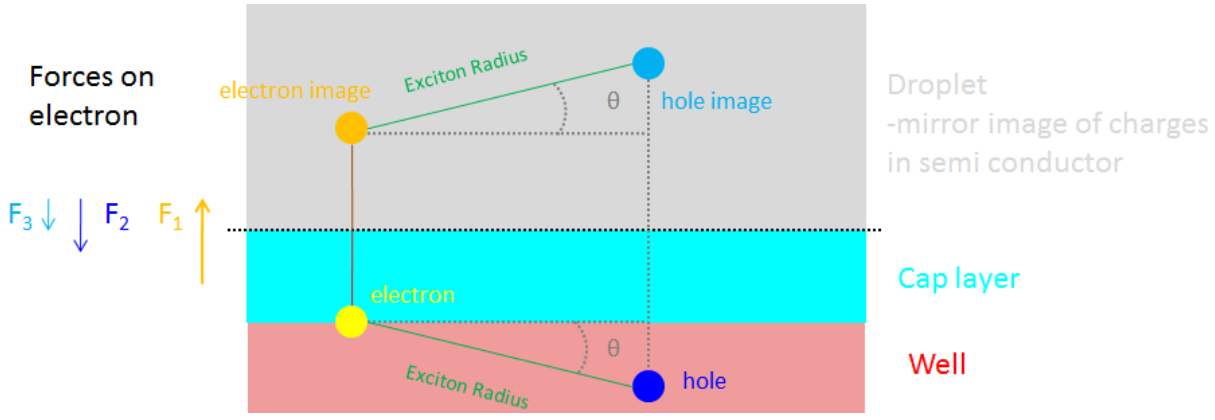

Figure 2.2.2 Schematic of image charge in semiconductor with infinite metal plane. The exciton is in the well and its image is in the metal surface.

The cap layer including the well barrier (and GaAs cap for AlGaAs-GaAs systems) is shown in cyan. The angle θ is the angle between an arbitrary in plane direction of the well and the location of the hole. The electron is assumed to be closer to the droplet arbitrary.

In the schematic in figure 2.2.2 only the electron's image is attracting it towards the metal, while the hole and hole's image are repelling it from the metal. However the hole is attracted to the metal by its image and the electron and repulsed only by the electron image. This is a consequence of the geometry and it can be assumed that the hole is on top and the number of charges attracting the carriers to the metal would switch. The forces in figure 2.2.2 may be calculated as

$$F_1 = \frac{-k}{d}. \tag{2.2.1}$$

$$F_2 = \frac{-k}{R_{ex}^2}\sin(\theta) \tag{2.2.2}$$

$$F_3 = \frac{-k}{\sqrt{(d + R_{ex}\cos(\theta))^2 + (R_{ex}\sin(\theta))^2}^2} cos\left(tan^{-1}\left(\frac{d + R_{ex}\cos(\theta)}{R_{ex}\sin(\theta)}\right)\right) \tag{2.2.3}$$

where F_i corresponds to the labels of figure 2.2.2 and is the force on the electron, k is the electric constant, and Rex is the exciton radios as labeled in figure 2.2.2. F_1 is the force on the electron from its image; F_2 is the force on the electron from the hole, and F_3 is the force on the electron from the image of the hole. F1 is the most intense force which leads to the attraction of the carrier to the metal surface.

The exciton radius may be determined from literature as the effective radius decreases as a function of well width. The narrower the QW the shorter the 'squeezed 'exciton becomes. Figure 2.2.3 shows a schematic specific to AlGaAs-GaAs wells as an example of possible and impossible arrangements of the excitons. Each line is to represent the orientation of the exciton, the length of the line corresponds to the exciton radius from literature. The red vertical line is a none-physical case where the exciton leaves the well. The yellow line corresponds to maximum exciton energy and a horizontal arrangement in the well. The exciton and its image would be arranged in a rectangle. The green lines correspond to the minimal exciton energy while the exciton is fully confined in the well. From the configuration of the green lines the angle of figure 2.2.2 is calculated. The geometry is simple; a right triangle with the exciton radius as the hypotenuse and the well height as one of its sides.

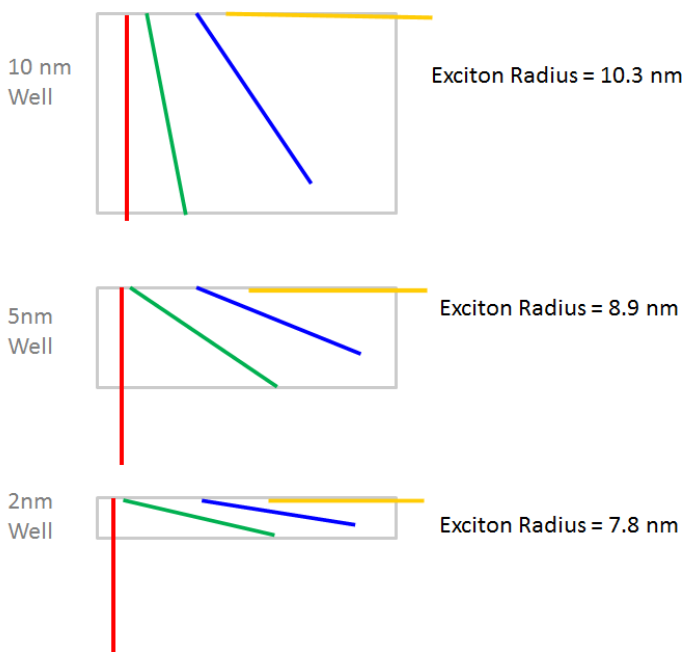

Figure 2.2.3 possible exciton arrangements for 10 nm, 5 nm, and 2 nm SQWs.

This process seems to constituently underestimate the necessary field by about ten percent. This is a very acceptable error especially since semi-classical approximations are used. Another good way of estimating the image charge is to simply consider a single carrier and its image, the result does not differ much and it is closer to matching experimental values.

Another geometry of samples which allows the study of the image charge effect on

semiconductor quantum wells is spherical metal nano particles. It is important to note that a semi sphere is very different from a sphere and the same mathematics cannot be used to model a semi sphere as a sphere. The electrostatic force on a point charge due to the presence of a none charged metallic (conductor) sphere is

$$Force = \frac{1}{4\,\pi\varepsilon_0}\left(\frac{q^2}{R^2}\right)\left(\frac{R}{z}\right)^3\left(1-\frac{R^2}{z^2}\right)^{-2} \qquad (2.2.4)$$

Where q is the charge, R the radius of the sphere, z is the distance from the center of the sphere to the point charge. The radius of the sphere is important in determining the image charge attraction between the sphere and time image charge. Figure 2.2.4 illustrates conducting spheres all the same distance away from their corresponding point charge. It is important to note that although the distance from the closest point on the sphere to the image charge is the same for all three, the distance from the center of each sphere to the point charge (z) is different in all three cases.

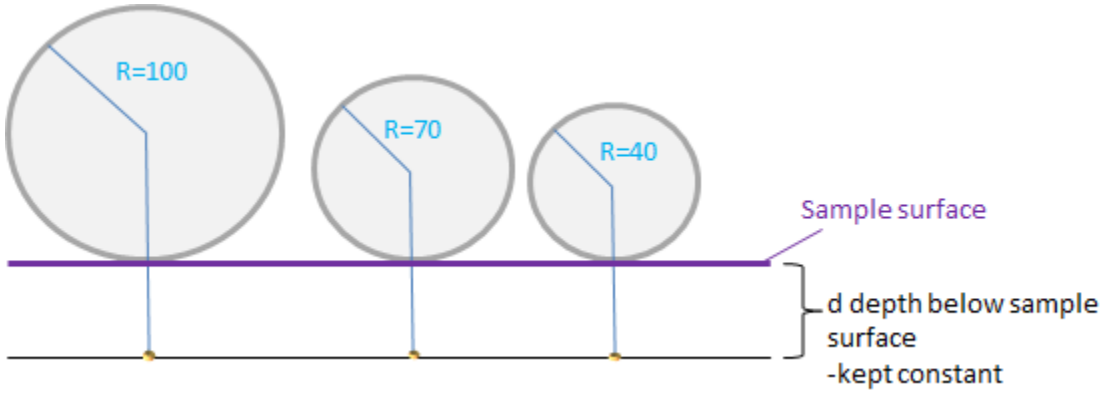

Figure 2.2.4 spheres of different radii on a plane showing the distance from their centers to a plane beneath them

Thus when the variation of sphere radius to be simulated it is necessary to remember that changing the sphere radius also changes z, the distance between the sphere center and the

point charge. Figure 2.2.5 shows the results of a simulation of the image charge potential with an uncharged conducting sphere varying the sphere radius. The top of the figure defines equation 2.2.4 in Mathematica, the plot command is used, notice that z is defined as the distance from the closest point of the sphere to the point charge (d) plus R, the sphere radius. The graph shows the dependence of sphere radius on the electrostatic image charge force.

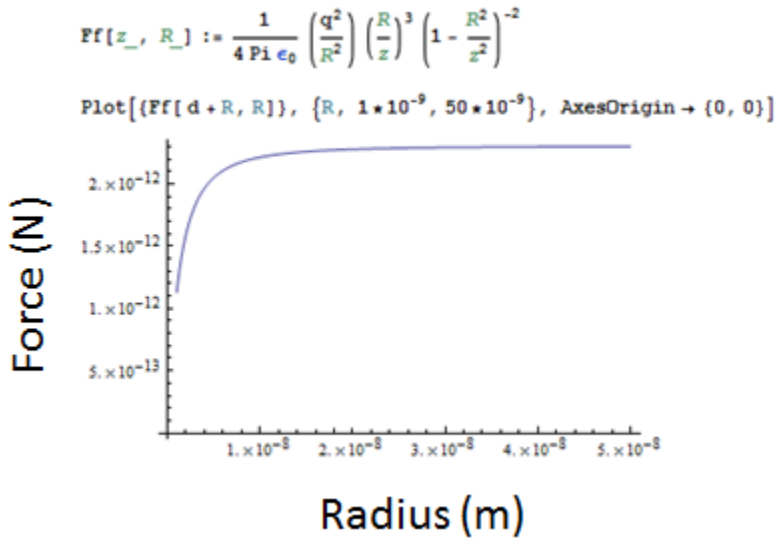

Figure 2.2.5 Simulation plot for intensity of image charge and sphere, varying the sphere radius.

2.3 Effects on Carrier Dynamics

When there is a non uniform metal surface the image charge field will have complex field lines in 3d space. This happens with the sample sets which have gallium deposited on the top. These droplets are imperfect hemispheres of varying sizes, the edges of contact between the gallium and gallium arsenide/gallium nitrite are sharp and discontinuous. In order to discuss the motion of carrier in a quantum well a set of coordinates must be established. Figure 2.3.1 shows a quantum well (blue) sandwiched between a barriers on top and bottom (red and

white). The Cartesian coordinate system is defined by the normal direction to the QW, or z axis in Fig. 2.3.1. The other two coordinates lie in the plane of the quantum well (x and y).

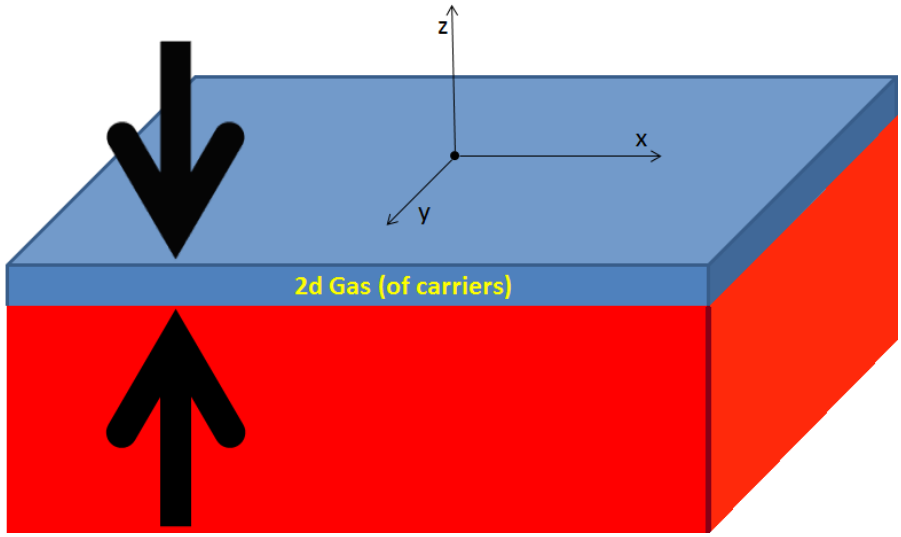

Figure 2.3.1 Coordinate grid on quantum well (blue), the barriers are red on bottom, and white (not shown) on top

It is not relevant how x and y are chosen, as long as they are mutually perpendicular with z. The quantum well is large in plane (order of centimeters) compared to all other dimensions, the z or perpendicular dimension is 'small.' More realistically it is smaller than the Bohr excition radius for the material it is made of, and of similar size as the height of the cap layer and height of the gallium droplets. Figure 2.3.2 shows a top section of a sample with a hemisphere like droplet on top. The plane of the sample surface is parallel to the plan of the quantum well, whether or not it is actually the barrier material. The GaN-InGaN wells use GaN as the barrier and cap, however the GaAs-AlGaAs wells use AlGaAs as the barrier and GaAs as a cap since a thin AlGaAs layer would react with ambient air. Since the interface between the gallium and sample surface is flat, the bottom of the gallium is also on the z-y plane and in a local region underneath the

droplet appears as a plane to the carriers in the well. Note that the system has radial symmetry from the center of the droplet hemisphere about the z coordinate.

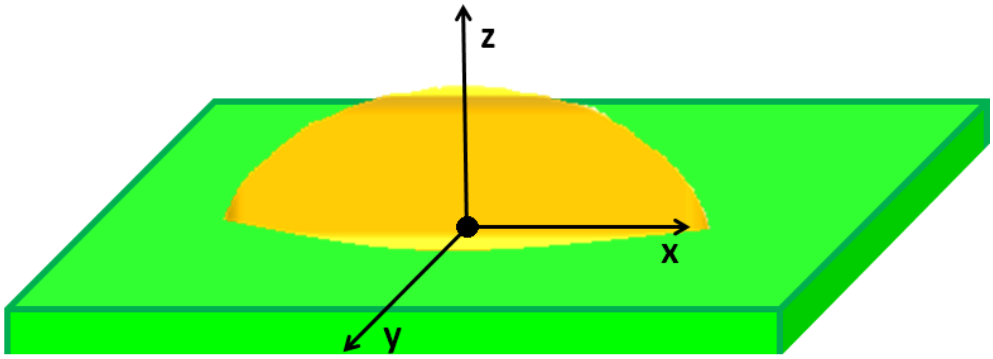

Figure 2.3.2 Schemetic of sample surface and Ga droplet on top, with coordinate axis

The system becomes more complex as carriers which are not under the droplet (to the side and below) are considered. Figure 2.3.3 shows a schematic of the GaAs-AlGaAs well looking at the system from the x-y plane. The quantum well layer has electric field vectors drawn to indicate the image charge attraction. Underneath the droplet the field lines are straight up in the z direction, as they would be for a plane or thin film. The force vectors of to the sides are have a component on the z axis, perpendicular to the well direction and a component in x and or y or the in plane component. Taking the origin of x, y as the point on top of the droplet x, y have radial symmetry and the problem may be reduced to two dimension, with z as the height / direction perpendicular to the QW and x as the

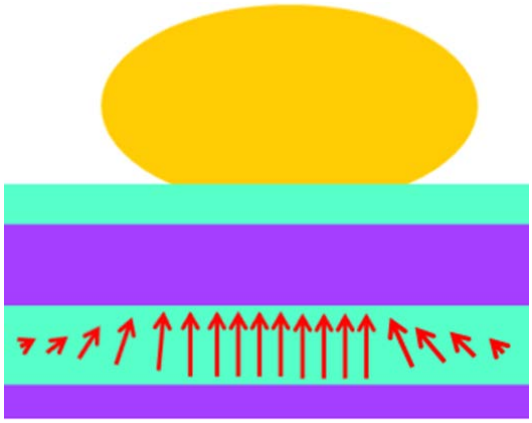

Figure 2.3.3 2d cross section of Ga-AlGaAs sample, the layer are from bottom to top: AlGaAs barrier, GaAs well, AlGaAs barrier, GaAs cap, Ga droplet. Red force vectors for the carriers are drawn in the quantum well.

orthonormal direction to z or in well component. Thus the vectors in Fig. 2.3.3 always have a positive z component, and the vectors on the usides of the droplets have components in the x direction. The above statement is obvious and basic, trivial consequences of the image charge. However estimating their magnitudes is not always trivial. The intensity of the electric field under the droplet and far from the edges tends to the image charge field of and infinite plane. This is a good approximation since the contact area of the droplet and the cap is large compared to the other relevant dimension in the problem. The attraction of the carriers outside maybe modeled as an image charge potential from a corner.

The in-plane motion of the carriers in a quantum well is often modeled as a 2 dimensional carrier gas [53, 54]. This 2DG undergoes Brownian motion. If an electric field is added to the system which is parallel to the direction of the well (perpendicular to the field needed for the Stark effect) the electric force acts as a bias for the Brownian motion inducing a net drift velocity on the carriers. Thus an average exciton in the ensemble obeys the Itō distribution [56]:

$$dx = \alpha(x,t)dt + \beta(x,t)dz \tag{2.3.1}$$

where x is the position of the particle, α is the drift coefficient, and ß is the variance. This is a process of drift and diffusion which depends on position and time. Taking the x coordinate to be positive and the edge of the droplet to be at the origin, all carriers will drift towards the particle's edge. The biasing force is provided for the in plane component of the image charge field, $F_{ICF}^{\parallel}$. It is important to remember that $F_{ICF}^{\perp}$ is responsible for the PL energy shift which is analogous to the Stark Effect. α is estimated to be $\alpha_0 \times \mu \times F_{ICF}^{\parallel}$ or $\alpha_0 \times v_d$ where α_0 is a unitless scaling constant and v_d is the drift velocity. μ is the mobility of the carriers. The mobility differs

greatly between InGaN and GaAs which are the well materials in this work. It is also dependent on temperature and to a lesser extent on carrier density. The carrier density dependence is irrelevant for this work as it is done in the gas limit, or at low densities. This approximation is in no way unrealistic with the equipment used for experiment, and it is very rare that it is invalid for gallium arsenide.

2.4 Case Study in Semiconductors

The image charge effect manifests itself optically in four ways in semiconductor quantum wells. It causes a shift in emission energy, an increase in recombination lifetime, a change in photoluminescence intensity, and a none linear excitation power dependence. In order to study the effects of image charges on semiconductor quantum wells two sets of samples were created. They were single quantum wells of GaAs-AlGaAs and GaN-InGaN.

The shift in energy is best described by the alteration of the confinement potential as described in section 2.1. Fig. 2.4.1 shows the experimental results for a 10nm AlGaAs SQW at 15K excited with a 442 nm HeCd laser. The change in potential is represented in Fig. 2.1. The AlGaAs system in this work is modeled as fallows: the barrier heights are 0.287eV and 0.123eV

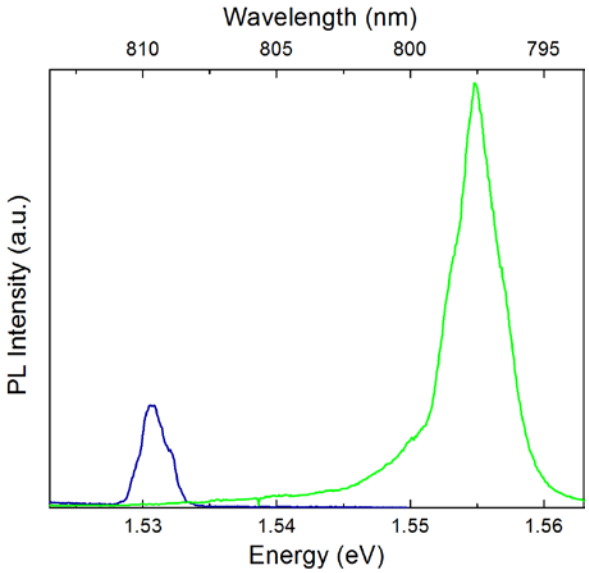

Figure 2.4.1 PL Spectra of AlGaAs QW (blue) and AlGaAs QW with image charge effect (green) at 15 K

for the electron and hole respectively, the used quantum well widths are 2, 5, and 10nm. Thus it is possible to solve for the reference system (without the gallium droplets, or blue spectral shape in figure 2.4.1. The Hamiltonian and wave function are thus:

$$H_{well}^{(ref)} = \frac{-\hbar^2}{2m^*}\frac{d^2}{dx^2} + V_0 \tag{2.4.1}$$

$$\Psi_{\text{well}}^{(\text{ref})} = a_1 \sin(\kappa\, x) + b_1 \cos(\kappa\, x) \tag{2.4.2}$$

These are ofcourse the simple square solutions for a finite quantum well where m* is the effective mass. In order to calculate the ICF the image charge interactions between a pair of point charges and a plane are used. The electrostatic force, eF, in the present system is well approximated semi classically. The dipole approximation in this system is impermissible due to the thin cap layer compared to the exciton radius. Since a narrower well causes greater shrinkage of the exciton wave function in both the parallel and perpendicular direction [contour] the geometry of the exciton, thus the location of the image charges, must very with well width. In the fully quantum mechanical treatment of the image charge effect the image charge and exciton Hamiltonians must be solved simultaneously with the confinement Hamiltonians. However, previous results allow for approximate solutions based on the average exciton from the ensemble. Effective exciton radii (R_{ex}) for GaAs-AlGaAs QWs are tabulated by Someya et. al. [26], using these values along with the constraints that the exciton must be confined inside the well and the ground energy be minimized the geometry of the system may be estimated as an interaction of the average exciton inducing an image charge on the contact plane of the Ga droplet, which is at least an order of magnitude larger than the exciton. The difference in the perpendicular positions of the electron and hole (z_e and z_h) is described by

$\theta = sin^{-1}\left(\frac{z_e - z_h}{R_{ex}}\right)$, thus θ = 0 for $z_e = z_h$ and the maximum value of θ is a function of the well width and exciton radius of each well. F, the electric field, is thus obtained by solving the system of charges in a dielectric media and e is simply the electron charge. An electron (hole) is attracted by its own image while being repelled by the image of hole (electron) thus the relative electron and hole positions affect the net force. Thus the AlGaAs SQW system may be modelled with the image charge effect using a Hamiltonian and wave functions as fallows:

$$H_{well} = \frac{-\hbar^2}{2m^*}\frac{d^2}{dx^2} + (V_0 + eFx) \tag{2.4.3}$$

$$\Psi_{\text{well}} = a_1\,\text{Ai}\left(-\left(\frac{2m^*}{(\hbar eF)^2}\right)^{1/3}(E - eFx)\right) + b_1\text{Bi}\left(-\left(\frac{2m^*}{(\hbar eF)^2}\right)^{1/3}(E - eFx)\right) \tag{2.4.4}$$

Notice that because of the condition that both electrons and holes are attracted to the image charge potential the wave function delocalization is much less than in the Stark Effect. The modeled and experimental emission energy shifts are presented in figure 2.4.2. The primary source of discrepancy between the experiment and theory is the assumption of a constant field within the well which leads to an increase in the calculated electrostatic energy but allows the well potential to remain linear instead of hyperbolic (1/z as the electrostatic potential). This discrepancy is thus more apparent for wider wells since more curvature is flattened. Secondly the oscillator strength and interactions between the well and barriers [barriers] are not considered semi classically. These effects cause a decrease in the

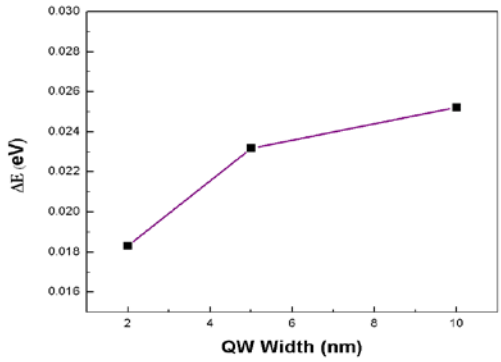

Figure 2.4.2 Modeled shift (line) and experimental shift (square) in AlGaAs SQWs

relative strength of the electrostatic interaction and manifest more clearly in narrower wells.

Because of its square well potential AlGaAs can only experience a blue shift from the image charge effect. InGaN may experience either a blue or red shift, as tabulated in section 2.1. InGaN's built in PEF is well studied and it was shown that an externally applied electric field may be used to increase the internal electric field in the well resulting in a red shift, or the external field may counteract the PEF resulting in a blue shift. The image charge field (ICF) is distinct from the PEF or an externally applied field in that, for low carrier concentrations, both electrons and holes experience an attractive potential while the other fields attract one type of carrier while repelling the other depending on field bias. This unique feature of the image charge leads electrons and holes to experience effective electric fields of different intensities while in the same system with a none zero PEF. Adding an external field will also result in attractive and repelling forces being equal in magnitude. In the image field for a system with an internal PEF an equal attractive force is added to both the attracting and repulsing fields resulting in different absolute intensities for each carrier. For semiconductors with no natural PEF, such as AlGaAs the intensities of the electric fields would be the same for both carriers.

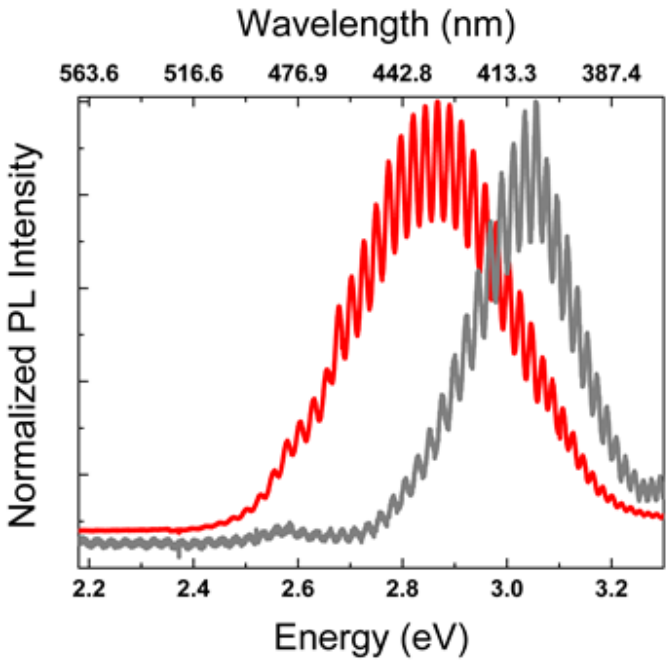

Figure 2.4.3 PL for InGaN SQW (grey) and same well with gallium droplets (red)

Figs 2.4.3 and 2.4.4 show experimental evidence for the image charge induced red shift and blue shift respectively. It is important to remember that for both gallium and gold induce the image charge effect virtually identically and their plasmon frequency is irrelevant to the result. InGaN, however, is a very sadly messed up material and there is no real consensus on its bandgap energy nor piezo electric field. This is the reason any calculation analogues to those for the AlGaAs system would be speculation at this point. The theoretical background showing the possibilities are tabulated in section 2.1. It is left to the interested reader to generate numerical results, for which there are infinitely many permutations of InGaN bandgap and PEF to satisfy the shift of figure 2.4.4. The Hamiltonian is the same for both the as grown InGaN SQW and InGaN SQW with the image charge effect except that the electric field changes as F = F_{PEF} for the as grown to F = F_{PEF} + F_{ICF} for the image charge case. Thus the Hamiltonian is the same as that for the image charge effect AlGaAs SQW and the total wave function is

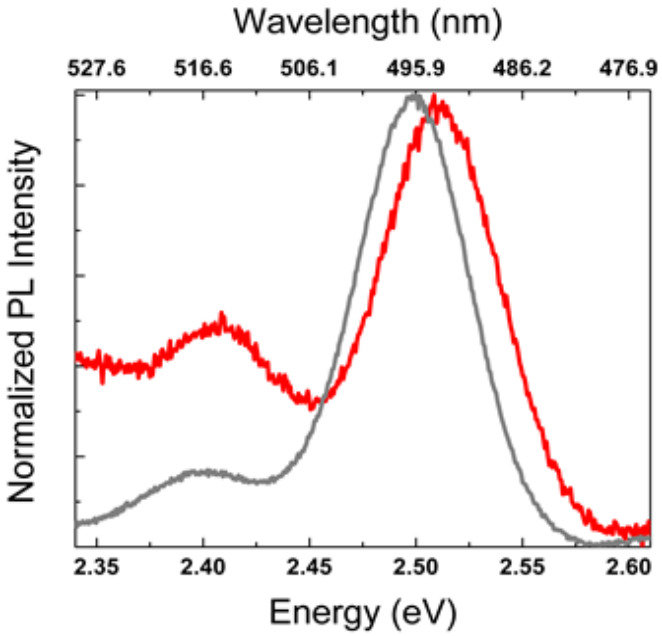

Figure 2.4.4 PL for InGaN SQW (grey) and same well with gold thin film (red)

$$\Psi = \begin{cases} a_1\left(\boldsymbol{i}\,\mathrm{Ai}\left(-\left(\frac{2m^*}{(\hbar eF)^2}\right)^{1/3}(E-V_0-eFx)\right)+\mathrm{Bi}\left(-\left(\frac{2m^*}{(\hbar eF)^2}\right)^{1/3}(E-V_0-eFx)\right)\right) & z<-\frac{L}{2} \\ a_0\,\mathrm{Ai}\left(-\left(\frac{2m^*}{(\hbar eF)^2}\right)^{1/3}(E-eFx)\right)+b_0\mathrm{Bi}\left(-\left(\frac{2m^*}{(\hbar eF)^2}\right)^{1/3}(E-eFx)\right) & -\frac{L}{2}\le z\le\frac{L}{2} \\ a_2\ \mathrm{Ai}\left(-\left(\frac{2m^*}{(\hbar eF)^2}\right)^{1/3}(E-V_0-eFx)\right) & z>\frac{L}{2} \end{cases} \quad (2.4.5)$$

remembering that F is calculated different for the image charge case and none image charge case. Of course the intensity of the image charge attraction is calculated the same for all hybrid semiconductor/metal system.

It is also worth noting that Ψ is technically a semi bound state. The potential decays to zero as z tends to infinity, however the tunneling probability is very low and carriers will de-excite by recombining in the well with much higher probability then tunneling out of the confined region. The possibility of loss of internal efficiency due to tunneling may not be discounted however. Although it is much more probably that the intensity is affected by the wave function delocalization.

Up to this point this section only dealt with comparisons at the same temperature and ignored carrier dynamics. As a reference starting point data for temperature dependent 10 nm AlGaAs SQW with 442 nm excitation is shown in figure 2.4.5. It is important to observe that there is negligible if any shift in the quantum well emission peak as a function of temperature. This is indicative of strong quantum confinement in a well grown hetero-structure. The same QW wafer with deposited gallium droplets shows a large energy shift as a function of temperature shown in figure 2.4.6. It is interesting to note that the energy in Fig. 2.4.6 converges to the well emission energy in

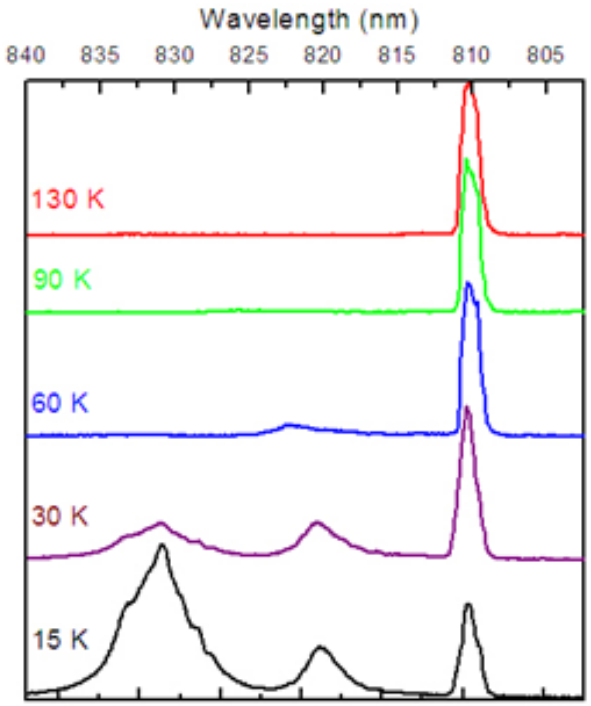

Figure 2.4.5 Temperature dependent spectra of 10 nm AlGaAs SWQ without image charge effect excited with 442 nm

Fig. 2.4.5. The excitation used for figs 2.4.6 – 2.4.8 is 532 nm as the reference system PL. This behavior is consistent for all three wells in the set, and figs 2.4.7 and 2.4.8 show the temperature dependent shift for the 5 nm and 2 nm SQWs respectively. The amount of energy shift is less for narrower wells as predicted in section 2.1 and shown in figure 2.4.2. Thus the model and data agree on the same trend which is good support for the model. A similar behavior is observed for multiple quantum well structures. The multiple AlGaAs quantum well structure shows less of a pronounced shift for two reasons. First is the distance from the bottom wells to the gallium droplets. The image charge effect is an inverse square law and distance, especially for weak fields, is a very important parameter. The second is that at each interface of the multiple quantum well structure does induce an image charge potential, albeit small, it is still present at each interface. Figures 2.4.10 and 2.4.11 show the CW temperature evolution of the MQW AlGaAs samples.

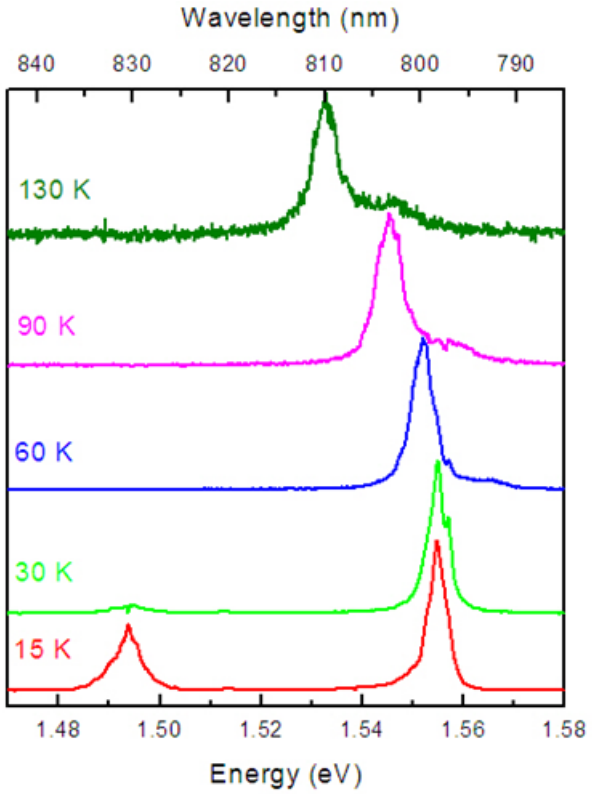

Figure 2.4.6 Temperature dependent spectra of 10 nm AlGaAs SWQ with gallium droplets (image charge effect) excited with 442 nm

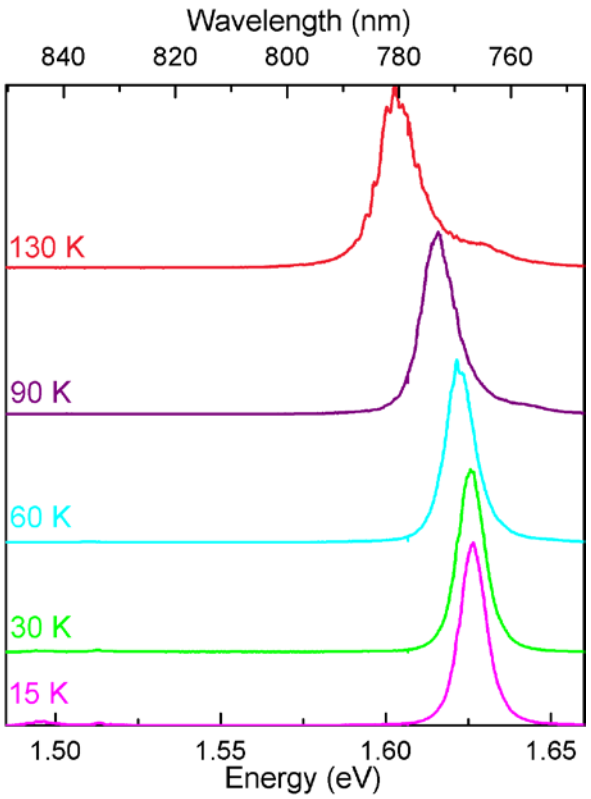

Figure 2.4.7 Temperature dependent spectra of 5 nm AlGaAs SWQ with gallium droplets (image charge effect) excited with 442 nm

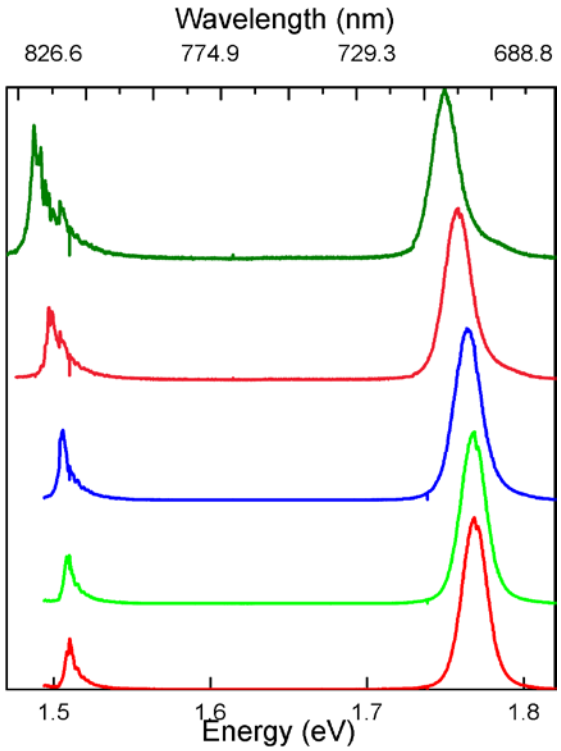

Figure 2.4.8 Temperature dependent spectra of 2 nm AlGaAs SWQ with gallium droplets (image charge effect) excited with 442 nm

Figure 2.4.9 Temperature dependent spectra of 1.5 nm AlGaAs SWQ with gallium droplets (image charge effect) excited with 442 nm

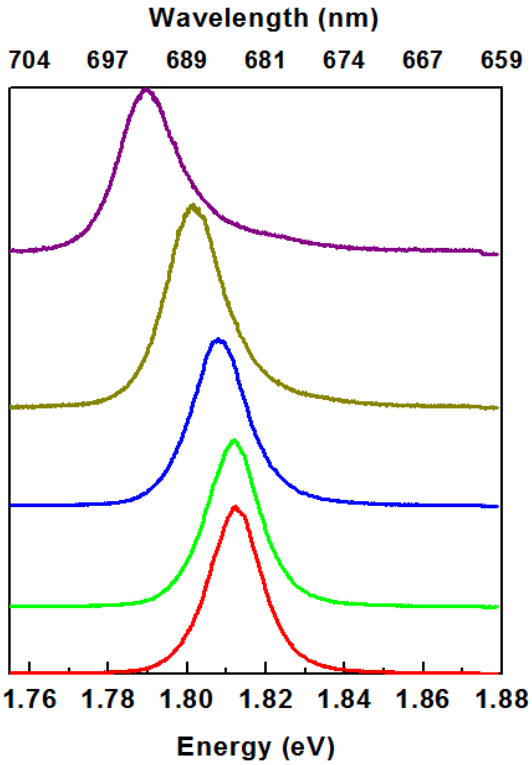

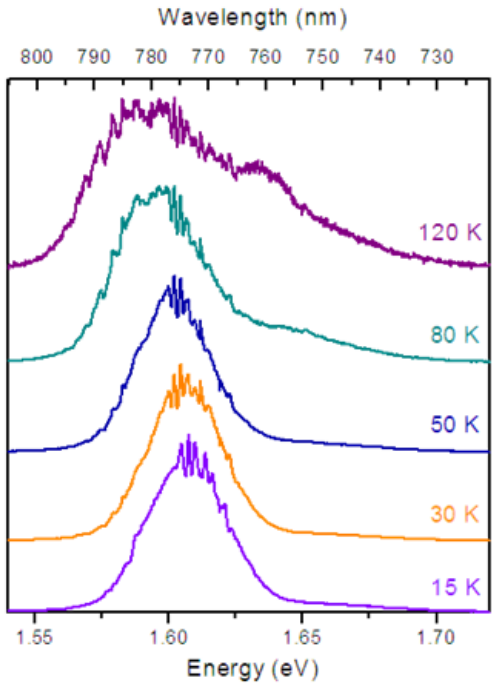

Figure 2.4.10 Temperature dependent CW PL for AlGaAs MQW with gallium droplets

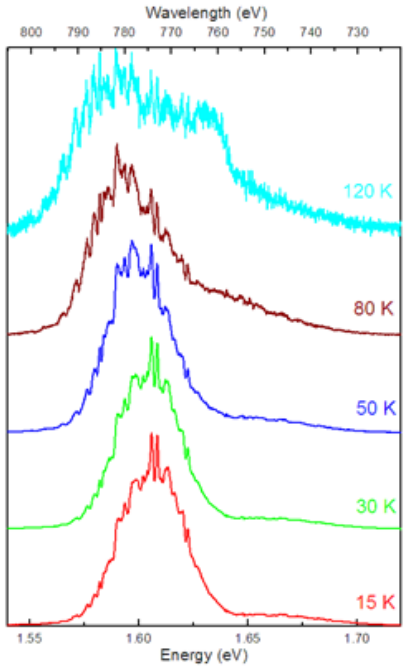

Figure 2.4.11 Temperature dependent CW PL for AlGaAs MQW without gallium droplets

The most pronounced difference in the two samples is enhancement from the gallium droplet sample. The high energy shoulder becomes less intense with rising temperature slower than the rest of the signal. However it is important to observe that the spectral shapes for the MQW sample bulges to the higher energy part of the spectrum, thus showing a blue shift analogous to the SQW samples. This sample also exhibits different behavior due to different excitation excitation wavelength Fig. 2.4.12. This is due to carriers being excited higher in the valance band and having a probability of recombining at different energies. Carrier dynamics

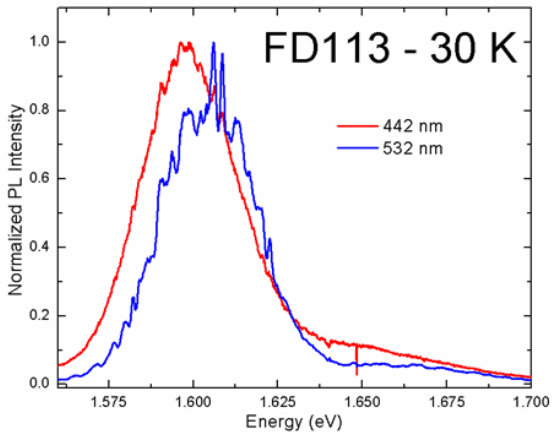

Figure 2.4.12 CW PL spectra of MQW AlGaAs with 442 nm excitation (red) and 532 nm excitation (blue)

are also affected by the excitation energy, which should come as no surprise. Since a higher excitation energy excites carriers higher into the conduction band. In general higher excitation energies increase the FWHM of quantum well structures.

AlGaAs is an excellent material for the study of the image charge effect because it has a long exciton radius of 10 nm. This is why the shifts in the temperature dependent data are so pronounced and easy to observe. InGaN has a smaller exciton radius, 3.4 nm, which is less preferable to the study of image charge effects on semiconductors. Furthermore the InGaN samples for this study were fabricated with a higher cap layer then the AlGaAs samples. For the above reasons the temperature dependent shift in the presented InGaN sample is not as large as the AlGaAs and converges to the none image charge case more rapidly.

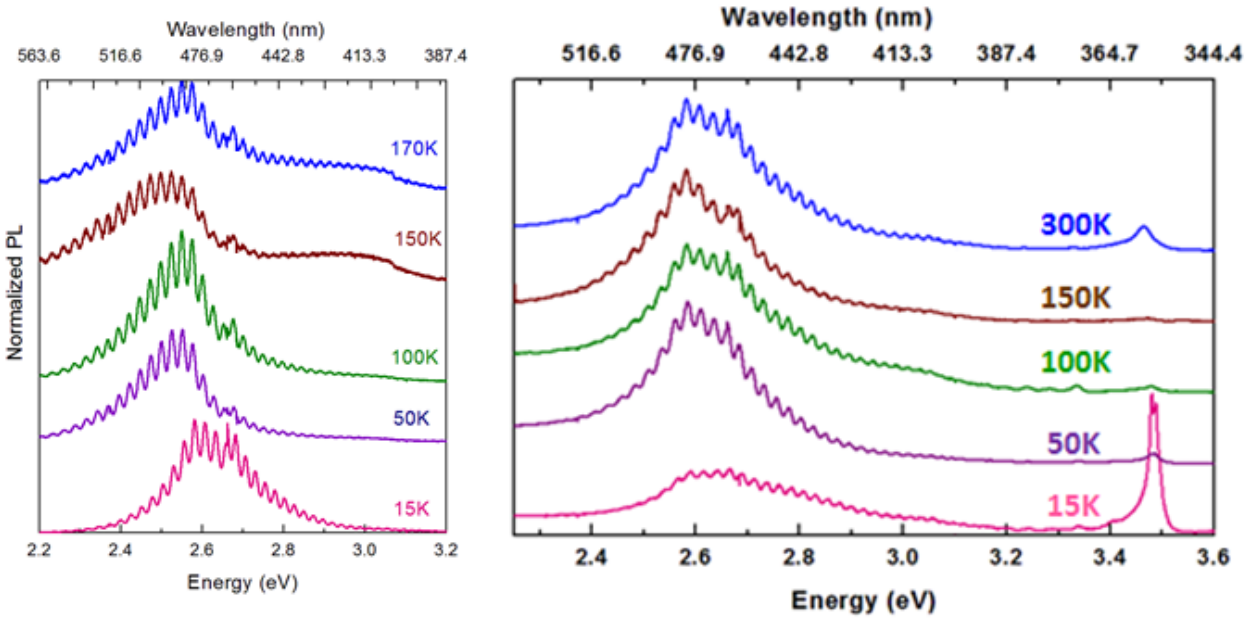

Figure 2.4.13 CW PL sectra of InGaN SQW without droplets (right) and with droplets (left)

Figure 2.4.13 shows the CW temperature evolution for the gallium droplet covered well and the bare well. The droplet sample has a lower intensity mostly due to the fact that it was front excited and the gallium droplets are so dense that the metal block a majority of the sample

surface. This however allows the plasmons modes on the droplets to couple creating higher plasmon energy, which is important for the fallowing chapters. The PL specta of the droplet sample also shows the bulk GaN peak at 3.48 eV for reference.

Figure 2.4.14 shows the CW spectra of three InGaN SQW samples with and without a gold thin film deposited on them and the fitted model for their energy shift (see section 2.2.1). This sample set has varying well widths of 4.05 nm, 4.30 nm, and 4.55 nm.

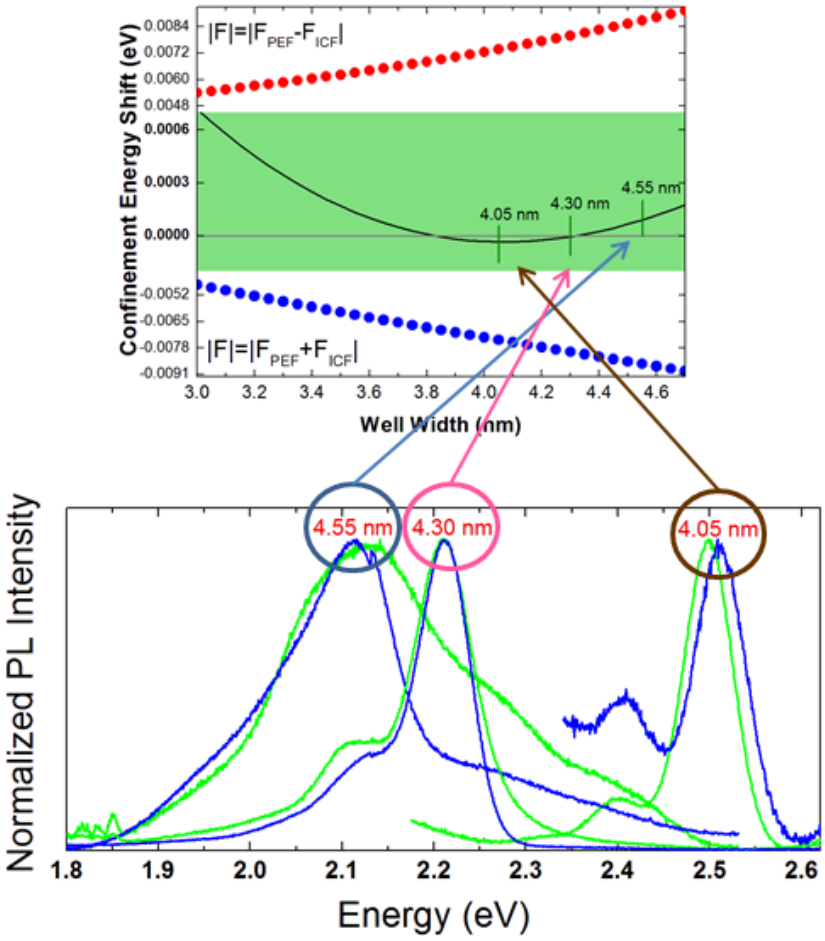

Figure 2.4.14 PL spectra for three GaN-InGaN SQW showing the shift in energy between gallium droplets covered samples and bare samples (bottom). Simulated prediction of energy shift from model (top)

In the CW PL spectra the blue curves are the gold film covered wells (with the image charge effect) and the green curves are the bare SQWs. Some of the quantum wells may couple via

plasmons to gold, but that is discussed elsewhere. This sample set is of particular interest because the gold covered wells red shift relative to the reference (4.55 nm well), blue shift relative to the reference (4.05 nm well), and show negligible shift relative to the reference well (4.30 nm well). All these samples were fabricated in the same facility with identical indium incorporation, and the gold films were deposited identically. Thus the varying shifts in energy do not originate from the fabrication process. This behavior is identical to the predicted behavior of section 2.1 with a somewhat lower magnitude in the shift. The top of figure 2.4.14 show simulation results for the image charge potential alterations. The top of the graph (red dots) is the change in energy the electrons and bottom (blue dots) is the change in energy of the holes. The solid black line represents the only observable on the graph, the sum of the energy shift of electron and holes. The shift is plotted versus well width, and the three tick marks correspond to the experimental data of widths 4.05 nm, 4.30 nm, and 4.55 nm. The theoretically predicted behavior is the same as the experimental result, and shows both the red shift, blue shift, and negligible shift. The PL peak pairs for the gold covered and bare samples of the same well width are circled and point to the theoretical model plot for reference.

The internal piezoelectric field in GaN-InGaN partially originates from the stress of the lattice mismatch and relaxes as the growth of one compound continues. Thus narrower wells tend to have a greater internal electric field, even if all other growth parameters are kept constant [45]. Taking this behavior into account increases the correlation between the experiment and theory parts of figure 2.4.14. The image charge effect is dependent on the intensity of the electric field in the sample (the mathematics and theory do not care whether this field if the piezoelectric field or an externally applied field). Figure 2.2.15 shows the

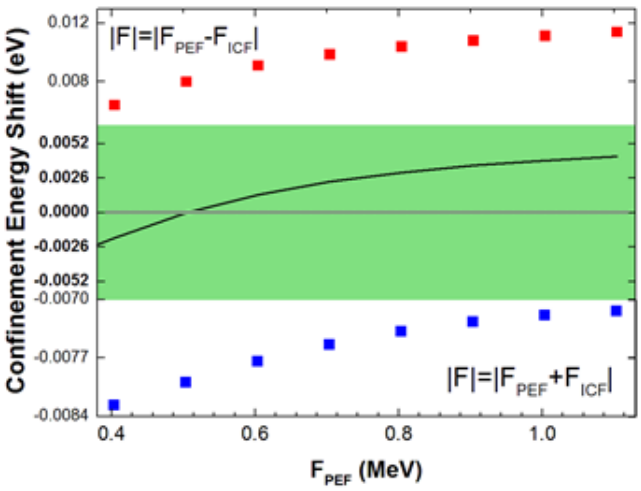

Figure 2.4.15 Simulation of energy shift in InGaN QW versus PEF resulting from adding an image charge field induced by a non-uniform metal layer on the well cap for a 4.30 nm SQW. The electron energy (RED) decreases since its well becomes more triangular (triangle) and the hole energy (triangle) increases as its well becomes more flat. The effective sum of the electron and hole energy (solid line) shift is observed in PL and drawn as a black solid line.

dependence of the image charge induced energy shift versus the electric field. As the electric field increases the magnitude of the energy shift of both electrons and holes increase. Thus as the narrower wells have a larger piezoelectric field they shift more than predicted in figure 2.2.13. Of course the intensity of the image charge potential also affects the behavior of the system. Its alteration on the energy shift is presented in figure 2.2.16.

The discussed energy shifts occur as a result of band bending and the alteration of confinement potentials in the presented quantum well systems. This causes a reduced wave function overlap and thus an increase in recombination lifetime. In the case of quantum well systems which are only partially covered with metals the 2D carrier gas drifts towards the metal islands as a result of the image charge attraction. This drift causes a larger increase in carrier concentration in the vicinity of the metal droplets.

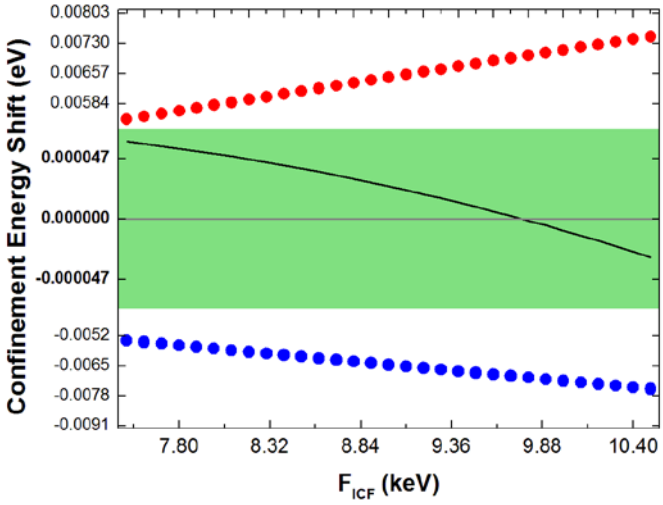

Figure 2.4.16 Simulation of energy shift in InGaN QW versus ICF resulting from adding an image charge field induced by a non-uniform metal layer on the well cap.

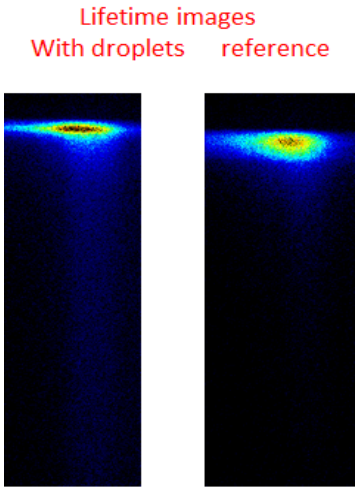

Figure 2.4.17 Streak image of growth defect peak with droplets (right) and without droplets (left)

The result is somewhat contradictory since the increase in carrier concentration in the vicinity of the droplet should result in a faster recombination rate. Figures 2.4.17 and 2.4.18 show a comparison of lifetimes of the defect peak from the quantum well growth and bulk gallium arsenide peak respectively. It should be noted that in both instances the lifetime noticeably increases for the droplet covered samples. It was not possible to acquire similar data for the quantum well peak due to instrumental shortcomings and in sufficient sensitivity. The quantum well lifetimes do have the same behavior for the reasons previously discussed. Figure 2.4.19 shows the exponential(s) decay graphs for the defect related peak. This provides a better comparison then the streak data.

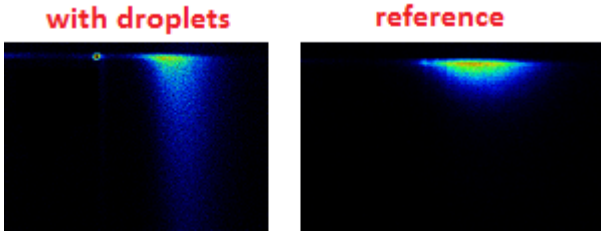

Figure 2.4.18 Streak image of growth bulk GaAs peak with droplets (right) and without droplets (left)

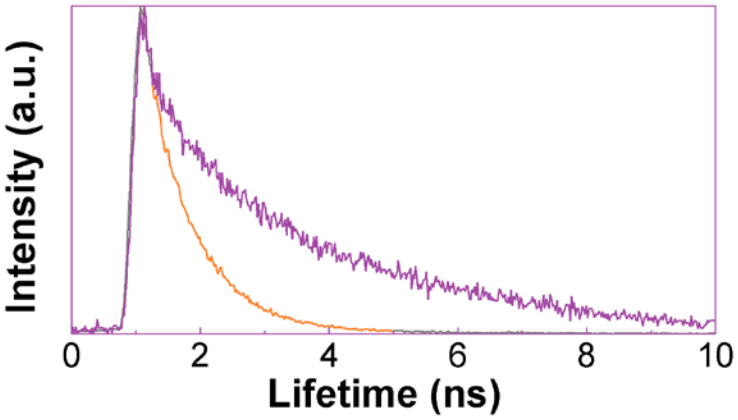

Figure 2.4.19 Lifetime decay curves from image charge sample (purple) and reference sample (orange) of the defect peak in GaAs-AlGaAs SQW.

The intensity saturation behavior is shown in figure 2.4.20. The data for the uncoated SQW well is taken from Semaltiano et. al [28]. Since the metal surfaces attract excitons and are not uniformly distributed, excitons may migrate closer to the gallium droplets in the plane of the well. Thus resulting in greater local concentration of excitons. PL intensity is inversely proportional to the lifetime and directly proportional to the carrier concentration, thus the intensity of the current system is enhanced by the localization of excitons near the metals and suppressed by the increased lifetime. The PL enhancement is thus explained by greater concentration of carriers.

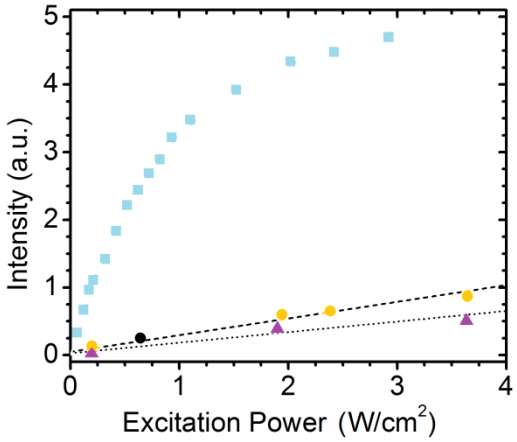

Figure 2.4.20 Power dependence of gallium covered GaAs-AlGaAs SQW and reference system from source 23 of as grown GaAs-AlGaAs SQW.

As the concentration of charged carriers increases the effective image charge field ceases to increase due to image charge cancelation from electrons and holes in close proximity. This can be seen experimentally by measuring the PL Intensity as a function of excitation power, figure 2.4.20. Increasing excitation power increases the amount of carries available for recombination thus the luminescence intensity is expected to increase linearly with increased excitation intensity as it does for the reference sample. However, with the electrostatic image charge effect, the image charge electric field ceases to increase above a certain carrier concentration. Fig. 2.4.20 shows a common AlGaAs-GaAs QW power dependence for various well widths (triangle and square)

which, in contrast to QWs with image potentials, is linear [23]. This maximum electric field intensity is decided by the geometry of the metal surfaces. For continuous smooth surfaces this saturation occurs at negligibly small field intensities.

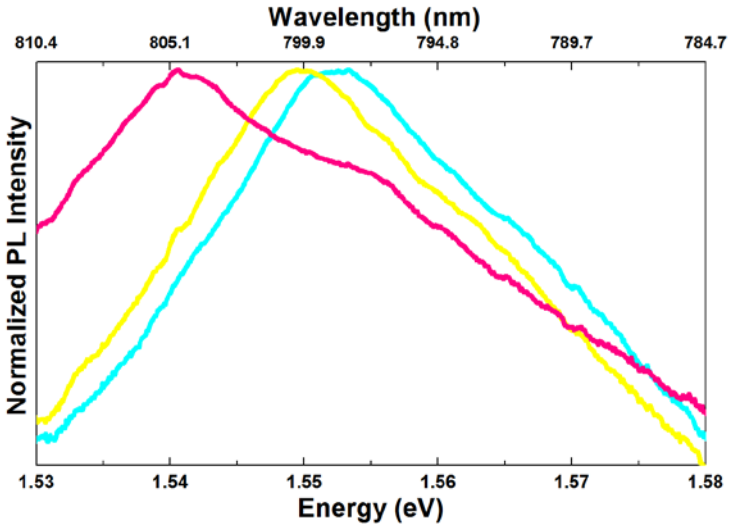

Figure2.4.21 Normalized PL spectra of 10 nm GaAs-AlGaAs SQWs with cap layers of 5 nm (cyan) 7 nm (yellow), and 20 nm (magenta).

Another important piece of evidence of the image charge effect is the quadratic dependence of the ICF as a function of the distance between the active well region and the metal. For this 3 identical 10 nm single quantum wells were created, only varying the GaAs cap layer height. Thus it is expected that the ICF intensity decreases as an inverse square law of the distance. To observe this the PL energy shift is studied as a function of cap layer height. Figure 2.4.21 shows the normalized PL spectra of the same to 10 nm GaAs-AlGaAs SQW structure with 5 nm, 7 nm, and 20 nm cap layer heights (with gallium droplets deposited on each wafer). The intersection of the line shapes on the right is attributed to random experimental noise as the intensities of all samples vary. Figure 2.4.22 shows the experimental energy shift and theoretical simulations using equation 2.4.4 and the theory introduced in the preceding chapters plotted. F, the electric field is calculated using the formulations described in this work, and the invers squares of 5, 6, and 10 are highlighted with starts in Fig. 2.4.22. This is done to emphasize that the energy shift in a transcendental function and it does not depend directly on any one of its parameters. The

similarity of figures 2.4.16 and 2.4.22 is expected since both vary the ICF intensity, although one is fitted for GaN-InGaN and the other is for GaAs-AlGaAs. Altering the confinement potential is the same mathematically for the two systems; however other variables, such as mobiilyt and diffusion, are trivially applied to both material systems. The cyan curve, which is somewhat linear, is reminiscent of the curved of section 1.3. This should be obvious since the mathematics of the Stark Effect and the image charge effect are practically the same.

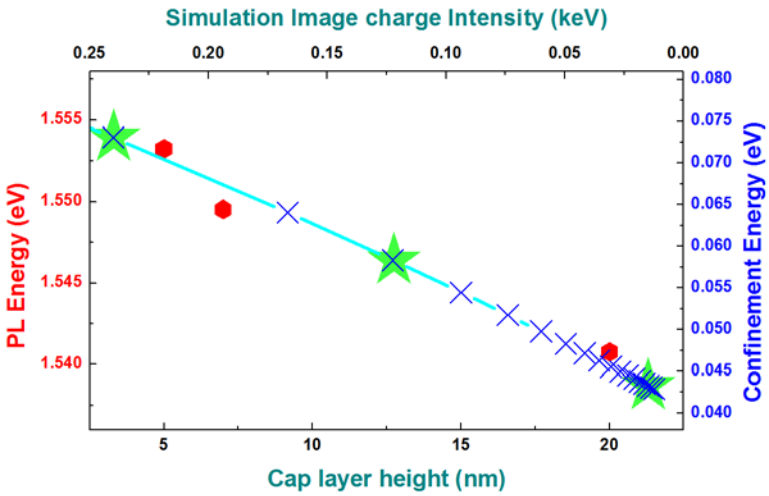

Figure 2.4.22 Experimentally observed emission energies of GaAs-AlGaAs SQWs as a function of cap layer height (red circle). Simulation results of confinement energy in GaAs-AlGaAs SQWs using image charge theory (cyan line and blue crosses). Green stars highlight field intensities of $F_0/5^2$, $F_0/7^2$, and $F_0/20^2$ for observation of the observed trend.

2.5 Temperature Dependence of the Image Charge Effect in Inhomogeneous Field Systems

The temperature dependent evolution of inhomogeneous image charge systems depends on both the parallel ($F_{ICF}^{\parallel}$) and perpendicular ($F_{ICF}^{\perp}$) components of the ICF. The perpendicular component leads to the change in emission energy and affects the lifetime, the parallel component leads to enhancement and also contributes to the lifetime changes. Since there are regions covered with metal, and regions not covered in metal the ICF is none uniform across the QW, although it must be noted that the both components decrease and increase togather. The distance dependents of the ICF on distance is a continuous inverse square law

and is not quantized, this leads to the continuous Itō distribution described in section 2.3. Figure 2.5.1 shows a schematic of the sample surface with a gallium droplet and the field intensity and confinement potentials as a function of distance.

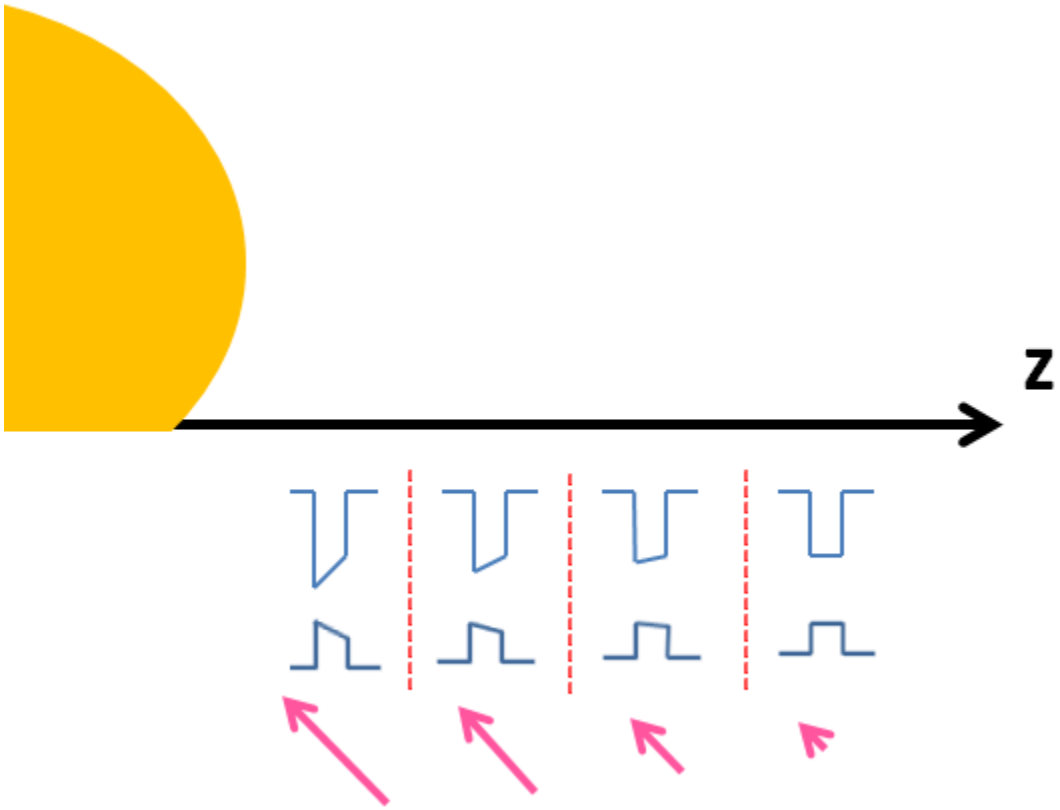

Figure 2.5.1 Top: schematic of a sample surface of a sample with inhomogeneous metal nano particle distribution. A metal nano droplet is at the origin of the z axis (yellow). The z value increases from left to right. Below are schematics of confinement potentials (blue) at different z values showing the evolution of the of an image charge potential on a square well such as for GaAs-AlGaAs QWs. Red line seperators are only present for aesthetics. Bottom magenta arrows representing the magnitude and direction of the image charge attraction.

It is necessary to consider only the perpendicuar component when calculating the depth of the confinement potentials. The emission energy is a transindental function of the field intensity and differs relative to intensity much as the Stark effect discussed in the introduction.

Figure 2.5.2 shows the temperature evolution of the reference and gallium covered samples. First of all it is important to note that as the temperature increases the image charge

sample emission energy tends to the reference sample energy, only its FWHM is greatly increased. This is all explained by the Itô distribution described in section 2.3.

$$dx = \alpha(x,t)dt + \beta(x,t)dz \tag{2.5.1}$$

where α is the drift coeficient and β is the variance. For the reference sample the variance is mostly independent from temperature, i.e. the FWHM does not change significantly. The reference sample also has a drift coewficient close to zero, i.e. there is no significant change in the emission energy. Thes observations are common for high quality SQWs. When the ICF is introduced into the well however, both α and β are drastically changed.

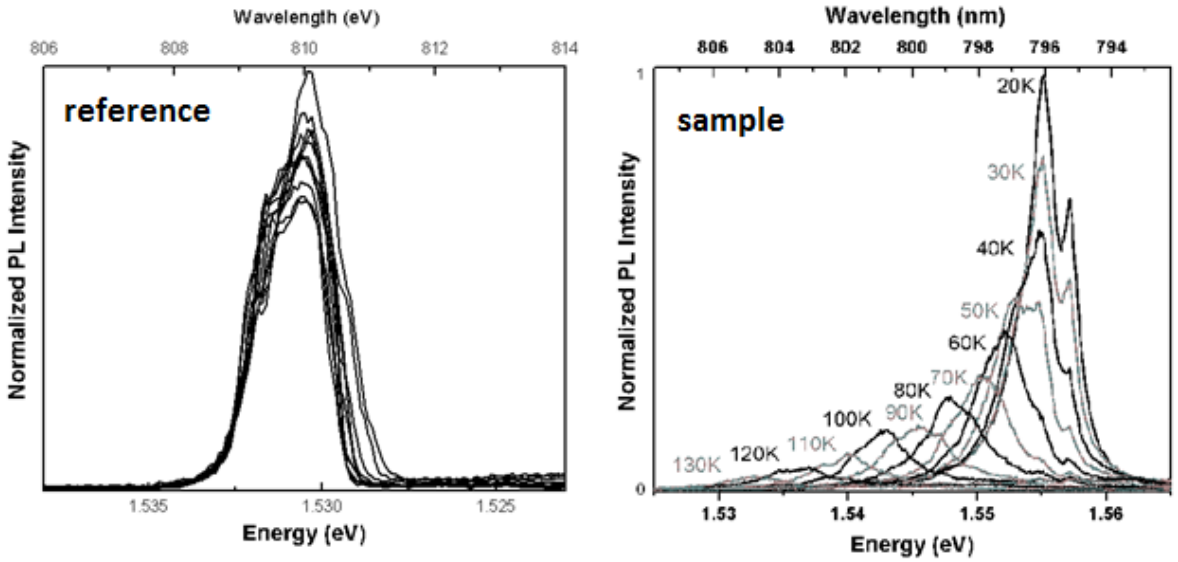

Figure 2.5.2 Temperature dependence of reference sample without gallium droplets (right) temperature dependence of sample with ICF (left).

The drift coefficient needs to be adjusted to allow for a 15 nm change in the average emission. The most logical and simple quantity to introduce for α is the drift velocity. Almost as an act of providence, the drift velocity is a function of the carrier mobility and electric field.

$$v_d = \mu \cdot F \tag{2.5.2}$$

where v_d is the drift velocity, μ is the carrier mobility, and F is the electric field. In the present

system the mobility is taken from Wiley [49], and is shown in figure 2.5.3.

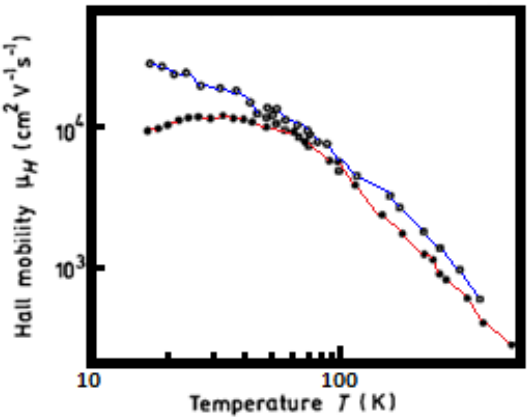

Figure 2.5.3 Carrier mobility in GaAs-AlGaAs quantum wells from reference [49].

The mobility is clearly temperature dependent and this is where the drift coefficient becomes a function of temperature (T). The spatial coordinate of α is trivially the distance from the gallium droplet the carrier is first excited at, thus putting the Ga droplet at the origin of the coordinate system. There is no time dependence on the drift velocity, thus v_d may be taken outside the time integral, and the time simply becomes the average lifetime of the carrier. Thus the drift towards the droplet becomes

$$\int_0^{\tau} v_d dt = \alpha_0 \cdot \mu_{\substack{e^- \\ h^+}} \cdot F_{ICF}^{\parallel} \cdot \tau \tag{2.5.3}$$

where α_0 is a scaling constant, μ is the mobility of electrons or holes, and $F_{ICF}^{\parallel}$ is the in plane component of the image charge electric field. Since v_d is independent of time the integral becomes the average lifetime of the particle, τ.

Figure 2.5.4 shows the PL spectra of the same gallium covered SQW at 15K and 130K. The energy shift and broadening are quite obvious. However the 130K spectra is not Gaussian, it appears more Poisson in nature; moreover it may be observed that every emission range in the 15K

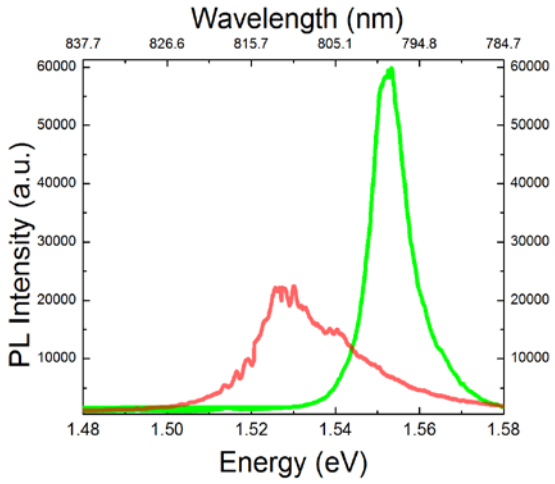

Figure 2.5.4 PL spectra for a gallium covered GaAs-AlGaAs SQW at 15K (green) and 130K (red)

spectrum is present in the 130K spectrum. Most of the emission energies in the 130K spectrum are not present in the 15K spectrum. These behaviors are also explained by the stochastic processes described in this section. At low temperature mobility is high and all carriers are able to drift into the higher potential regions. When mobility is decreased carriers will decay in regions of lower confinement potential. However the excitation area (laser spot size) excites carriers close and far from the droplet. The excitons created close to the droplet, will remain close to in (in the higher confinement potential) until they recombine, thus the high energy emission is still present in the 130K sample, although it is much lower. The other important aspect to consider is the surface area of the 2d quantum well, and how much of this surface is affected by the image charge potential. A rough estimate from the AFM images (see chapter 5 for sample details) puts this number at about 5 percent. Thus from any random excitation five percent of the excitons should experience an energy shift from the ICF potential, assuming that they do not drift towards the potential. Figure 2.5.5 shows the temperature evolution of the emission energy and FWHM for 2 nm, 5 nm, and 10 nm single GaAs-AlGaAs quantum wells.

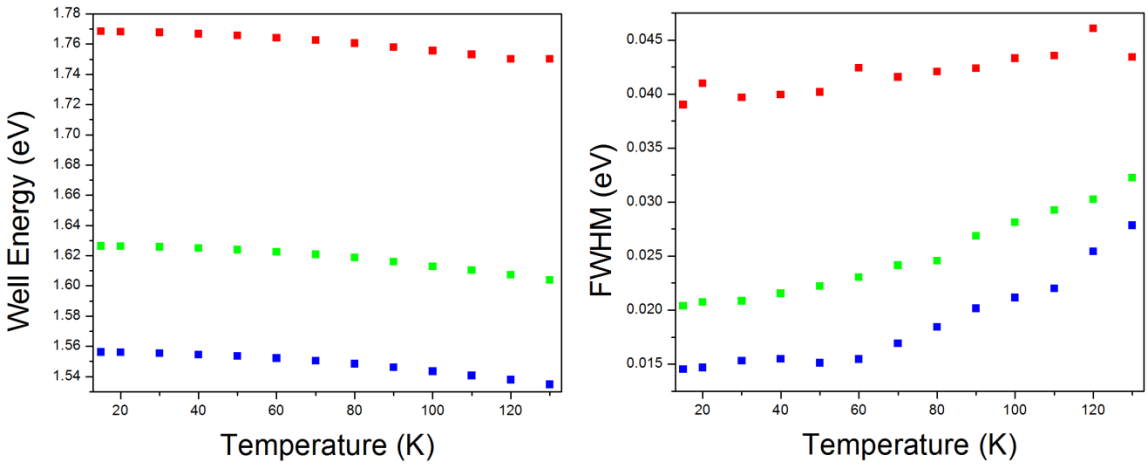

Figure 2.5.5 Temperature evolution of emission energy (right) and FWHM (left) for 2 nm (red), 5 nm (green), and 10 nm (blue) GaAs-AlGaAs SQWs.

The drift towards the gallium nano droplets has another effect: it increases the local carrier density of the excited excitons near the droplets. The increase in carrier concentration causes a decrease in carrier mobility [50], however the probability that a carrier will escape the ICF potential when close to the gallium droplet is negligible. Carrier concentration is directly related to the internal quantum efficiency in quantum well systems [51, 52]. This increase in efficiency seems to be as in reference [53]. However the power dependence of the gallium covered sample is not linear in nature. This is not a contradiction to the reference case, it is a result of the two dimensional stochastic drift towards the droplets. For each excitation power a different amount of carriers drifts towards the droplet creating regions of high carrier concentration, which is equivalent to increasing the excitation power for a small region of the reference sample.

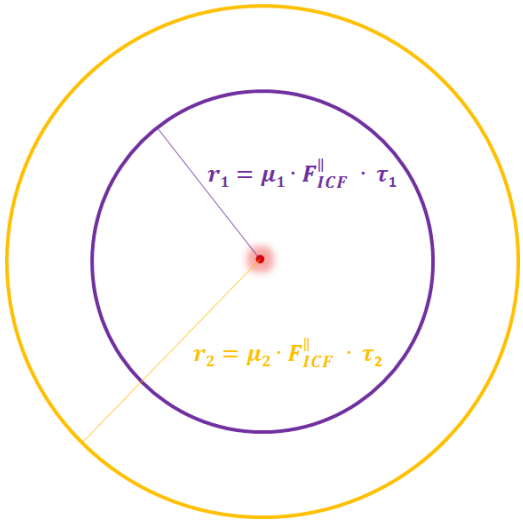

Figure 2.5.6 Schematic of Ga droplet and the radii of attraction (r1, r2) at different temperatures

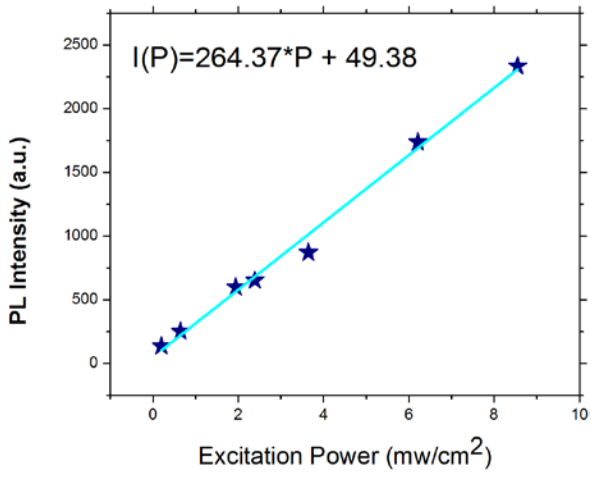

Figure 2.5.7 Best fit line of power dependence (carrier density) of a GaAs-AlGaAs SQW from [53].

The temperature intensity evolution of the gallium sample differs at a much faster rate than the reference sample (which is linear [53]). The intensity of the gallium covered sample changes as a square dependence. This is a function of the drift coefficient, and what percentage of carriers reach the potential of

the droplet. Figure 2.5.6 shows a gallium particle and radii of convergence for different temperature (different motilities and lifetimes). An average carrier drifts a distance $\mu F_{ICF}^{\|} \tau$ in the well. Thus carriers which are created a distance of $\mu F_{ICF}^{\|} \tau$ from the droplet will migrate into a region close to the droplet, increasing the carrier density around the droplet and decreasing the carrier density in all other regions of the wafer. In the simplified case where the intensity is a function of carrier concentration this causes a net increase in carrier concentration. Carrier density is most simply increasde by increasing the excitation power, thus creating more carriers in a uniform area. In the image charge attractive case the total amount of carriers remains constant, but the carriers are redistributed, thus creating areas of higher and lower concentration then uniform distribution in the quantum well. The function calculated for the power is shown as an inset in figure 2.5.7.

Taking the simple picture that each carrier in the image charge quantum well system is either close or far from the droplet it is possible to make an estimate of the change in intensity based on the best fit line in figure 2.5.7. An increase in the drift coefficient causes an increase in the carrier density around the metal, and a decrease of concentration everywhere else. The total amount of carriers is always constant and a function of excitation power. The drift coefficient is a direct function of the mobility, ICF, and lifetime, thus changing any one of these parameters leads to a change in expected intensity. To calculate the emission intensity of this binary system it is necessary to sum the products of the percentage of carriers in each region with the corresponding carrier density in that region. Based on the AFM images it is estimated that ten percent of the sample surface area is in the region near to the metal droplets. Thus if it is assumed that half the carriers in the sample are close to the droplets then their density increases to 5 times the original density and the density elsewhere decreases to 5/9 of the original density. See figure 2.5.8 for details. Thus the emission intensity from each region relative to the reference

(uniform density) is the percentage of carriers in that region time the expected emission intensity of carriers in that density state (best fit line of figure 2.5.7 (I(p)). Table 2.5.1 shows the expected intensities and ration of enhancement for the described system. The row highlighted grey represents the reference case where all the carriers are in the same density state. Thus it has no change in emission intensity.

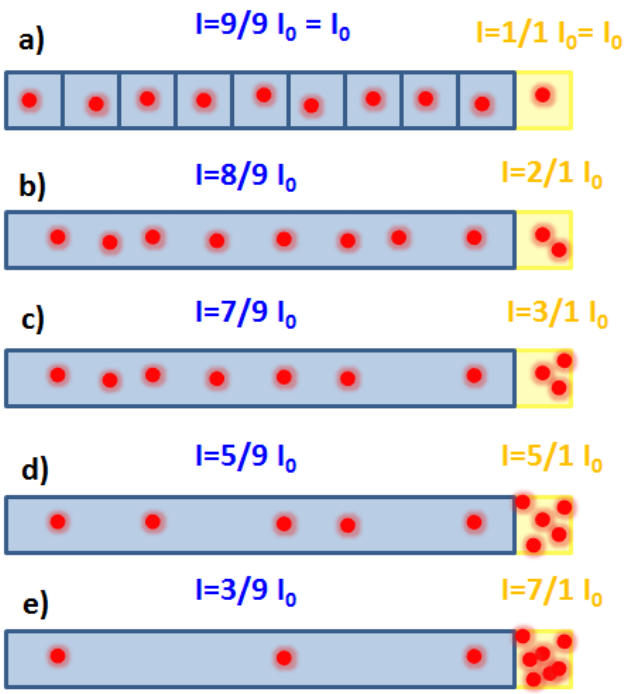

Figure 2.5.8 simplified schematic of random area where 90% of it is blue and 10% of it is yellow. Red dots represent particles and their density in the two regions is labeled as I for the 90% of the area (blue) and 10% of the area (yellow). a) is divided into ten equal parts to make the point that the ten particles correspond to equal areas.

Table 2.5.1 Theoretical prediction of change in intensity as the different percentages of carriers are aggregated in an area close to the nano droplet.

Percent Carriers not clustered around ICF	Percent Carriers clustered in ICF	Expected Intensity (a.u.)	I/I_{ref}
100	0	I_0*I(1)=*313.75*	1
95	5	I_0.*(.95*I(10/9)+.05 *I(1/2))= 335.05	1.07
90	10	I_0.*(.9*I(9/9)+.1 *I(1/1))= *313.75*	1
80	20	I_0*(.8*I(8/9)+.2*I(2/1))=*343.12*	1.09
70	30	I_0*(.7*I(7/9)+.3*I(3/1))=*431.25*	1.37
60	40	I_0*(.6*I(6/9)+.4*I(4/1))=*578.12*	1.84
50	50	I_0*(.5*I(5/9)+.5*I(5/1))=*783.74*	2.50
40	60	I_0*(.4*I(4/9)+.6*I(6/1))=*1048.11*	3.34
30	70	I_0*(.3*I(3/9)+.7*I(7/1))=*1371.23*	4.37
20	80	I_0*(.2*I(2/9)+.8* I(8/1))=*1753.10*	5.59
10	90	I_0*(.1*I(1/9)+.9* I(9/1))=*2193.71*	6.99
0	100	I_0*I(10)=*2693.08*	8.58

The row highlighted red is a pure theoretical idea where instead of attractive centers there exist repulsive centers; this also leads to an enhancement.The resulting intensity as a function of the drift coefficient is quadratic and corresponds to the intensity change in figure 2.5.2 for the Ga droplet plot. The change in intensity for the reference in figure 2.5.2 is linear as expected.

The trends of table2.5.1 stay true using continuous functions. Table 2.5.1 tabulates the results using the Heaviside step function

$$H(x) = \begin{cases} 0 & x < 0 \\ 1/2 & x = 0 \\ 1 & x > 0 \end{cases} \tag{2.5.4}$$

More specifically -H(x-a)/a where a is a constant distance from the droplet as in figure 2.5.6. It is trivial to see that integrating the product of this function with the power dependence function would reproduce the results of table 2.5.1. To illustrate the point two continuous candidate functions will be considered to replace the Heaviside step function. This adds nothing new to the theory. It is necessary that the candidate function converge on the interval [0, ∞) and be normalized. The two candidate functions are be an exponential decay and a product of a square and exponential. These functions are depicted in figure 2.5.9. It is important to notice that all the functions of figure

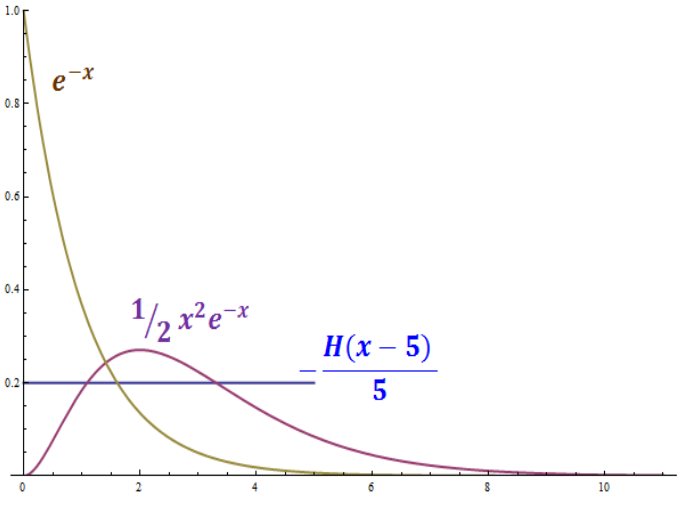

Figure 2.5.9 Candidate function for carrier density distribution

2.5.9 are normalized on the domain between zero and infinity. The normalization condition is trivially

$$\mathbb{1} = \int_0^\infty f(x)dx \tag{2.5.5}$$

Imposing the normalization condition is necessary to insure that the amount of carriers is always constant, only their local density is changed. Thus the expected intensity of all functions is where I is the best fit line to figure 2.5.7.

$$\mathbf{I} = \int_0^\infty \mathrm{I}(\mathrm{f}(\mathrm{x}))\ dx \tag{2.5.6}$$

Evaluating the bound integral, I, of the selected candidate functions results in the intensity increase from the in homogenous carrier distribution. The carrier concentration is varied continuously, preferable as a step function. It is also possible to reproduce this result using a Riemann sum.

2.6 Enhancement and Internal Quantum Efficiency

The internal quantum efficiency of a semiconductor emitter is defined as the ratio of photons coming into the system to the photons coming out of the system. Thus if every photon from the excitation beam was to be absorbed by the material, create an exciton, and recombine radiatively, the system would have one hundred percent quantum efficiency. The increase in recombination lifetime in the GaAs-AlGaAs system contradicts the observed increase in luminescence intensity. This discrepancy is resolved by the local increase in carrier concentration due to carrier drift in the in-plane direction of the well. However it is desirable that the observed enhancement be quantified in terms of the internal quantum efficiency.

The internal quantum efficiency (IQE) may be estimated as the ratio of the integrated PL

intensities of the same system at the lowest observed temperature and the highest observed temperature [30]. In this approximation it is assumed that the maximal quantum efficiency is reached at low temperature, and the low temperature intensity is a ratio of the best intensity. In the case of the presented GaAs-AlGaAs SQWs the temperature range was between 15 K and 130 K. The datum was stopped at 130 K due to concerns of the gallium droplets deforming due the continuous exposure to focused laser light. Thus the estimates for the IQE in this section are underestimates, but the observation that the IQE increases as a result of the presence of gallium droplets, and the image charge effect, remains valid. Figure 2.6.1 shows the integrated PL of the gallium covered and bare GaAs-AlGaAs 10 nm SQWs.

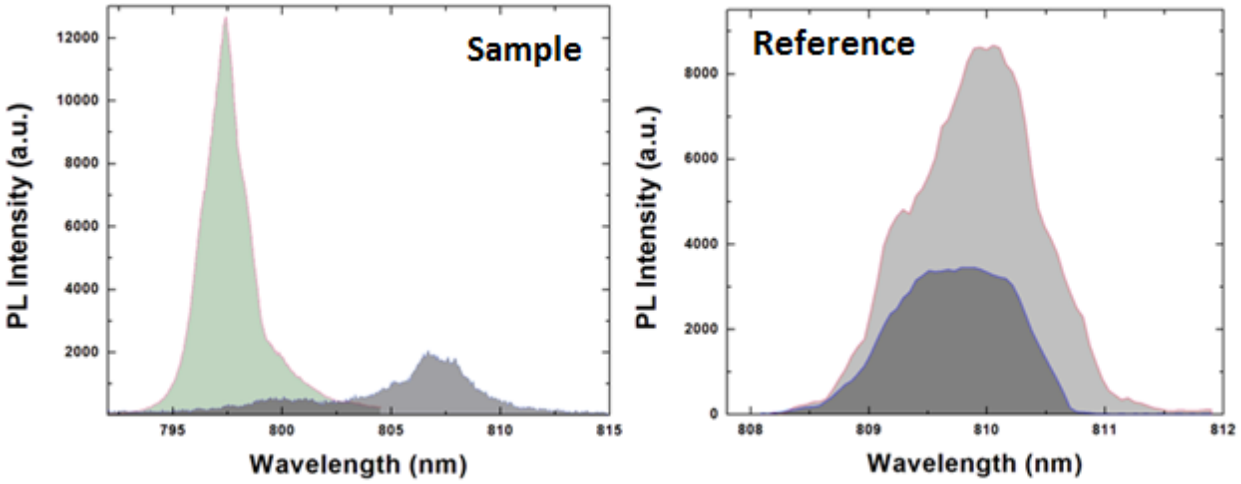

Figure 2.6.1 Integrated PL at 15 K (left) and 130 K (right) of Ga droplet sample (light shade, red outline) and reference sample (darker shade blue outline). The overlap in emission is shaded darkest, as the sum of the two.

Assuming that at 15K the internal efficiency is maximum, the internal quantum efficiency at 120K is calculated as $I_{120}K/I_{15K}\times100(\%)$ for the Ga droplet and reference samples as 56% and 45% respectively. The increase in quantum efficiency leads to PL enhancement. It should be noted that the rate of PL decrease with increasing temperature is greater for the droplet

sample, thus if the experiments were carried to higher temperatures the increase in IQE from the image charge effect would increase.

The above calculation is valid for all GaAs-AlGaAs SQWs in this study. The amount of light absorbed by each of the different size quantum wells is the same. Figure 2.6.2 presents the results from Masumoto et al [23] showing the relationship between well width and the absorption coefficient (α) in GaAs-AlGaAs wells. There is no data for 2 nm probably because of the difficulty of working with narrow wells. The fit and data points is an inverse function with a constant, k and the plotted in as a dashed line is f(l)=k/l. Thus the preceding fitted equation was solved and k was found to be to be 13.5. Thus α for 2 nm well is calculated using the best fit equation to be 6.75. The Beer-Lambert law is used to find the transmission of an ensemble of photons, it is in the form

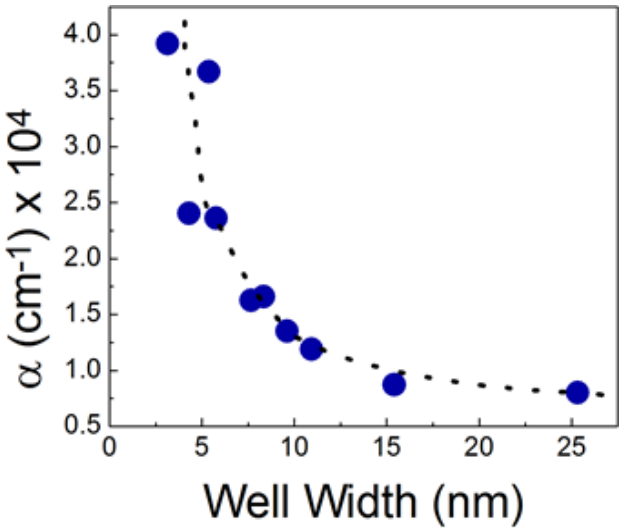

Figure 2.6.2 Absorption coefficient (α) versus well width for GaAs-AlGaAs wells from Masumoto et. al. [23].

$$T = \frac{I}{I_0} = e^{-\alpha l} \tag{2.6.1}$$

where T is the ratio of transmitted light, I is the intensity after the transmission, I0 is the initial intensity before the transmission, α is the absorption constant of the material the light is being transmitted through, and l is the length of the material. The percent of light absorbed is determined from the trivial conservation relation:

$$1 = T + A \tag{2.6.2}$$

where T is the transmission and A is the absorption. This of course assumes that there is no

reflection at the boundary of the materials. The assumption is ok in this case since we are only interested if GaAs quantum wells absorb different amounts of photons from the excitation pulse, and since they have the same GaAs-AlGaAs interface the reflection and that interface is identical for all wells, independent of their sizes. The calculated absorptions and transmissions for the SQWs are tabulated in table 2.6.1.

Table 2.6.1 Results of Beer-Lambert transmission calculations for GaAs-AlGaAs SWQs of lengths 10 nm, 5 nm, and 2nm.

	SQW 1	SQW 2	SQW 3
Well width l (nm)	10	5	2
α (10^{4} cm^{-1})	1.3	2.75	6.75
T=Exp[-α*l] *(2.6.1)*	0.987	0.986	0.986
% I_0 absorbed *(2.6.2)*	1.3	1.4	1.4

The results of table 2.6.1 show that the absorption of the laser excitation pulse by GaAs-AlGaAs quantum wells is independent of their length. Thus the same trends in the internal quantum efficiency are expected.

2.7 Chapter References

1. J. Holst, A. Kaschner, A. Hoffmann, P. Fischer, F. Bertram,T Riemann, J. Christen, K. Hiramatsu, T. Shibata, and N. Sawaki, Appl. Phys. Lett.,. 75, 11 (1999).
2. W. L. Barnes, Nature Materials, 3, 588 (2004).
3. A. Neogi, H. Morkoç, T. Kuroda, and A. Tackeuchi, Optics Letters, 30, 1, (2005).
4. A. Neogi, C. Lee, H. O. Everitt, T. Kuroda, A. Tackeuchi, and E. Yablonovitch, Phys. Rev. B 66, 153305 (2002).
5. K. Okomoto and Y. Kawakami, IEEE Journal of Selected Topics in Quantum Electronics 15, 4 (2009).
6. C.F. Lu, C. Liao, C. Chen, C. Hsieh, Y. Kiang, and C. C. Yang, Appl. Phys. Lett. 96, 261104 (2010).
7. Nagaraj,and A. Krokhin, Phys. Rev. B 81, 085426 (2010).

8. J. B. Khurgin, G. Sun, and R. A. Soref, J. Opt. Soc. Am. B. 24, 8, (2007).

9. L. V. Keldysh: Pis'ma Zh. Eksp. Teor. Fiz. 29 (1979) 716 [J. Exp. Theor. Phys. Lett. 29, 658 (1979).]

10. K. Tanaka, T. Takahashi, T. Kondo, K. Umeda, K. Ema, T. Umebayashi, K. Asai, K. Uchida, and N. Miura Jpn. J. Appl. Phys. 44, 8 (2005).

11. X. Hong, T. Ishihara, and A. V. Nurmikko: Phys. Rev. B 45, 6961 (1992).

12. E. A. Zhukov, Y. Masumotoa, E. A. Muljarovd and S. G. Romanov. Solid State Communications 112, 575 (1999).

13. Kai Chang and F. M. Peeters, J. App. Phys; 88, 5246, (2000).

14. A. Nazimov, E. Cohen, Arza Ron, B.M. Ashkinadze, and E. Linder, Journal of Luminescence 85, 301 (2000).

15. D. Lepage and J. J. Dubowski, Appl. Phys. Lett. 91, 163106 (2007)

16. Z. Gong, Z. C. Niu, S. S. Huang, Z. D. Fang, B. Q. Sun, and J. B. Xia, Appl. Phys. Lett. 87, 093116 (2005).

17. Zh. M. Wang, K. Holmes, J. L. Shultz, and G. J. Salamo, Phys. Status Solidi A 202, R85 (2005).

18. J. Planelles and J. I. Climente, Eur. Phys. J. B 48, 65 (2005).

19. B. L. Liang, Zh. M. Wang, J. H. Lee, K. Sablon, Yu. I. Mazur, and G. J. Salamo, Appl. Phys. Lett. 89, 043133 (2006).

20. J. H. Lee, Zh. M. Wang, Z. Y. AbuWaar, N. W. Strom, and G. J. Salamo, Nanotechnology 17, 3973 (2006).

21. R. Pomraenke, C. Lienau, Y. Mazur,Z. Wang, B. Liang, G. Tarasov, and G. Salamo Phys. Rev. B 77, 075314 (2008).

22. T. Mano, T. Kuroda, S. Sanguinetti, T. Ochiai, T. Tateno, J. Kim, T. Noda, M. Kawabe, K. Sakoda, G. Kido, and N. Koguchi, Nano Lett. 5, 425 (2005).

23. Y. Masumoto, M. Matsuurab, S. Taruchac, and H, Okamoto, Surface Science 170, 635 (1986).

24. D. A. B. Miller, D. S. Chemla, and T. C. Damen ,A. C. Gossard and W. Wiegmann, T. H. Wood and C. A. Burrus, Phys. Rev Lett., 53, 22, (1984).

25. G. Bastard, E. E. Mendez, L. L. Chang, and L. Esaki, Phys. Rev. B 28, 6 (1983).

26. T. Someya, H. Akiyama, and H. Sakaki, Phys. Rev. Lett 74, 18 (1995).

27. YJ. Chen, B. Elman and Emil S. Koteles, Solid State Communications, 72, 1, (1989).

28. N.G. Semaltiano, Journal of Physics and Chemistry of Solids, 63, 273 (2002).

29. J. W. Orton, P. Dawson, D. E. Lacklison, T. S. Cheng, and C.Foxon, Semiconductor Science and Technology, 9, 9 (1994).

30. SW. Kim, S. Fujita, and Sh. Fujita, Appl. Phys. Lett, 86, 153119 (2005).

31. Y. D. Jho, J. S. Yahng, E. Oh, and D. S. Kim, Appl. Phys. Lett 79, 8, (2001)

32. P. C. Wu, T.-H. Kim, A. S. Brown, M. Losurdo, G. Bruno, and H. O. Everitt, Appl. Phys. Lett. 90, 103119 (2007)

33. D. Ahn and S.L. Chuang, Phys. Rev. B, 34, 12 (1986)

34. S.F. Chichibu, A.C. Abare, M.P. Mack, M.S. Minsky, T. Deguchi, D. Cohen, P. Kozodoy, S.B. Fleischer, S. Keller, J.S. Speck, J.E. Bowers, E. Hu, U.K. Mishra, L.A. Coldren, S.P. DenBaars, K. Wada, T. Sota, and S. Nakamura, Mat. Sci. and Eng., B59 298 (1999)

35. J. Lin, A. Mohammadizia, A. Neogi,H. Morkoc, M. Ohtsu, Appl. Phys. Lett. 97, 221104 (2010)

36. K. Okamoto, and Y. Kawakami, Phys. Stat. Sol. C, 7, 2582 (2010)

37. P.M. Tu, C.Y. Chang, S.C. Huang, C.H. Chiu, J. .R. Chang, W.T. Chang, D.S. Wuu, H.W. Zan, C.C. Lin, H.C. Kuo, C.P. Hsu Appl. Phys. Lett. 98, 211107 (2011)

38. F.T. Vasko, A.V . Kuznestow. Electronic States and Optical Transitions in Semiconductor Heterostructures, Springer-Verlag New York Inc. (1999)

39. M.V. Durnev, A. V. Omelchenko, E. V. Yakovlev, I. Y. Evstratov, S. Y. Karpov, Phys. Stat. Sol doi: 10.1002/pssa.201127278 (2011)

40. J. Sean J. I.L. Yoon, Jpn. J. Appl. Phys. 40 3124 (2001)

41. S.F. Chichibu, A.C. Abare, M.P. Mack, M.S. Minsky, T. Deguchi, D. Cohen, P. Kozodoy, S.B. Fleischer, S. Keller, J.S. Speck, J.E. Bowers, E. Hu, U.K. Mishra, L.A. Coldren, S.P. DenBaars, K. Wada, T. Sota, and S. Nakamura, Mat. Sci. and Eng., B59 298 (1999)

42. C. Berthod, N. Binggeli, A. Baldereschi, Phys. Rev. B 68, 085323 (2003)

43. L. Geng, B. Magyari-Kope,and Y. Nishi, IEEE Electron Device Letters, 30, 963 (2009).

44. P. R. Vemuri, Masters Thesis, University of North Texas (2005).

45. U.M.E. Christmas, A.D. Andreev, D.A. Faux, Journal of Applied Physics 98, 073522 (2005)

46. K. Okamoto, I. Niki, A. Shvartser, Y. Narukawa, T. Mukai, AND A. Sherer, Nat. Mat. lett., 3, 601 (2004)

47. D. Arbel, N. Berkovitch, A. Nevet, A. Peer, S. Co-hen, D. Ritter,and M. Orenstein, Optics Express, 12, 10 (2011)

48. C.Y. Chen, Y.C Lu, D.M Yeh, and C.C. Yanga Appl. Phys. Lett. 90, 183114 (2007)

49. J. D. Wiley, Semiconductor and Semimetals 10 91 (1975)

50. Y. Shiraki, T. Mishima, and M. Morioka, J. of Crystal Growth 81, 164 (1987)

51. J. Lee, Y. Tak, J. Kim, H. Hong, S. Chae, B. Min, H. Jeong, J. Yoo, J. Kim, Y. Park, J. of Crystal Growth, 315, 263 (2011)

52. C.H. Wang, C.C. Ke, C.H. Chiu, J.C. Li, H.C. Kuo, T.C. Lu, S.C. Wanga, J. of Crystal Growth, 315, 242 (2011)

53. N.G. Semaltianos, Journal of Physics and Chemistry of Solids, 63, 273 (2002)

54. J. R. Kuklinski and S. Mukamel, J. of Lumin. 53, 97 (1992)

55. L. Z. Peredo, A. G. Cervants, Z. R. Alvarez, M. L. Lopez, A. G. Vazquez, V. G. Garcia, Microelectronics Journal 34 521 (2003)

56. G.V. Ramanathan, Lecture Notes, © 2008.

57. A.P. Ghosh, Lecture Notes “Introduction to Diffusion Processes,” Iowa State University © 2010

58. G. Chirico, C. Fumagalli, G. Baldini, J. Phys. Chem. B. 106, 2508, (2002)

59. A. H. MacDonald, H. C. A. Oji, K. L. Liu, Phys. Rev. B 34, 2681 (1986)

CHAPTER 3

IMAGE CHARGE EFFECTS AND PLASMONICS EFFECTS

The image charge effect is a way to alter carrier dynamics and thus optical properties in semiconductors. Plasmonics is another phenomenon which alters carrier dynamics in semiconductor systems. Plasmonics is an electro-dynamics phenomenon characterized by an increase in the radiative rate of a semiconductor. Carriers which couple to surface plasmon polaraitons recombine quicker (decrease in lifetime) causing a higher emission intensity. For plasmonics to be observable in a system the plasmon frequency, determined the dielectric function mismatch between a metal and semiconductor/insulator, must be close to the semiconductor emission energy. In contrast the image charge effect is an electrostatic phenomenon. It is most pronounced for metals; however it can also arise at junctions of two dielectrics with different dielectric constants. The larger the difference of the dielectric constants the more pronounced the image charge effect will be for that system.

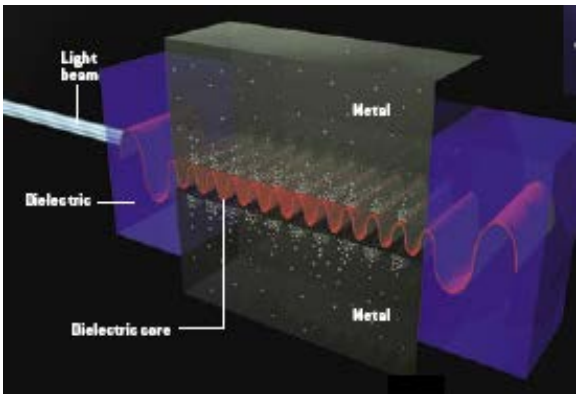

Figure 3.1 Simulation of plasmonically coupled system

3.1 Differences between Image Charges and Plasmonics

Plasmonic is a resonant phenomenon, meaning that the plasmon frequency energy ($\hbar\omega_p$) must match the emission energy. This limits the possible metals which may be used per emission energy, furthermore the dielectric on which the metal is deposited on also contributes

to the plasmon frequency and thus energy.

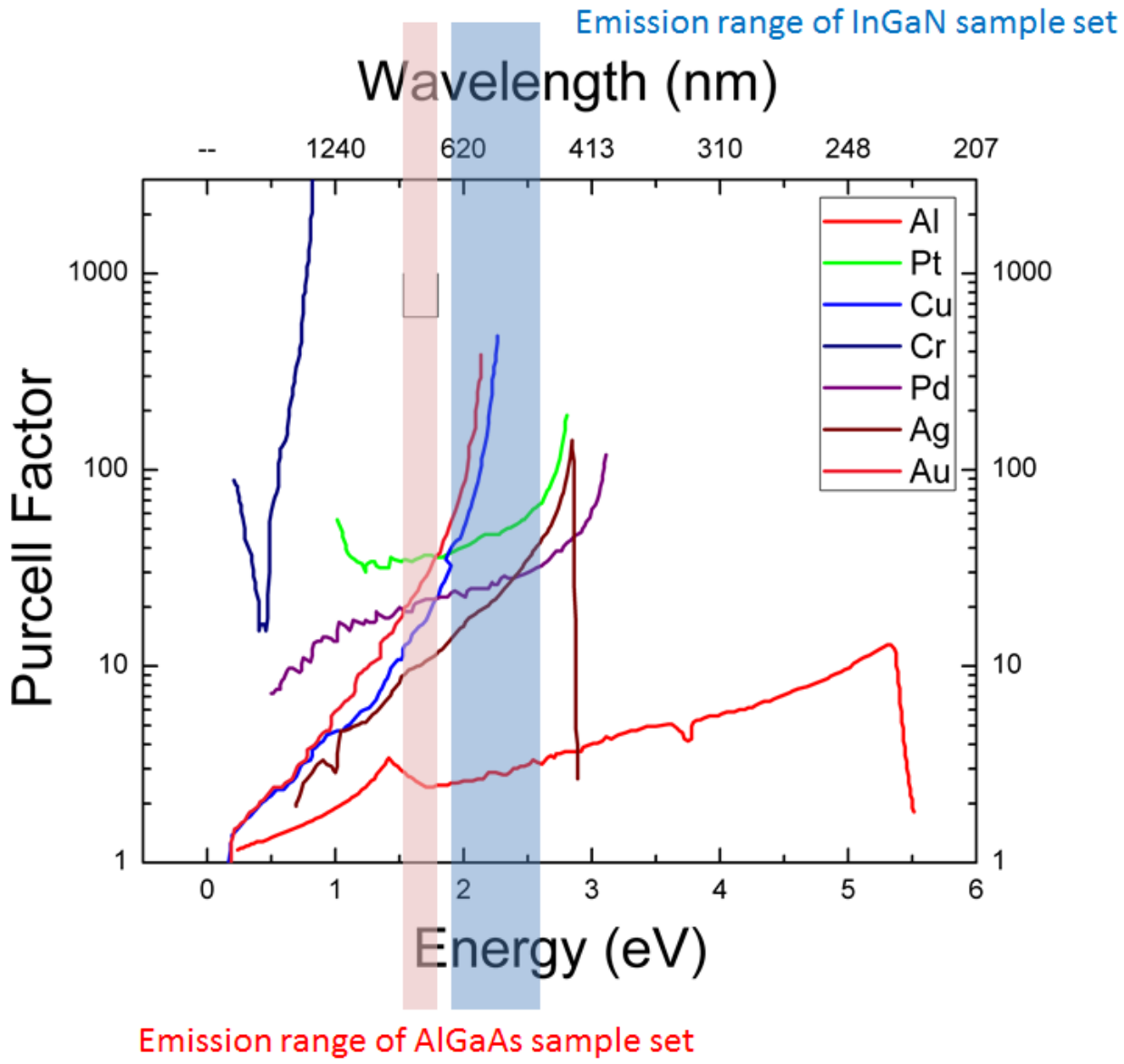

Figure 3.1.1 Plasmonic enhancement from various metals

Figure 3.1 shows different energy (wavelength) regions of possible plasmon coupling from certain metals to emitters and how much enhancement may be expected from plasmonics. Regions of emission from the samples of the current work are highlighted; red for the GaAs-AlGaAs QWs and blue for the GaN-InGaN quantum wells. The shaded regions include the

maximum and minimum energy as well as several energies in between. They do not imply that the sample can have any energy in the shaded region. The enhancement or Purcell factor ($F_p(\omega)$) is calculated as:

$$F_p(\omega) = \frac{\Gamma_p(\omega) + \Gamma_0(\omega) + \Gamma_{nr}(\omega)}{\Gamma_0(\omega) + \Gamma_{nr}(\omega)} \approx 1 + \frac{\Gamma_p(\omega)}{\Gamma_0(\omega)} \quad (3.1.1)$$

where Γ_{nr} is the none-radiative recombination rate, Γ_p is the plasmon induced recombination rate, Γ_0 is the recombination rate in the absence of plasmons, and ω is the frequency. Thus a Purcell factor of one means no enhancement. It is important to note that the Purcell enhancement is only valid when the resonance condition is met, for ω_p faraway F_p will always be 1. Equation 3.1.1 also does not take into account scattering or reflection from the metal surface and it assumed that the same excitation power is delivered to the plasmonically coupled and uncoupled systems.

The image charge effect however relies only on the one property which all metals have in common: the electric field inside a metal is zero. The free surface electrons on the surface rearrange in such a way that the field inside remains zero, but the field outside the metal need not be zero. Interaction with this field is the necessity for the image charge to be present (even if in such a small scale that it is not observable). Any enhancement from this effect is most likely caused by the localized increase in carrier concentration and is thus analogues to increasing excitation power, or number of excited carriers. Thus the image charge interaction and plasmonic interaction result from different properties of the metal, which are not mutually exclusive. Table 3.1.1 lists some of the differences between the image charge effect and plasmonics.

Table 3.1.1 Contrasts of image charge effects and plasmon effects

Plasmonic interactions	Image charge interactions
Resonant: occurs at frequencies $\omega < \omega_p$	Is frequency independent
Independent of excitation power	Enhancement ratio saturates with excitation power
Decrease carrier lifetime	Increase carrier lifetime
Dissipates exponentially with distance	Dissipates as a polynomial (inverse square law) with distance
Does not alter quantum confined potential in any significant way.	Alters quantum confined potential
Increases density of states	Increases local carrier concentration
Electrodynamic in nature	Electrostatic in nature

Keeping the contrasts of table 3.1.1 in mind is necessary to identify a system with both plasmonic and image charge effects. Although both interactions can lead to an increase in radiative efficiency they do it in fundamentally different ways. This allows for isolation of one of the effects and for the two to coexist to together.

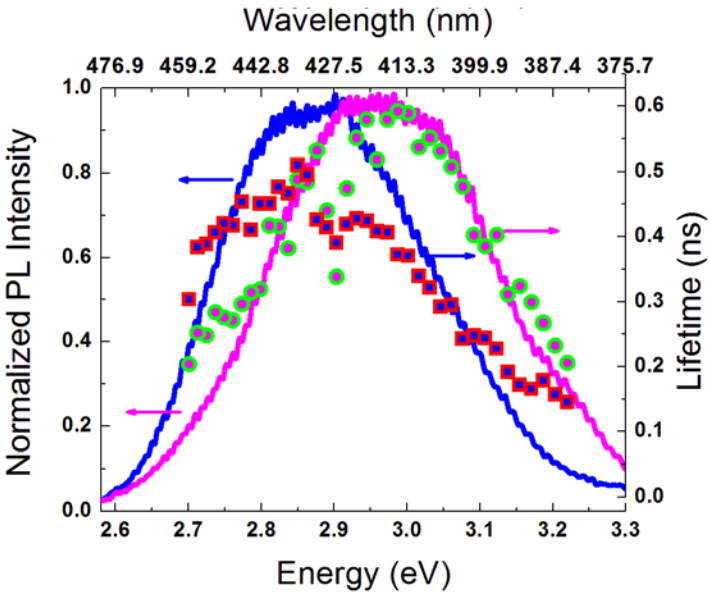

Figure 3.2.1 PL spectra of bare InGaN SQW (magenta) and InGaN SQW with Ga droplets (blue). Lifetimes are shown for the gallium covered well (blue square) and bare sample (magenta circle).

3.2 Case Study in GaN-InGaN

The competition between the image charge effect and plasmonics is investigated with time resolved photoluminescence. The technique can easily and reliably detect the emission lifetimes as a function of emission wavelength or energy ($\hbar\omega = h\nu = hc/\lambda$). In fact the decrease in carrier lifetime is often used to prove the existence of plasmonic interaction in a system.

Figure 3.2.1 shows the PL spectra (lines) with overlaid lifetimes for the corresponding energies (scatter plot). The gallium droplet covered SQW spectrum is depicted as the blue line and has lower emission energy then the reference sample (magenta). The corresponding lifetimes for the gallium sample are the blue squares with red boarders and the bare sample has lifetimes represented with magenta circles with green borders. The interesting behavior seen from these lifetimes is that they intersect at about ħω = 2.85 eV, the gallium sample has a longer lifetime in the low energy region then the reference and a shorter lifetime in the high energy region. This intersection in lifetimes is inconstant with either the plasmonics picture or the image charge picture. However, this data shows a clear case of competition between the two effects, with plasmonics dominating in the low energy region and the image charge effect dominating at higher energies. Of course the image charge effect is independent of emission energy.

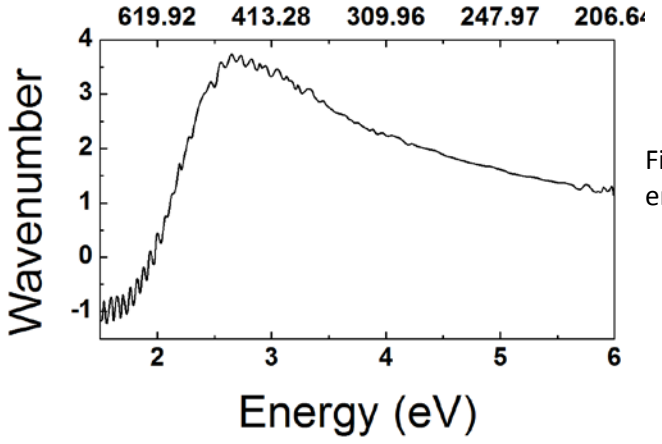

Figure 3.2.2 Dispersion relation for plasmon energy for coupled gallium droplet system

At the energy point where the sample and reference lifetimes are equal the two effects, plasmonics and image charge effect, appear to cancel each other out. This behavior shows a clear competition between the two effects, and that either affect may be dominant. This happens at ~2.85 eV, roughly at the maxima of the dispersion relation in figure 3.2.2 [2]. It is hypothesized that the image charge interaction is present in the entire emission region, and the

plasmonic interaction is present only at the surface plasmon resonance region. The increase in plasmon energy of dense gallium droplets arises from the resonance conditions and size distributions and is described else ware [2].

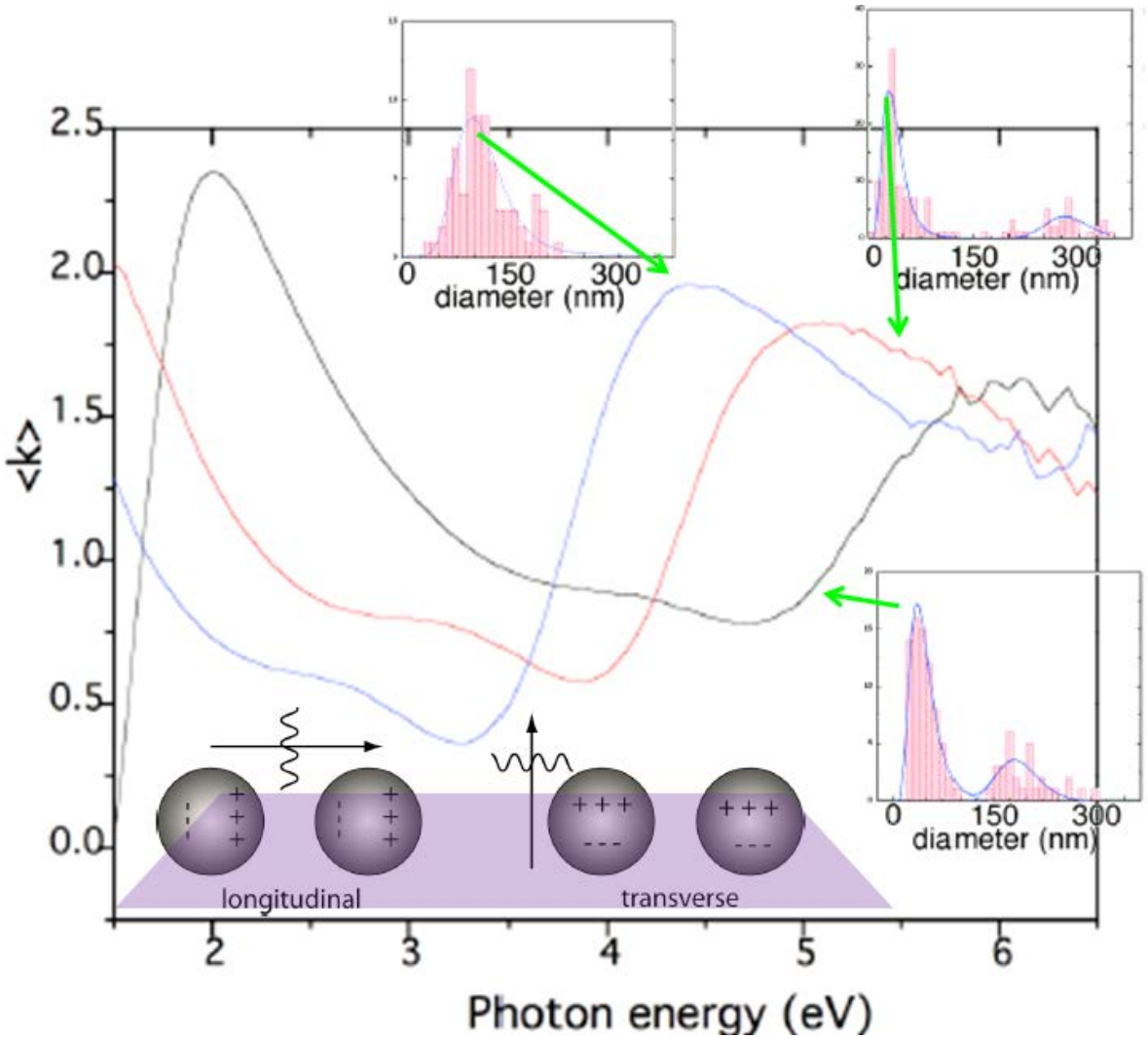

Figure 3.2.3 <k> dependence on photon energy for coupled gallium droplets of different sizes. the three histograms show the size particle size distributions of the corresponding curves. The inset on the bottom illustrates the longitudinal and transverse modes sustained by the droplets

Figure 3.2.3 shows the data from Pae Wu [15] detailing the size dependence of the gallium droplets on the plasmon energy. For smaller average droplet diameter distribution greater plasmon energy is observed. The inset, also from reference [15], shows the schematic

for longitudinal and transverse plasmon coupling on spherical particles. The higher energy plasmons are the transverse modes while the lower energy modes are the longitudinal modes.

Figure 3.2.4 show the entire photoluminescence spectra for the gallium droplet covered and bare InGaN samples. The high energy emission at 3.44 eV is from bulk GaN in the sample. The emission at 3 eV is the emission from the quantum well, and the emission peak at ~1.8 eV originates from defect sites from the growth.

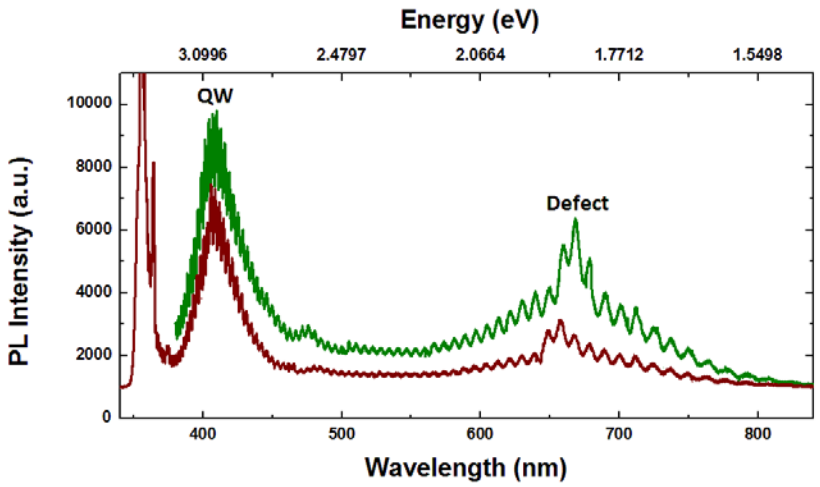

Figure 3.2.4 PL spectra of Ga droplet covered InGaN SQW (red) and bare SQW (green)

The steady state spectra of the two samples look quite similar and not out of the ordinary. Lifetime measurements for these samples were measured using astage scanning fluorescence lifetime microscopy and are presented in figure 3.2.5. Each square in Fig. 3.2.5 shows the representative 30 µm by 30 µm image area (300 pixels by 300 pixels). Color brightness correspond to the observed intensity and actual color represents average fluorescence lifetimes measure over the each individual pixel. Effectively the lifetime was measured at 90,000 unique locations on the sample where each pixel corresponds to a stage translation of 100 nm. However the real size of observed spots is diffraction limited and is close

to 250 nm for short wavelength and slightly above 300 nm for long wavelength observation.

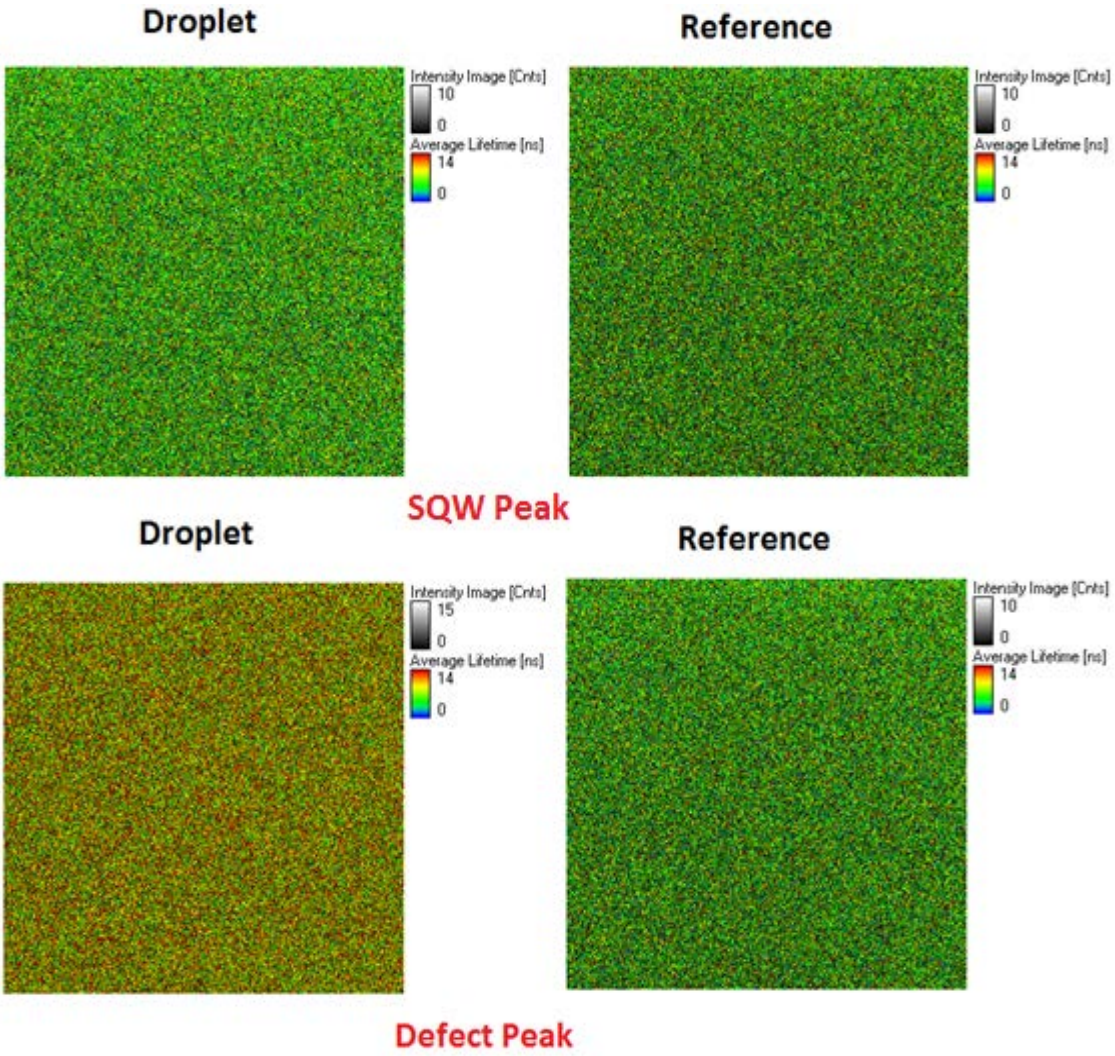

Figure 3.2.5 FLIM measurements at 450 nm (top) and 650 nm (bottom) for droplet (left) and reference (right) samples

The quantum well emission was observed through a 440 nm ± 20 nm band pass filter. The defect peak was observed through a 650 nm long wavelength pass filter. The top two images show the lifetimes for the quantum well while the bottom two show the lifetimes for the defect peak. The left side images are for the sample with the gallium droplets and the right images are for the reference sample. The lifetimes of the two QW peaks are quite similar, the gallium covered sample lifetime is perhaps a bit longer but no significant conclusion may be reached

due to the noise. However the lifetime difference in the defect peak is striking with gallium droplet sample showing a great increase in the average lifetime. How can this large difference in lifetimes be explained for the defect states while the change in lifetime for the quantum confined emission peak is negligible, especially since the data is taken from the same wafer. The answer lies in the fact that the plasmonic interaction has a small resonant range where it is affective, and the image charge effect is equally applicable to all emission wavelengths in the sample. Thus at the emission energy of the quantum well competition between plasmonics and image charges is observed, in this particular case leading to negligible lifetime change. The defect peak however is far off plasmonic resonance and thus only the image charge effect manifests. This result is especially interesting since the same metal is being used for plasmonics and image charge and one of the emissions is coupled via plasmons, one is not, and both are effected by the image charge effect. An interesting future experiment would be to use the same InGaN QW and deposit a metal on it such that it would plasmonically couple to the defect emission and not the quantum well emission.

3.3 Case Study in GaAs-AlGaAs

Plasmonic coupling decreases carrier lifetime. The Itō distribution presented in section 2.3 is directly dependent on lifetime, since the drift is

$$\alpha = \int_0^{\tau} v_d dt = \alpha_o \cdot \mu \cdot F_{ICF}^{\parallel} \cdot \tau_{avg} \tag{3.3.1}$$

Thus it is predicted that the amount of carriers which recombines close to the metal droplets in the presented GaAs-AlGaAs systems diminishes as lifetime diminishes. Thus, as with reducing

the carrier mobility or the intensity of the ICF, decreasing the average lifetime is also expected to decrease the center emission energy shift.

Two GaAs-AlGaAs semiconductor/metals hybrid systems were created for this study. The QW systems with gallium droplets on the surface were used, and metal colloids were then deposited on their surfaces. Thus these samples have two metals on top, one which couples via resonant plasmons (Au or Ag), and one which does not (Ga). First a 1.5 nm SQW was treated with a low concentration silver colloidal solution of average size 30 nm nano particles. The aqueous solution of colloids was spread over a part of the sample wafer and left to dry until all water evaporated. The resulting wafer was half covered with silver particles which give that half a yellowish color (Fig. 2.2). Second, a 10 nm SQW was treated with a low concentration colloidal gold solution. Half of the wafer was covered with 50 nm gold nano particles and became reddish in color. Both these systems are known to couple via plasmons [3, 4, 5, 6]. It is important to note that the emission of the 10 nm and 1.5 nm QWs is almost 0.3 eV apart, thus using different metals for plasmonic coupling is acceptable. Furthermore using materials with different plasmonic resonances eliminates the possibility that the observed differences do no originate exclusively from plasmonics. Both quantum wells have a five nm cap layer. In both these systems the emission energy shift was diminished compared to the sample with only gallium but there was still a blue shift compared to the sample without any metal. The PL from the 1.5 nm well

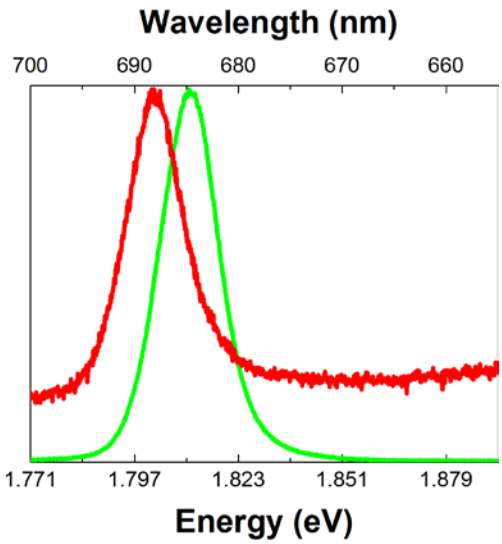

Figure 3.3.1 1.5 nm GaAs-AlGaAs SQWs covered with gallium droplets (green) and with added silver colloids (red)

covered with silver is presented in figure 3.3.1 and the PL from the 10 nm well covered with gold is shown in figure 3.3.2. Furthermore both dual metal samples exhibit the same temperature dependent behavior as the gallium only samples presented in section 2. Since the samples were excited through the deposited metals and their emission was again scattered by the same layer the intensity decreased. This is due to the fact that the samples could not be back excited, and has nothing to do with intensity change due to plasmonics.

This energy shift is expected using the Itō formalism and is observed experimentally. The above experiments were done using a steady state laser to illustrate that this is the expected behavior when carrier creation/annihilation is at equilibrium. Thus all three factors determining the drift, mobility, ICF intensity, and lifetime, have been isolated and experimentally observed to have the expected results. Another important observation from figure 3.3.2 is the change in the peak width. This is expected as the probability of carriers recombining under the Ga droplets is none zero while most of the recombination occur elsewhere.

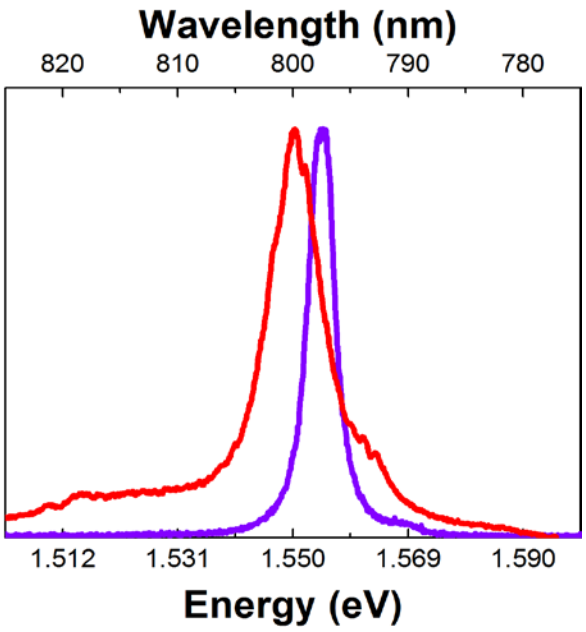

Figure 3.3.2 10 nm GaAs-AlGaAs SQWs covered with gallium droplets (green) and with added gold colloids (red)

Coupling of the excitons in the quantum well to the plasmons on the gold spheres is confirmed through TRPL measurements. The part of the QW covered with Au colloids has a faster recombination rate, Fig. 3.3.3b then the part with only the Ga droplets, Fig. 3.3.3a.

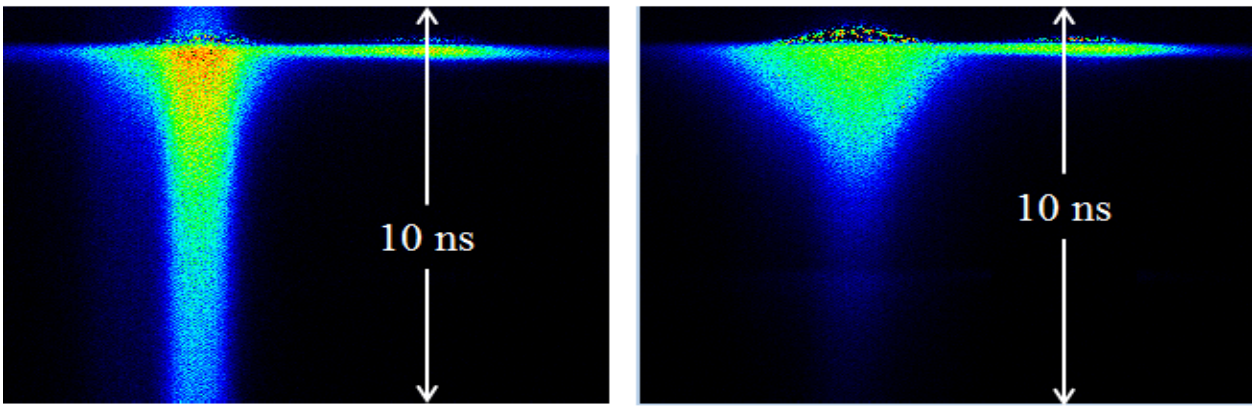

Figure 3.3.3 Streak camera image showing the difference in lifetime between the image charge only Ga-AlGaAs sQW with gallium droplets (a) and GaAs-AlGaAs sQW covered with both gallium droplets and gold spherical nanoparticles

The TRPL measurements also confirm the increase in FWHM when both plasmonic and image charge effects are present. The addition of the gold particles is confirmed using APL shown in figure 3.3.4.

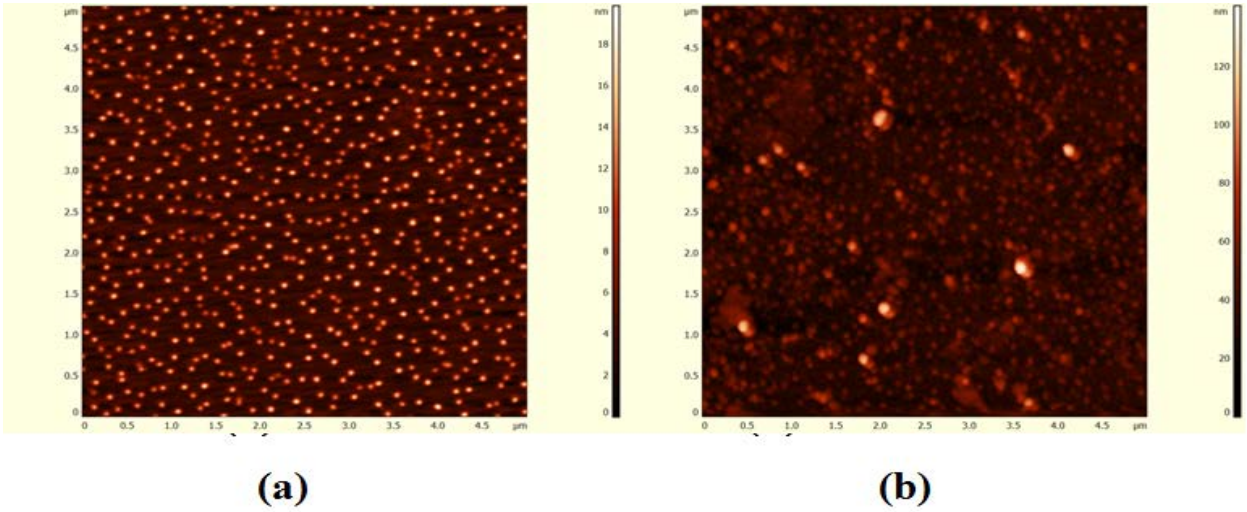

Figure 3.3.4 AFM images of Ga droplets (a) and Ga droplets and Au spheres (b)

Figure 3.3.4a shows only the gallium droplets, while figure 3.3.4b shows the gallium and gold. The gallium appears darker in figure 3.3.3b because the extreams of the color scale are the same and the gold spheres are much talker then the gallium.

3.4 Chapter References

1. A.K. Singh, K.G. Gryczynski, F.D. McDaniel, S. Y. Park, M. Kim, A. Neogi, Applied Physics Express 3, 102201 (2010) .
2. P. C. Wu, T.-H. Kim, A. S. Brown, M. Losurdo, G. Bruno, and H. O. Everitt, Appl. Phys. Lett. 90, 103119 (2007)
3. N.E. Hecker, R.A Hopfel, N. Sawaki, T. Maier, G. Strasser, Appl. Phys. Lett. 75, 11 (1999)
4. D. Lepage, J.J. Dubowski, Appl. Phys. Lett. 91, 163106 (2007)
5. K. Nakayama, K. Tanabe, H.A. Atwater 93, 121904 (2008)
6. D.A. Evans, M. Alonso, R. Cimino, K. Horn, Phys. Rev. Lett. 70, 3483 (1993)
7. K. Uno, S. Susumu, A. Sasaki, J. Appl. Phys. 77, 9 (1995)
8. W. Rechberger, A. Hohenau, A. Leitner, J.R. Krenn, B. Lamprecht, F.R. Aussenegg, Optics Comm. 220, 137 (2003)
9. A. Neogi, C.W. Loo, H.O. Everitt, T. Kuroda, A. TackeuchiE. Yablonvitch, Phys. Rev. B 66 153305 (2002)
10. E.A. Shaner, M. Lee, M.C. Wanke, A.D. Grine, J.L, Reno, S.J. Allen, Appl. Phys. Lett. 87 193507 (2005)
11. T. Demel, D. Heitmann, P. Grambow, K. Ploog, Phys. Rev. Lett. 66 20 (1991)
12. K. Okamoto, I. Niki, A. Scherer, Y. Narukawa, T. Mukai, Y. Kawakami, Appl. Phys. Lett. 87 071102 (2005)
13. N. Okisu, Y. Sambe, T. Kobayashi, App. Phys. Lett. 48, 776 (1986)
14. M. Giltrow, A. Kozorezov, M. Sahraoui-Tahar, J. K. Wigmore, J. H. Davies, C. R. Stanley, B. Vogel, C. D. W. Wilkinson, Phys. Rev. Lett. 75 1827 (1995)
15. Pae Wu, Plasmonic Gallium Nanoparticles – Attributes and Applications, Department of Electrical and Computer Engineering, Duke University (2009)

CHAPTER 4

ON THE INTERACTION OF THE IMAGE CHARGE EFFECT AND PHONONS

All semiconductors and metals are comprised of crystal lattices. Solids which do not have a crystal lattice are called amorphous and are not discussed in this chapter. The lattice is a distribution of atomic nuclei which remain at a certain distance and orientation relative to each other and are bound together by electromagnetic forces. These lattices are periodic arrays of the same basic structure, called a unit cell. Each nucleus in the lattice is called a lattice point. These lattices vary amongst each other in ways such as their geometric arrangement of lattice points (wurtzite, rock salt, cubic, etc.) and the separation between lattice points. These lattice points, however, are not stationary in relation to each other and the nuclei oscillate about the mathematical dot which represents their average position within the lattice. These oscillations have energy, and a quantum of such a vibration is called a phonon. This chapter deals with phonons in image charge systems.

The materials in this work are made of different types of lattices. GaN and InGaN have a wurtzite crytal structure depicted in figure 4.1. Wurtzite crystals lattice are not centro symmetric which often leads to the presence of inbuilt piezoelectric fields as in GaN-InGaN systems as described in chapter 2.

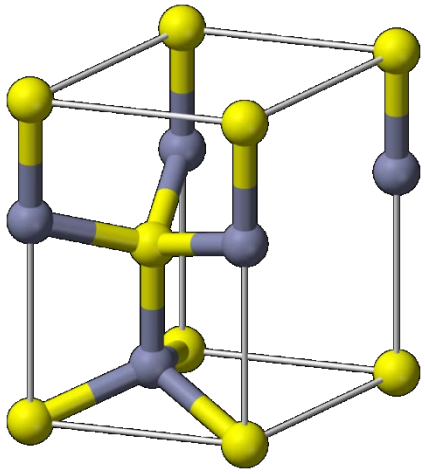

Figure 4.1 Wurtzite unit cell (GaN and InGaN). *Use of image complies with BSDU license.*

Gallium arsenide and aluminum gallium arsenide have a zinc blend lattice structure depicted in figure 4.2. This lattice structure is from the cubic structure and is arranged as a

diamond cubic, except that it has two nuclear species in the lattice. Each nucleus has four nearest neighbors, of a different species. This structure is essentially two face centered cubic lattices which are overlaid within each other with an offset of lattice points.

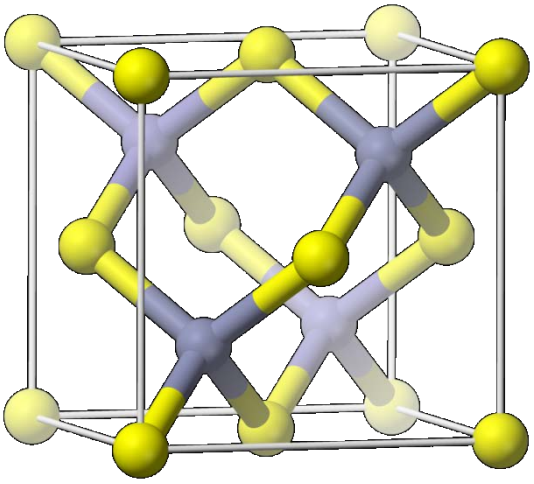

Figure 4.2 Zinc blend unit cell (GaAs and AlGaAs). *Use of image complies with BSDU license.*

The noble metals used in this work, gold and silver, both have a face centered cubic lattice unit cell. This unit cell is shown in figure 4.3. This lattice structure is common for metals.

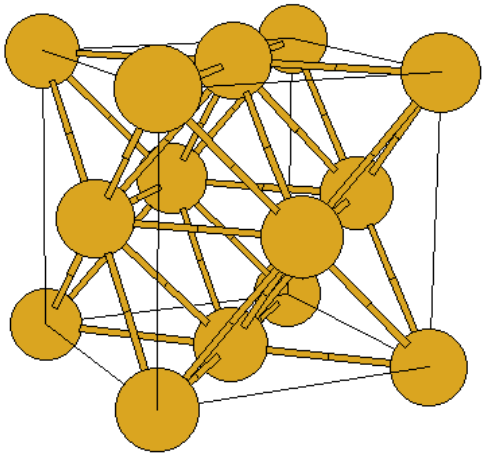

Figure 4.3 Face centered cubic unit cell (Au and Ag). *Use of image complies with BSDU license.*

Gallium is a unique metal which can exist in various phases at the temperatures studied in this work. However, only α phase gallium is relevant here. α-Ga has a orthorhombic lattice unit cell. Unlike the cubic cells, it has edges of different lengths thus it lacks the symmetry of the cubic lattices and has more than one point in the primitive cell (four lattice points). This leads to the presence of optical vibration modes in its wave vectors. Thus unlike most metals it can have a Raman signal [1].

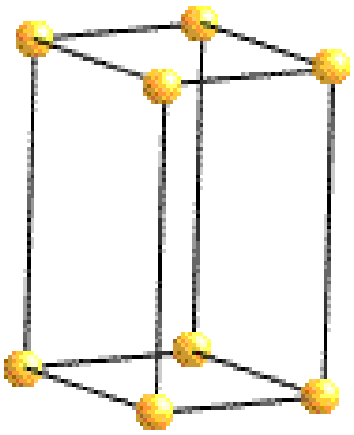

Figure 4.4 Orthorhomic lattice unit cell (alpha phase gallium). *Use of image complies with BSDU license.*

Because of the obvious differences among these lattices all of the presented materials have different vibrational modes.

The energy of these modes are detected using a technique called Raman spectroscopy which shows peaks at the inverse wavelength corresponding the energy of the vibration. This is observed optically as phonon replicas, or a replication of a PL peak a distance equivalent to the phonon energy away from the original.

Alloyed semiconductors such as AlGaAs and InGaN exhibit phonons from their individual partial lattices i.e. AlAs, GaAs, InN, and GaN. This behavior arises from the fact that, to some extent, both these lattices coexist in the material. This fact is illustrated by image 4.2 where aluminum or gallium take be part of the lattice overlapping with the arsenide. This is why phonons in these materials are labled as originating from either one of its building blocks. For example AlGaAs has both “GaAs-like” and “AlAs-like” phonons.

4.1 Case Study in Aluminum Gallium Arsenide

The Raman spectra of bulk GaAs and GaAs-AlGaAs single quantum wells is observed to change due to the presence of gallium droplets for both a GaAs reference wafers and GaAs-AlGaAs SQWs. Figure 4.1.1 shows the Raman spectra for bulk GaAs and a GaAs-AlGaAs SQW with and without gallium droplets. All wavenumber axes are the same scale, and the plots are aligned vertically for easy comparison. The same back scatter geometry was used for every sample. The gallium spectra are on the left, the QW spectra are on the right and the droplet covered samples are on the bottom. All the peaks of the reference samples are highlighted in green, and the highlight goes down to the image charge samples to emphasize that these peaks are also present in the image charge case, although they may be somewhat shifted.

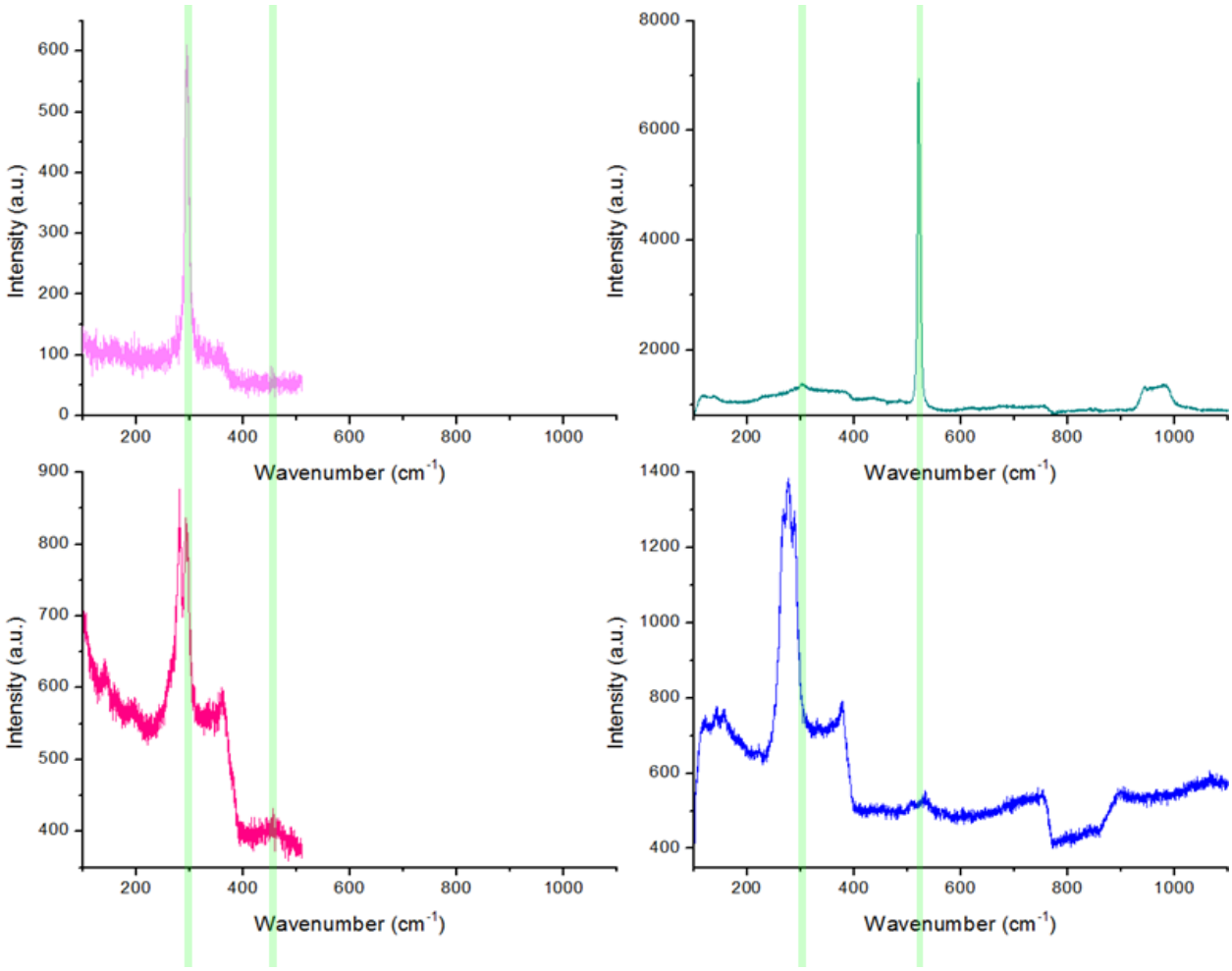

Figure 4.1.1 Raman spectra of GaAs (top left), GaAs with Ga droplets (bottom left), GaAs-AlGaAs SQW (top right), and GaAs-AlGaAs SQW with Ga droplets (bottom right).

The GaAs LO_1 mode at 289 cm^{-1} is present in all samples (288cm^{-1} to 293cm^{-1}) [1, 2]. The presence of this peak in all samples is obvious. The peak at 277 cm-1 is the bi-modal GaAs longitudal optical (LO) phonon [3]. The intensity of the LO_1 peak seems smaller in the QW sample but only relative to the other peak. This peak is slightly shifted in the droplet case which indicated that the electrostatic field decreases the phonon energy as expected [4].

Both quantum well Raman spectra exhibit the $2LO_1$ peak at 522cm^{-1}[5, 6], which are not present in the GaAs samples. This is un-remarkable as phonons commonly manifest at hetero-junctions of semiconductors.

In the image charge quantum well, the TO_1 mode at 268^{-1} [1] appears, either showing a change in selection rules or an increase in oscillator strength. The first explanation is far more likely since the well is grown on the 100 plane. Phonons with small oscillator strength are not observable in a Raman spectrum [5], however transvers optical (TO) modes are not expected in samples such as these which are grown along the (100) plane. What is especially interesting about this is that there is on such Raman peak in the reference well, and thus the presence of this peak is attributed to the image charge effect.

The peak assignments and which system they are present in are presented in table 4.1.1. A check marked box indicated that the peak is present, while an empty box indicated that the peak is absent from the Raman spectrum of that sample.

Table 4.1.1 Raman peak assignments and list of peaks present.

Peak Position	Peak Assignment	GaAs	GaAs droplet	GaAs-AlGaAs	GaAs-AlGaAs droplet
268 cm^{-1}	GaAs like TO_1				✓
277 cm^{-1}	GaAs like bi-modal LO	✓	✓	✓	✓
289 cm^{-1}	GaAs like LO_1	✓	✓	✓	✓
522 cm^{-1}	GaAs like $2LO_1$			✓	✓

It should be noted that the noisy peaks in the gallium covered samples between 100 cm^{-1} and 200 cm-1 are from folded zone LA phonons, however these peaks are always to noisy to merit individual, or any, assignment.

A phonon is an oscillation displacement of a lattice point, let us call it Q

$$\boldsymbol{Q}(\boldsymbol{r},t) = Q(\boldsymbol{q},\omega_0)\cos(\boldsymbol{q}\cdot\boldsymbol{r} - \omega_0 t) \tag{4.1.1}$$

where **q** is displacement vector, **r** is the position, t is the time, and ω_0 is the frequency. In the

isotropic approximation the electric susceptibility, χ, is taken to be a scalar instead of a second rank tensor. Furthermore in the adiabatic limit χ can be defined as a Taylor series of **Q**.

$$\chi(\boldsymbol{k_i}, \omega_i, \boldsymbol{Q}) = \chi_0(\boldsymbol{k_i}, \omega_i) + \frac{\partial \chi}{\partial \boldsymbol{Q}_0}\ [\boldsymbol{Q}(\boldsymbol{r}, t)] \tag{4.1.2}$$

There exist two sources of polarization in the solid structure, one which vibrates in phase with the incident radiation (Raman excitation), and one which is induced by the phonons in these materials. These are labeled as P_{ex} and P_{ind} respectively.

$$\boldsymbol{P_0}(\boldsymbol{r}, t) = \chi_0(\boldsymbol{k_i}, \omega_i)\boldsymbol{F_i}(\boldsymbol{k_i}, \omega_i)\cos(\boldsymbol{k_i} \cdot \boldsymbol{r} - \omega_i t) \tag{4.1.3}$$

where F_i is the i^{th} component a plane electromagnetic wave.

$$\boldsymbol{P_{ind}}(\boldsymbol{r}, t, \boldsymbol{Q}) = \frac{\partial \chi}{\partial \boldsymbol{Q}_0}\ [\boldsymbol{Q}(\boldsymbol{r}, t)]\boldsymbol{F_i}(\boldsymbol{k_i}, \omega_i)\cos(\boldsymbol{k_i} \cdot \boldsymbol{r} - \omega_i t). \tag{4.1.4}$$

Thus the total polarization is

$$\boldsymbol{P}(\boldsymbol{r}, t, \boldsymbol{Q}) = \boldsymbol{P_0}(\boldsymbol{r}, t) + \boldsymbol{P_{ind}}(\boldsymbol{r}, t, \boldsymbol{Q}). \tag{4.1.5}$$

The Raman tensor **R** is defined as

$$\mathrm{R} = \frac{\partial \chi}{\partial \boldsymbol{Q}_0}\left[\frac{\boldsymbol{Q}(\boldsymbol{r}, t)}{|\boldsymbol{Q}(\boldsymbol{r}, t)|}\right] = \frac{\partial \chi}{\partial \boldsymbol{Q}_0}\ [\widehat{\boldsymbol{Q}}(\boldsymbol{r}, t)]. \tag{4.1.6}$$

Fallowing the derivation in Yu and Cardona [8] the Raman tensors of GaAs become

$$\mathrm{R}(\hat{\boldsymbol{x}}) = \begin{bmatrix} 0 & 0 & 0 \\ 0 & 0 & d \\ 0 & d & 0 \end{bmatrix} \tag{4.1.7}$$

$$\mathrm{R}(\hat{\boldsymbol{y}}) = \begin{bmatrix} 0 & 0 & d \\ 0 & 0 & 0 \\ d & 0 & 0 \end{bmatrix} \tag{4.1.8}$$

$$\mathrm{R}(\hat{\boldsymbol{z}}) = \begin{bmatrix} 0 & d & 0 \\ d & 0 & 0 \\ 0 & 0 & 0 \end{bmatrix} \tag{4.1.9}$$

where the coefficients of the tensor are given by

$$\mathrm{d} = \text{Ŕ}(\mathrm{i},\mathrm{j}) = \frac{-m^{*}\omega_{kj}\omega_{ki}\langle\psi_k|x|\psi_j\rangle\langle\psi_k|x|\psi_i\rangle}{-\delta + i\Gamma} \tag{4.1.10}$$

where I, j, k are cyclic coordinate indecies, m* is the effective mass, δ is a parameter related to the detuning of the laser, Γ is the line width of intrasubband transitions, and ψ is the envelope function [13].

The above tensors ignore the miniscule change in frequencies between the incoming and outgoing photons [8]. In the back scatter Raman geometry the TO phonons must be perpendicular to the incident beam, **q**. this is not the case for LO phonons. If the incident and scattered wave vector is parallel to the wave vector the TO modes will not be present. The intensities of the LO and TO mode intensities are given in equations 4.1.10 and 4.1.11.

$$I_{TO} = \left|\sum_{x,y,z} \hat{x}_i R^z_{xy}(\alpha\, \varphi^z)\hat{y}_s\right|^2 \tag{4.1.11}$$

$$I_{TO} = \left|\sum_{x,y,z} \hat{x}_i R^z_{xy}(\alpha\, \varphi^z + \beta k^z)\hat{y}_s\right|^2 \tag{4.1.12}$$

where ϕ^z are phonon polarization vectors R are the Raman tensor and α is a short range force constant. The coefficient β is the measure of electric field related to the LO phonons in the crystal [10].

The coefficient β is present in the “extra” term of the TO intensity phonon and is not present in the LO phonon intensity. It should be noted that samples grown on the (110) plane are expected to have only TO phonons active and samples grown on the (100) plane should have only LO samples active. Thus it is surprising that the GaAs active quantum well layer grown on the (100) plane should display optically active TO phonons. This is mostly likely due to the

presence of nonuniform electric fields due to the image charge interactions. Furthermore deposition the gallium layer can in no way introduce strain or damage to the GaAs layer. In the present system, however, the ICF contributes to β. This is because the inhomogeneous external field in this system alters the Fi sates of equations 4.1.3 and 4.1.4 leading to an effective wave vector in the (110) direction without physically damaging the lattice.

In an analogy to the Stark effect, binding energy and electron phonon coupling are decreased [4]. The case in the presented system is somewhat more complicated due to the presence of parallel and perpendicular components of the none internal electric field in the lattice. These components lead to a perceived change in the electric susceptibility, χ which propagates all the way to the Raman tensor, thus altering the selection rules. Although surface roughness and damage from ion beams have the same effect on the Raman spectrum they are different in that they physically alter the Raman active layer. By indroducing disorder through damage the other crystal orientations are truly present. In the image charge case however, the physical structure of the Raman active GaAs layer is not altered, but the oscillations of atomic nuclei are perturbed by the introduction of an electric field.

4.2 Chapter References

1. O. Pages, A. Lazreg, A. Zaoui, M. Certier, C. Thiandoume, A. Bouanani, L. Svob, O. Gorochov, D. Bromann, Thin Solid Films 364, 123 (2000)
2. Z.P. Wang, H.X. Han, G. H. Li, D.S. Jiang, K. Ploog, Phys Rev B 38, 12 (1988)
3. K.W. Sun, C.M. Wang, H.Y. Chang, S.Y. Wang, C.P. Lee, J. of Lumin. 92, 145 (2001)
4. Z.P. Wang, X.X. Liang, Phys. Rev. A 373 2596 (2009)
5. D. Varandani, N. Dilawar, A.K. Bandyopadhyay, Thin Solid Films, 444, 221 (2003)

6. G. Scamarcio, A. Cingolani, R. Cingolani, K. Lloog, Surface Science 228, 213 (1990)

7. J.A. Creighton, and R. Withnall, Chemical Physics Letters 326, 311 (2000)

8. Peter Y. Yu and Manuel Cardona, Fundamentals of Semiconductors: Physics and Materials Properties, Springer Heidelberg Dordrecht London New York 2010

9. Charles Kittle, Introduction to Solid State Physics eight edition, John Wiley & Sons International New Celodonia 2005

10. A.J. Semjonow, A. Kau, K. Lenz, B.D. Nechiporuk, V.V. Strel'chuk, M.J. Walakh, J. of Molecular Struct. 267, 155 (1992)

11. T. Sekine, K. Uchinokura, E. Matsuura, J. Phys. Chem. Solids, 38 1091 (1977)

12. K. Kikuchi, K. Tada, M. Aoki, , J. Phys. Chem. Solids 41, 1361 (1980)

13. M. Miura, S. Katayama, Science and Technology of Advanced Materials 7 286 (2006)

14. T.D. Harris, M. Lamont Schnoes, L. Seibles, Anal. Chem. 61 994 (1989)

15. S.J. Chua, S.J. Xu, X.H. Tang, Solid State Comm. 98 1053 (1996)

16. S.D Lin, H.C. Lee, K.W. Sun, C.P. Lee, J. of Lumin. 94 761 (2001)

17. K. Huang, A. Rhys, Proceedings of the Royal Society of London. Series A, Mathematical and Physical Sciences, 1950

18. R.C. Miller, D.A. Kleinman, A.C Gossard, Solid State Comm. 60 213 (1986)

19. H.W. Kunert, Appl. Surface Sci. 166 304 (200)

CHAPTER 5

DETAILS ON USED METAL-SEMICONDUCTOR META-MATERIALS

The samples used in this work include GaAs-AlGaAs and GaN-InGaN quantum wells. These samples are divided into sets; each set tries to isolate a single parameter which is to be studied related to the image charge effect.

5.1 GaAs-AlGaAs SQWs Varying Well Width Using Gallium Droplets to Induce an Image Charge Potential

The GaAs/AlGaAs samples were grown by the group of Dr. Salamo from the University of Oklahoma. These samples are designed to study the effects of the well width dependence on the image charge effect in aluminum gallium arsenide quantum wells. These samples were fabricated molecular beam epitaxy (MBE) on the (100) plane. Three sample were fabricated on identical GaAs substrate, on the substrate a 20 nm AlGaAs barrier was deposited then the GaAs quantum well, then a 10 nm AlGaAs barrier then a 5 nm GaAs cap layer. The samples differed only with the width of the GaAs wells which were made 10 nm, 5 nm, and 2 nm wide. On these samples (on the 5 nm cap layer) gallium (Ga) droplets were deposited by growing a few

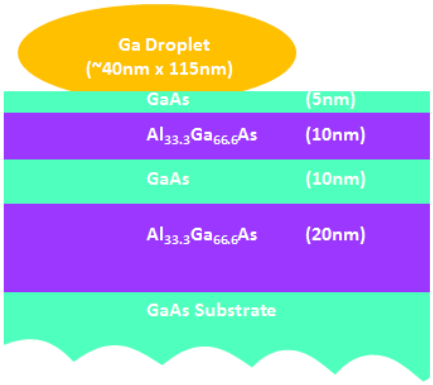

Figure 5.1.1 AlGaAs-GaAs 10 nm SQW with gallium droplet

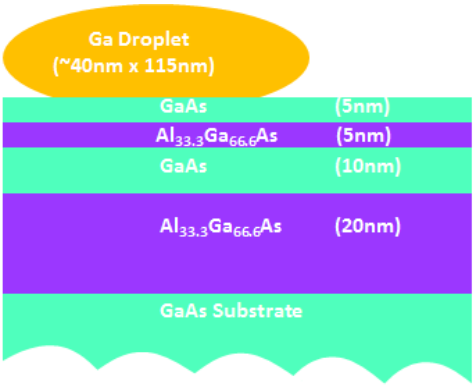

Figure 5.1.2 AlGaAs-GaAs 5 nm SQW with gallium droplet

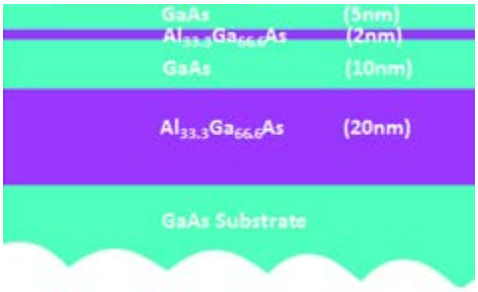

Figure 5.1.3 AlGaAs-GaAs 2 nm SQW without gallium droplet

monolayer gallium film which later aggregated into droplets. Parts of these wafers had the gallium droplets removed by etching them of with HCl. The samples with etched off gallium are refered to as reference samples since they are the quantum well without the image charge field. Occasionally these wells are called bare since there is nothing on these quantum wells.

The density of gallium on all these wells was the same on all samples from this set; it is about 13 droplets per square micron. The droplet height is about 80 nm and their diameter looking from the top varies between 40 nm and 115 nm. These droplets are self-assembled from a fluid and have curved edges; they are in no way rectangular. Fig. 5.1.4 shows an AFM micrograph of the sample surface showing the random distribution of the gallium droplets.

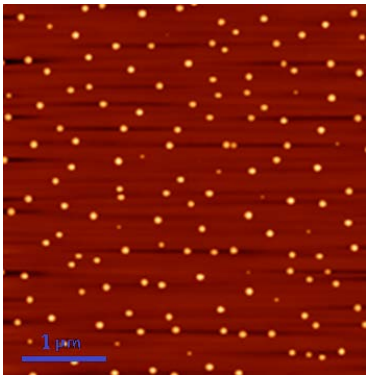

Figure 5.1.4 AFM showing gallium droplet distribution on AlGaAs-GaAs SQW from sample set 1

These samples were excited optically threw the top, or the sparse gallium droplets.

5.2 GaAs-AlGaAs SQWs Varying Cap Layer Height Using Gallium Droplets to Induce an Image Charge Potential

These samples were fabricated to study the effects of the intensity of the image charge force field on optical properties of the GaAs-AlGaAs SQWs by the same group, using the same Al incorporation as the samples in sections 5.1. Because of its reactivity with ambient atmosphere aluminum gallium arsenide cannot be used as the cap of the sample. This is why all GaAs-AlGaAs wells have a thin protective gallium coating on top of the AlGaAs barrier (In the case of GaN-InGaN the cap material is the QW barrier material). By varying this cap layer the properties of the top well barrier, such as height or strain, are not altered, making these

structures ideal for studying image charge intensity. Figure 5.2.1 depicts these samples to scale schematically.

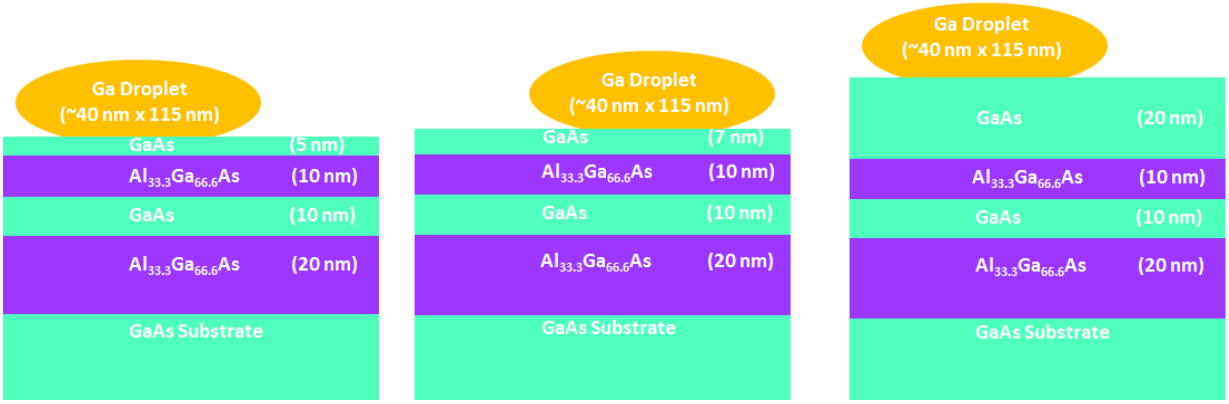

Figure 5.2.1 GaAs-AlGaAs SQWs carying cap layer height using gallium droplets to induce and image charge interaction.

The gallium droplet distribution of these samples is also the same as that of samples in section 5.1, thus the AFM in figure 5.1.4 is applicable to this sample set and will not be repeated here since it would offer no new insight.

5.3 GaAs-AlGaAs SQWs with Gallium Droplets Mixed with Plasmonically Resonant Metal Nanoparticles

The GaAs-AlGaAs meta materials in the previous samples isolated the image charge effect. This sample set is designed to study the effects of metals which are plasmonically resonant and off resonant simultaneously. Plasmonic interaction of GaAs-AlGaAs SQWs are well studied and documented and cited as needed thought the text.

In order to induce plasmonic interactions colloidal metal solutions were evaporated on top of the gallium covered caps of the quantum wells of sections 5.1 and 5.2. This allows for the study of the interplay of plasmonics and the image charge effect with minimal alteration to the sample. Since the colloidal solutions were evaporated on the surface, the internal structure of

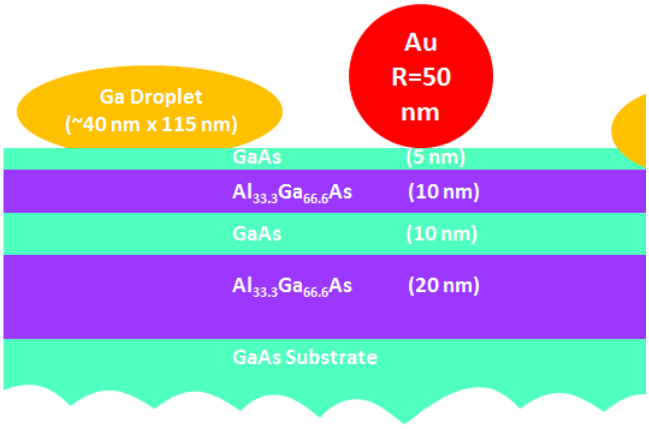

Figure 5.3.1 GaAs-AlGaAs 10 nm SQW with gallium droplets and gold particles.

the samples used in the image charge studies are in no way altered, and it is possible to remove the evaporated metal layer. A gold colloidal solution was deposited on a 10 nm well with a 5 nm cap (Fig. 5.3.1), this is the same quantum well as in sections 5.1 and 5.2 only with the addition of gold. Using the same sample in multiple study sets is a strength of this work since the comparisons of different parameters can be studied simultaneously. Figure 5.3.2 shows a 1.5 nm QW with a 5 nm cap layer with deposited silver colloids. These colloids were smaller and tended to conglomerate together. The AFM image of this is presented in figure 5.3.3. The AFM also shows noise form the suspension of these particles. This sample set was made with the smallest cap layer used in this work purposely because the effective plasmon interaction strength decreases exponentially.

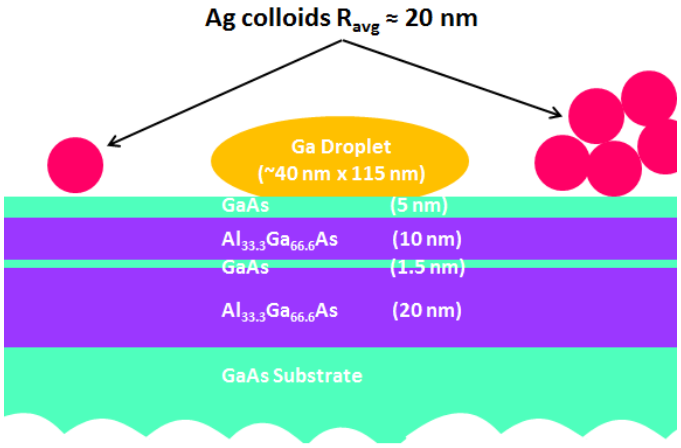

Figure 5.3.2 GaAs-AlGaAs 1.5 nm SQW with gallium droplets and silver nanoparticles.

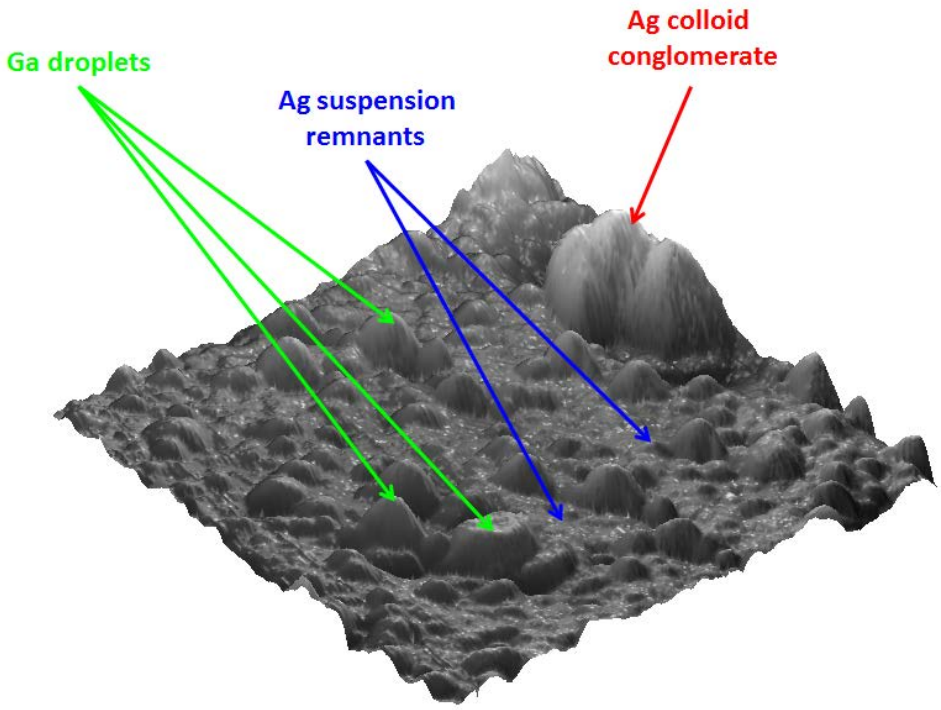

Figure 5.3.3 AFM image of the surface of the 1.5 nm QW with a 5 nm cap, silver and gallium are the distinct features.

5.4 GaN-InGaN SQWs Varying Well Width Using Gold Thin Films to Induce an Image Charge Potential

Samples for studying the quantum well width dependence in indium gallium nitrate were fabricated by the group of Dr. Watson at SUPA, Institute of Photonics, University of Strathclyde, Glasgow, UK. Actually, they were not, these samples were made for Padma Rekha Vemuri to study the excitation angle dependence on photoluminescence and work involving this is part of her thesis. The samples however do show image charge effect behavior and only their contribution to this work will be described here (which is original and not done before). These samples were grown using metal organic vapor deposition. The samples had a gold thin film deposited on top which provides the metal interface which sustains image charges.

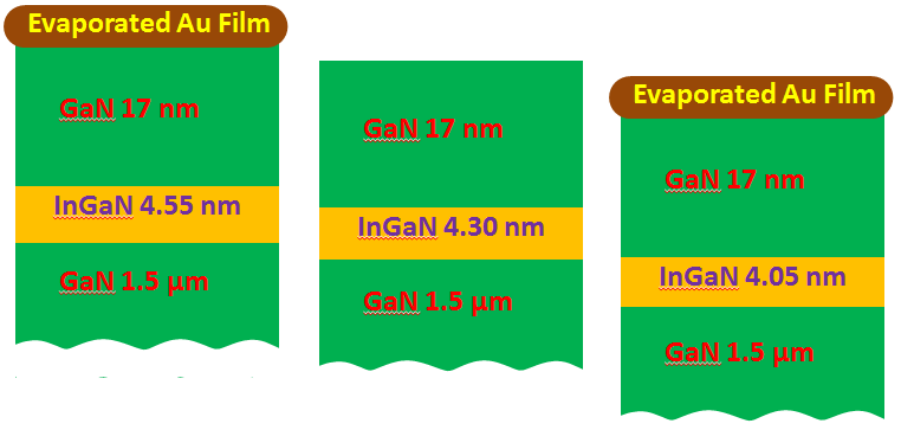

Figure 5.4.1 samples from this sample set, the 4.55 nm and 4.05 nm wells are shown with a gold film (samples) and the 4.30 nm well is s hown without a gold layer.

The well widths were 4.05 nm, 4.30 nm, and 4.55 nm (Fig. 5.4.1). Again the wells which have the metal for image charges are referred to as the sample and the none gold covered films are the reference or bare samples. The gold films were deposited by evaporation gold metal ingots using a VEECO Evapatrol (VE-400) metal evaporator.

Figure 5.4.2 AFM micrographs of the gold covered SQW and the bare SQW

The atomic force microscopy micrographs for the samples and reference are presented in figure 5.4.2. The sample with the gold layer shows less roughness. The roughness of the gold film is roughness of the film is estimated as 3 nm and 2.5 nm for the sample without a metal layer.

The sample was backed polished using an Allied Tech Prep P/N 15-2000 mechanical polisher. The sample was polished on top before deposition of the gold film. The bottom of the sample was also polished to allow for back excitation. Back excitation for this sample set is necessary since metal films will not transmit light, and it was necessary to back excites the samples.

5.5 GaN-InGaN SQWs Using Gallium Droplets to Induce an Image Charge Potential and the Droplets are Close Enough for Resonant Plasmon Modes on the Droplets to Induce Plasmonic Coupling with the Well

These samples were made for the purpose of studying the co-existence of the image charge effect and plasmonics. These samples were grown using metal organic chemical vapor deposition by the group of Henry O. Everitt at the Department of Physics at Duke University. There were two different well widths: 3 nm and 4.05 nm. The samples were grown on commercial sapphire substrate. Gallium droplets were fabricated by depositing a few monolayers of gallium in the fabrication chamber and the droplets then self-assembled. Half of the wafer was masked during gallium growth, thus only half of the wafer ever had gallium droplets deposited on it. Thus the part without the gallium is referred to as the reference sample, and the half with the gallium droplets for image charge is the sample. These droplets were grown very close together, thus their plasmon resonances couple creating higher plasmon energies. An AFM micrograph of a typical top of a gallium a sample is presented in figure 5.5.3 while the AFM for a bare sample is presented in figure 5.5.4. These samples may be optically excited through the thick gallium droplets. However the samples were also back polished to

allow for back excitation and avoid the scattering and light obstruction from the thick gallium droplets.

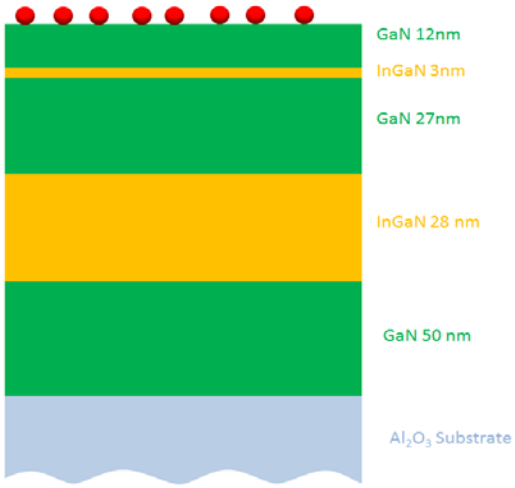

Figure 5.5.1 3 nm InGaN SQW with gallium droplets

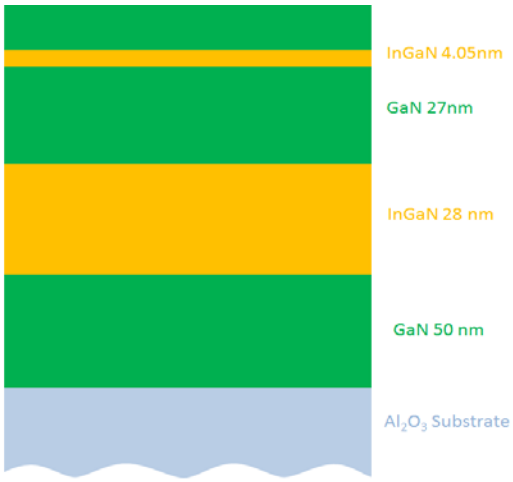

Figure 5.5.2 4.05 InGaN SQW without gallium deposition used as a reference sample

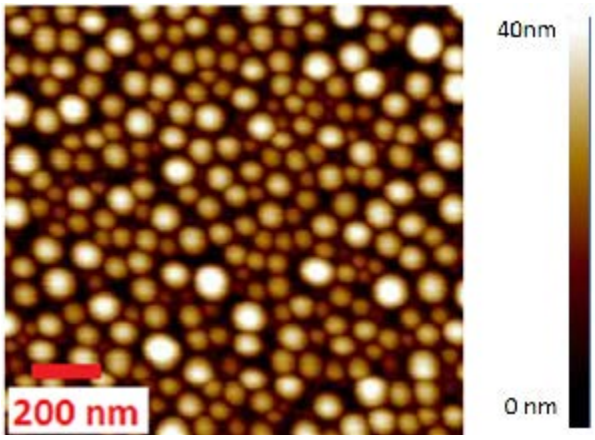

Figure 5.5.3 A typical AFM image of gallium droplets on InGaN SQW sample from this sample set

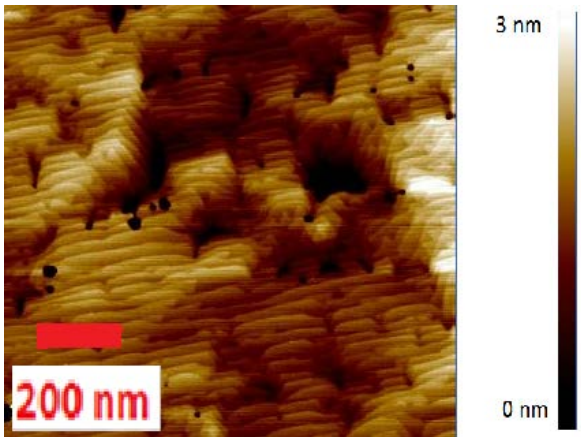

Figure 5.5.4 A typical AFM image of InGaN SQW sample from this sample set without gallium droplets

CHAPTER 6

CONCLUSION

In conclusion the introduction of the electrostatic image charge force between carriers in a semiconductor quantum well and a metal surface is necessary to explain the behavior of the presented systems. The significant shift in energy is the most obvious and unique feature of this effect. Other experimental observations leading to the introduction of the image charge effect include an increase in carrier lifetime, increase in PL intensity, and none linear power v. PL intensity dependence.

To the best of my knowledge this effect was first published in 2011 by us in Applied Physics Letters. The image charge has been considered before, especially between semiconductors with different dielectric constants, however this is the first detailed investigation of the image charge effect on carriers in quantum wells due to metals. Furthermore this work introduces the ideas of altering confinement potentials for the first time. Recent progress in plasmonics and nano-photonics brings new interest in possible image charge phenomena, and I expect the effect to be more widely considered in the near future.

The image charge effect is a fundamental physical phenomenon much like plasmonics. Although plasmonics enjoys much popularity the image charge effect still remains obscure. Both effects can coexist, plamsonics is typically dominate, although it cannot explain luminescence emission energy shifts and significant peak broadening while the image charge effect can. It is not necessary to choose either or, chapter 3 exclusively deals with the coexistence of these two effects. The existence of image charge interactions in no way diminishes the usefulness of or excitement about plamsonics.

The study of image charges, like the study of plasmonics, is long and involved. There are multiple approaches and the expectation that a single thesis or book covers all aspects of plasmonics or image charges indicates a lack of understanding of the depth of the subjects. This thesis has two underlying themes which reoccur and relate throughout the work, that the image charge field alters the confinement potential similarly to the Stark effect and that it creates inhomogeneous carrier regions following a statistical Itō model.

The energy shift in quantum wells feeling an ICF may be modeled as any quantum well feeling an electric field. The mathematics of modeling the image charge effect energy shift are taken directly from the mathematics of the Stark effect. This leads to good agreement with theory and experiment. The major difference is that the effective potential of the electron and hole potential differ in the image charge case. This can lead to a blue shift or a red shift, while the Stark effect only causes a red shift.

The presented Itō distribution is used to predict the inhomogeneous carrier distribution in systems which have inhomogeneous metal distributions. The drift term is dependent of the carrier mobility, ICF intensity, and the lifetime. Each of these parameters were isolated experimentally and confirm the theory. The energy shift is dependent on the intensity of the perpendicular component of the electric field, thus close proximity to a metal increase the energy shift.

Carrier mobility may be altered in semiconductors by altering the temperature. Thus experiments on the same sample changing the temperature are used to demonstrate the mobility dependence of the Itō drift term. This describes the temperature dependence of the energy shift, the majority of carriers drift to a certain proximity of the metal islands.

Theory predicts that the ICF varies as the square of the distance between the quantum well and the metal surface. To test this, the image charge field intensity is varied by changing the distance between a quantum well and a metal surface. To do this different sample were created with different GaAs cap layers on top of the well barriers. Since the image charge intensity drops off as a square of the distance changing the cap layer, and not the properties of the confined excitons, allows the isolation of the ICF intensities.

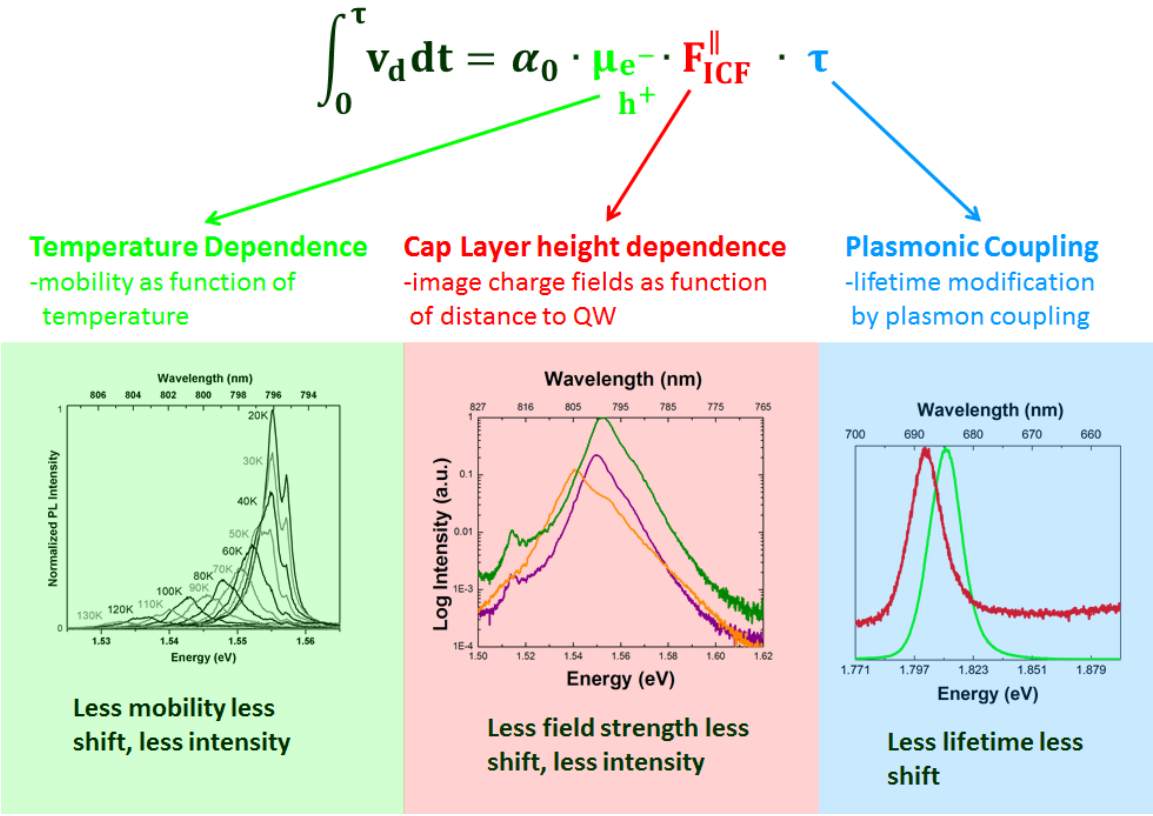

Figure 6.1 The drift term written out and example experiments for isolating each variable in it.

Finally the drift time, or carrier lifetime may be changed in semiconductor systems using plasmonics. By adding plasmonically resonant metal surfaces to image charge samples the carrier lifetime is reduced. This was accomplished by drying aqueous solutions of metal particles which can couple via plasmons with the ICF systems. Thus the necessity of introducing the ICF is demonstrated and mathematics to predict it are introduced.

APPENDIX A

MATHEMATICA MODELING DESCRIPTION

In this work it is necessary to solve wave functions in order to find Eigen state energies of various systems. Often to model a change in energy versus a parameter such as internal electric field, image charge field, or well width it is necessary to solve the equation about a dozen times to produce a plot or table. Thus solving by hand is undesirable and iteration over a changing parameter in a computer program is preferable. Thus I have used Mathmetica (Wolfram Research, Champaign, Illinois). This appendix is meant to detail the procedures used in creating the scripts and to allow for easy understanding of the work.

There are multiple ways of solving quantum confined Eigen energy problems, in this scrip the most simply boundary value matching procedure is used. An example of a wave function to solve is the triangular quantum well:

$$\Psi = \begin{cases} a_1\left(\boldsymbol{i}\,\mathrm{Ai}\left(-\left(\frac{2m^*}{(\hbar eF)^2}\right)^{1/3}(E-V_0-eFx)\right)+\mathrm{Bi}\left(-\left(\frac{2m^*}{(\hbar eF)^2}\right)^{1/3}(E-V_0-eFx)\right)\right) & x<-\frac{L}{2} \\ a_0\,\mathrm{Ai}\left(-\left(\frac{2m^*}{(\hbar eF)^2}\right)^{1/3}(E-eFx)\right)+b_0\mathrm{Bi}\left(-\left(\frac{2m^*}{(\hbar eF)^2}\right)^{1/3}(E-eFx)\right) & -\frac{L}{2}\le x\le\frac{L}{2} \\ a_1\ \mathrm{Ai}\left(-\left(\frac{2m^*}{(\hbar eF)^2}\right)^{1/3}(E-V_0-eFx)\right) & x>\frac{L}{2} \end{cases} \tag{A.1}$$

Where in mathematica the above piece wise defined function is defined as three functions.

```
y1[x_] := b0 (AiryBi[-(2 m/(F^2 hbsq))^(1/3) (En - V - F x)] + I AiryAi[-(2 m/(F^2 hbsq))^(1/3) (En - V - F x)])
y2[x_] := a1 AiryAi[-(2 m/(F^2 hbsq))^(1/3) (En - F x)] + b1 AiryBi[-(2 m/(F^2 hbsq))^(1/3) (En - F x)]
y3[x_] := a2 AiryAi[-(2 m/(F^2 hbsq))^(1/3) (En - V - F x)]
```

(A.2)

where Ai (AiryAi) and Bi (AiryBi) are the Airy functions; E (En) is the energy Eigen State; and a_1, a_0, b_0, and a_2 are normalization coefficients of the wave function, and L is the well width.

Equations A.1 and A.2 are really the same, with equation A.1 being clear about being a single piecewise defined function. Also it is important to note that some constants from eq. A.1 are grouped into one in equation A.2. This is done for ease and will be detailed later in this section. For matching the derivative of the wave function a new set of three functions is defined as the derivative of y_1, y_2, and y_3.

```
y1p[ξ_] := D[y1[x], x] /. x → ξ
y2p[ξ_] := D[y2[x], x] /. x → ξ
y3p[ξ_] := D[y3[x], x] /. x → ξ
```
(A.3)

Such definitions abstract away most of the math involved, but are useful in producing many solutions. Letting y->ψ and assuming that ψ_1 is defined in the region x < -L/2, ψ_2 is defined in the region –L/2 ≤ x ≤ L/2, and ψ_3 is defined in the region x > L/2 boundary condition may be matched. Thus

$$\Psi = \begin{cases} \psi_1 & x < -\frac{L}{2} \\ \psi_2 & -\frac{L}{2} \leq x \leq \frac{L}{2} \\ \psi_3 & x > \frac{L}{2} \end{cases} \tag{A.4}$$

Solving $\psi_1 = \psi_2$ and ψ_1 `= $\psi_2$` at the boundary x = -L/2 yields all normalization constants as function of one of the normalization constants. Doing the same on the boundary x = L/2 i.e. $\psi_2 = \psi_3$ and ψ_2 `= $\psi_3$` yields all normalization constants in terms of only one constant. Applying the normalization condition:

$$\int_{-\infty}^{\infty} \langle \Psi | \Psi \rangle = 1 \tag{A.5}$$

allows for finding the wave function given energy. In order to find the Eigen energy of the wave function a dispersion relation must be found. This is done by finding the roots when the

normalization constants are formed into a single equation with the energy as the independent variable. Thus the wave function and Eigen energies are found.

In Mathematica code the quantity $\frac{2m^*}{(\hbar eF)^2}$ will often appear as $\frac{2m}{F^2\text{hbsq}}$. Where hbsq is shorthand for h-bar square, $\hbar^2$. $\hbar^2$ is in units of eV kg nm^2, thus mass is in kg. The above quantities have units of 1/eV^3. For simplicity of plugging in numbers into Mathematica I use the parameter (eF) as a single variable, F in the script. This may lead to some confusion, but absorbing a constant (e) into a variable is quite common and not detrimental in anyway. The quantity eF has units [C MV/cm] or newtons, however in the script the units are eV/nm. Again this is so that the relevant units are in electron volts and nanometers, which are the necessary units in discussion and experimental planning. Furthermore I only use this with carriers inside a quantum well, the e is always the fundamental charge, q = 1.602*10^{-19} C. Thus when seeing a substitution of F=x in the script one should remember that the electric field really is equal to $x/|q|$ or x/q since q is always taken as positive. Thus for example a value of 2 MVcm^{-1} appears as 0.2 [eV/nm] or (q 2 MVcm^{-1})^2 or 1 MVcm^{-1} becomes 0.1 [eV/nm].

The above discussion is for generating a single data point for a specific set of, PEF, ICF, barrier height, well width, effective mas, and external field. However, for this work it is necessary to calculate the equation multiple times to find the trends in section 2.1. In order to find a trend Mathematica provides iterators which allow for a few lines to generate results for as many related results as desired. The construct used in the work is the Do[] loop. First it is necessary to define a variable which will be iterated over.

```
well_width = 3.2;  (* well width in nm *)
```

The above line defines a variable called well_width with a value of 3.2 and makes a comment that it is well width in units of nanometers. The well_width variable will be changed by the Do loop itself. Thus it is important to understand the syntax of the loop before proceeding.

```
Do[
 {expressions},
 {iterator, iterator_min _value, iterator_max _value, iterator_incrament}
]
```

As the above snippet show Do[] takes two lists as its arguments. The first is expressions, which are such as solve for this Eigen value as discussed above. The second list contains two to four values but the four valued list is discussed here. The first thing in the list is the name of the variable being iterated over, or well_width in the current example. Second is the minimum value that variable will take, then the maximum value that variable will take then the amount that variable will change at each iteration. For example the syntax (well_width, 2, 3, 0.05) will execute twenty times and the well width variable will have 20 different value: 2.00, 2.05, 2.10, 2.15, … , 2.90, 2.95, 3.00. The relevance of this is that the expressions part involving the dispersion relation is a function of well_width and will generate a different (correct and unique) result for each iteration of the loop. This can of course be extended to any variable(s) and expression(s) used in this work. To vary multiple variables it is possible to put a Do loop as one of the expressions for the outer loop, thus generating results for all permutations of the variable s they iterate over, this is called nesting.

The major short coming of this approach is that the mathematics is applied only to a wave function without considering what the Hamiltonian actually is. This presents a problem when the slope of the triangular potential (eF) becomes greater than the well potential.

Mathematical solutions exist, however physically there is a scattering potential, not a confined potential thus results from such inputs are meaningless.

It is necessary to remember that observed data for luminescence emission in an ensemble of many recombinations while this simulation is energy for only a single electron hole pair. It is expected that a single electron hole pair will produce a delta function emission, only at one energy, as this code predicts. However, many electron hole pairs continuously recombine in a real quantum well leading to a Gaussian like distribution in the emission spectrum.

APPENDIX B

SOLENOID CONSTRUCTION FOR MAGNETIC FIELD IN CRYOSTAT

Electric and magnetic fields are fundamentally the same phenomena but only in different reference frames. The image charge effect is an elementary electrostatic phenomenon, however in some sample sets it generates an attractive potential for the two dimensional exciton gas which alters the behavior of exciton dynamics in the quantum well. To study this effect construction of a magnetic attachment for the laboratory cryostat was attempted.

A home built closed circuit helium cryostat is used for low temperature photoluminescence. Figure B.1 shows the cold finger onto which the sample holder mounts (the sample is clipped to the sample holder). It is important to maintain maximal contact area with the cold finger for better heat transfer and temperature stabilization. Any new holder must also fit in the two mounting screws on either side of the cold finger. Furthermore the sample holder may not touch any of the exterior shell of the cryostat or the air outside will be cooled, condensation will form on the cryostat, and low temperature will never be reached. Thus the radius of the solenoid and this length are constrained by the dimensions of the cryostat. Electric wires run through the length of the cryostat to input / output ports on the outside. One of the ports is connected to a power generator which is used to drive DC into the solenoid (there is a separate tuned box for temperature control, which cannot attach at the same time due to lack of ports). Also a

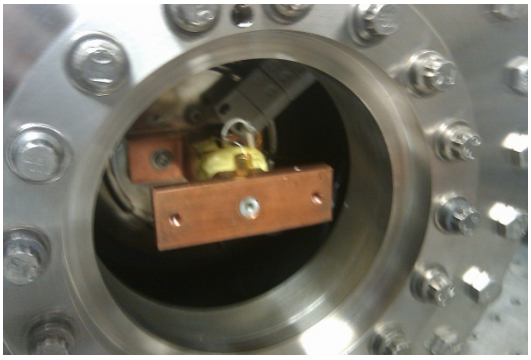

Figure B.1 Cryostat cold finger with sample holder removed.

temperature probe read out is run through the ports to observe the temperature in the cryostat.

Figure B.2 shows the original sample holder and the solenoid used for creating a magnetic field. The sample mounts are clips and the mounting screws are made to match the cold finger mounts.

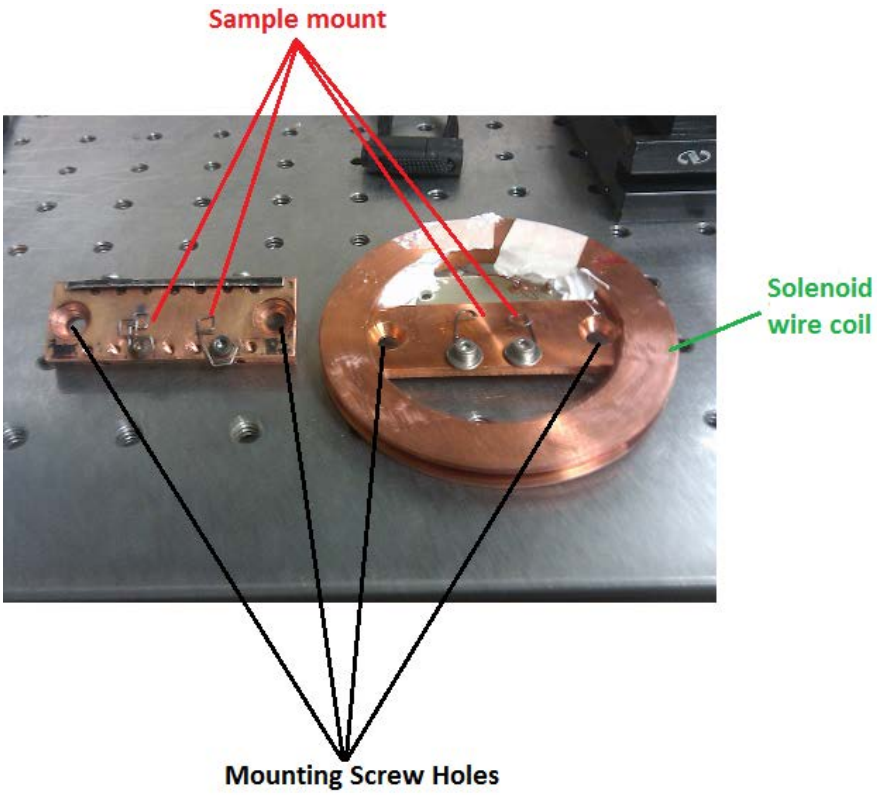

Figure B.2 Heater sample holder (left) and sample holder with solenoid (right).

It was necessary to have the solenoid wire coils run outside the mounting screws due to space constraints to mount the actual samples. The sample mount thickness is half of the colloid thickness to make the sample be in the center of the solenoid. The thichness of the coil and its radius are made to not touch the cryostat wall.

The power supply for the heater/magnet comes from outside through connection ports on the back of the cryostat. A power cable runs inside the cryostat from the external port to the

cold finger, due to lack of wiring it is only possible to power the magnet or heater, not both. This means that in order to switch operating mode from heater to magnet the cold finger itself must be removed.

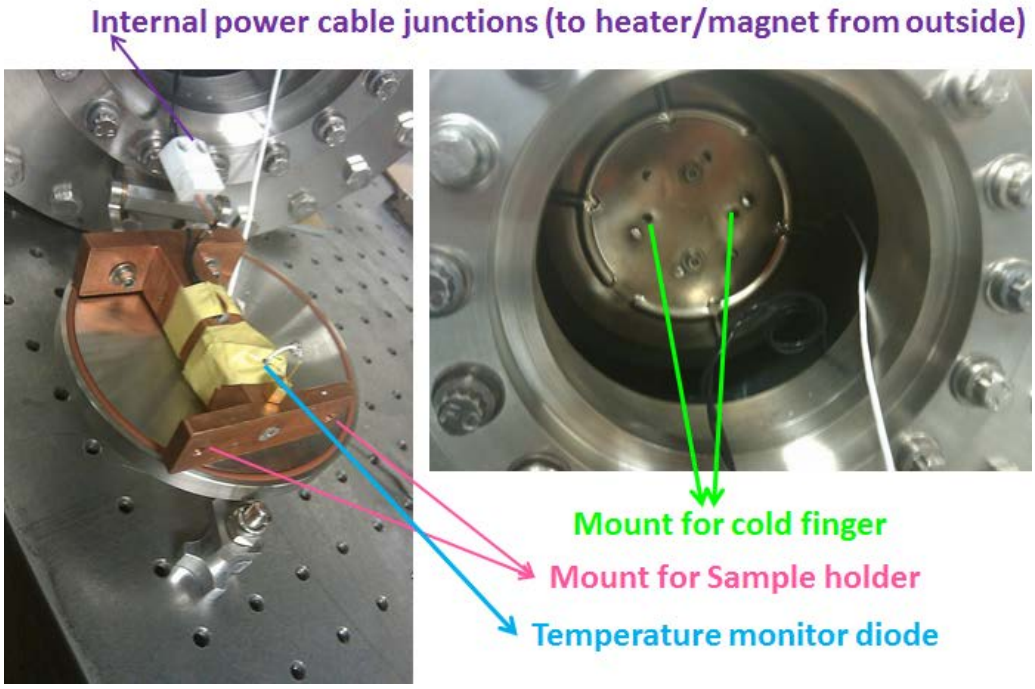

Figure B.3 Copper cold finger (left) and mount for cold finger inside open cryostat

Figure B.3 shows the removed cold finger and the mount for it inside the cryostat. The internal power cable may not be plugged/unplugged while the cold finger is in place due to lack of space. Thus when exchanging the sample holder, some assembly is required. The cold finger itself has a heater and a temperature read out diode attached to it. The temperature read out functions with either with the heater or magnet.

The magnetic field, B, at the center of an ideal solenoid is given by

$$B = \mu_0 N i \times {}^{1}/_{l} \tag{B.1}$$

Where μ_0 is the magnetic constant, N is the number of turns in the solenoid, i is the current, and l is the length of the solenoid. This idealized equation is not applicable to the real solenoid used in the laboratory.

The approximations used in equation 1 which are not applicable are that the solenoid is long compared to its radius, and that the wires are infinitesimally thin, and packed together tightly. The field was measured experiment as 75 Gauss per amp threw the solenoid coils. The power supply provides a maximum of 13 amps thus the field inside the solenoid may reach 975 Gauss or 0.0975 Tesla. This field however is too low to affect excitons in semiconductor systems.

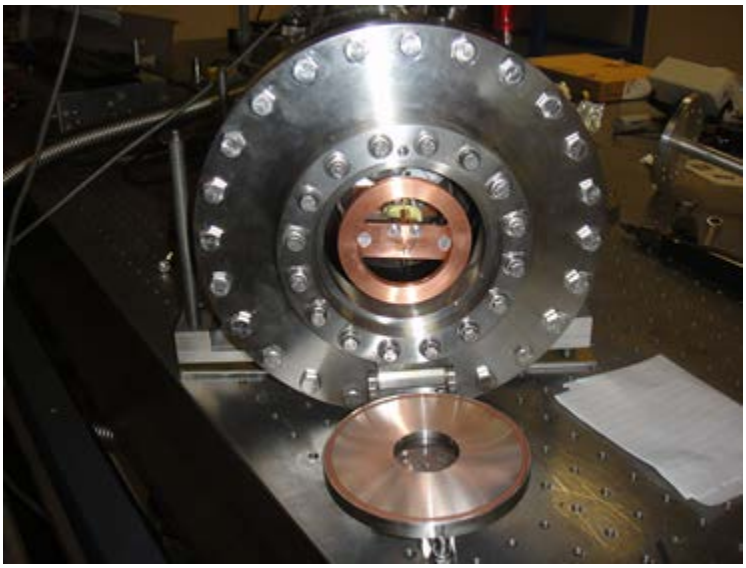

Figure B.4 Cryostat with solenoid sample holder and mounted sample

There are several ways to increase the magnetic field in the solenoid. The most obvious way is to use superconducting wires or wires with less resistance. The resistance is the primary reason for decreasing current and thus the electric field. Also heating is a problem as it competes with the cooling process in the cryostat and causes the resistance to rise thus the field strength falls quickly. In this system, heating is the greatest obstacle for creating a stable magnetic field in the cryostat.

Another possibility for increasing the field strength is to remake the cold finger to be shorter thus allowing to make the solenoid to be deeper (increase height of cylinder) and have more turns of the wire. This will make the approximation for the ideal solenoid more applicable and the field will increase dues to more current and thus more field intensity.

Yet another way to increase the magnetic field is to rewire the single wire in the solenoid in parallel. Using multiple wires in parallel will decrease resistance as compared to a single wire thus reducing heating.

APPENDIX C

COPYRIGHT NOTICES

All reproduced images fall into one of the fallowing license agreements.

C.1 The BSDU License for images from internet.

“

Redistribution and use in source and binary forms, with or without modification, are permitted provided that the following conditions are met:

1. Redistributions of source code must retain the above copyright notice, this list of conditions and the following disclaimer.
2. Redistributions in binary form must reproduce the above copyright notice, this list of conditions and the following disclaimer in the documentation and/or other materials provided with the distribution.
3. Neither the name of Baszoetekouw nor the names of its contributors may be used to endorse or promote products derived from this software without specific prior written permission.

THIS SOFTWARE IS PROVIDED BY BASZOETEKOUW "AS IS" AND ANY EXPRESS OR IMPLIED WARRANTIES, INCLUDING, BUT NOT LIMITED TO, THE IMPLIED WARRANTIES OF MERCHANTABILITY AND FITNESS FOR A PARTICULAR PURPOSE ARE DISCLAIMED. IN NO EVENT SHALL BASZOETEKOUW BE LIABLE FOR ANY DIRECT, INDIRECT, INCIDENTAL, SPECIAL, EXEMPLARY, OR CONSEQUENTIAL DAMAGES (INCLUDING, BUT NOT LIMITED TO, PROCUREMENT OF SUBSTITUTE GOODS OR SERVICES; LOSS OF USE, DATA, OR PROFITS; OR BUSINESS INTERRUPTION) HOWEVER CAUSED AND ON ANY THEORY OF LIABILITY, WHETHER IN CONTRACT, STRICT LIABILITY, OR TORT (INCLUDING NEGLIGENCE OR OTHERWISE) ARISING IN ANY WAY OUT OF THE USE OF THIS SOFTWARE, EVEN IF ADVISED OF THE POSSIBILITY OF SUCH DAMAGE.
“

Please not that an image is a binary file.

C.2 American Institute of Physics author license

“

An author may use his/her own article, or portions thereof, in his/her thesis or dissertation provided that the appropriate copyright credit line is included.

“

-

https://urresearch.rochester.edu/fileDownloadForInstitutionalItem.action?itemId=2709&itemFileId=3730

C.3 Creative Commons

Please see http://creativecommons.org/licenses/

C.4 GFDL-OpenGeoDB